Polymerization and Replication of DNA/RNA in a Thermal Trap

Christof Mast

Dissertation

München, Juni 2013

Polymerization and Replication of DNA/RNA in a Thermal Trap

Christof Mast

Dissertation
zur Erlangung des Grades
Doktor der Naturwissenschaft (Dr. rer. nat.)

an der Fakultät für Physik
der Ludwig-Maximilians-Universität
München

vorgelegt von
Christof Mast
aus Freising

München, den 03. Juni 2013

Erstgutacher: Prof. Dr. Dieter Braun
Zweitgutachter: Prof. Dr. Ulrich Gerland
Eingereicht am: 3. Juni 2013
Mündliche Prüfung am 1. Oktober 2013

Zusammenfassung

RNA, DNA und Proteine sind die Grundlage allen Lebens auf Erden. Es ist allerdings alles andere als klar, wie die ersten längeren RNA-Polymere mit enzymatischer Aktivität in einer prebiotischer Umgebung entstehen konnten. Selbst in hohen, millimolaren Konzentrationen konnten RNA-Nukleotide höchstens Polymere mit einer Länge von etwa 20 Basen bilden. Diese Arbeit zeigt, wie ein reversibler Polymerisationsprozess mithilfe eines Temperaturgradienten verstärkt werden kann. In länglichen, mit Wasser gefüllten Kammern sorgen solche Temperaturunterschiede für einen konvektiven Kreisfluss, der zusammen mit der thermophoretischen Bewegung der gelösten Biomolekülen entlang des Temperaturgefälles eine thermale Falle darstellt. Derartige Fallen, die auch in hydrothermalen Poren auftreten können, akkumulieren durch ihr physikalisches Nicht-Gleichgewicht längere Polymere exponentiell besser als kürzere. Darüberhinaus ist in reversiblen Polymerisationsreaktionen die Polymerlänge proportional zur lokalen Monomerkonzentration, sodass sich die thermale Falle und die Polymerisationsreaktion gegenseitig verstärken. Dieser Prozess wird mit einer Theorie erklärt, welche in dieser Arbeit experimentell bestätigt werden konnte. Die Ergebnisse zeigen, dass bereits Poren mit einer Länge von 5 cm und einem Temperaturunterschied von 10 K ausreichen, um RNA-Polymere zu bilden, die länger als die kleinsten RNA Replikatoren sind.

Die Vervielfältigung genetischer Information ist ein zentraler Aspekt der Darwinschen Evolution. Diese Arbeit zeigt, wie eine thermale Falle eine exponentielle Vervielfältigungsreaktion antreiben kann, indem ein konvektiver Kreisfluss periodisch aufgeheizt und abgekühlt wird. Zeitgleich wird das Replikationsprodukt durch die Fallenwirkung vor Diffusion in die hochverdünnte Umgebung geschützt. In einer Beispielreaktion vervielfältigt eine DNA-Polymerase ein 143 Basen langes Produkt mit einer Verdoppelungszeit von 50 s, während die charakteristische Zeitskala der Falle 92 s ist.

Thermale Fallen sind somit ein vielversprechendes Beispiel dafür, wie ein Nicht-Gleichgewichtsprozess die Polymerisation und die Vervielfältigung der ersten Biopolymere begünstigt haben könnte - zwei notwendige Voraussetzung für die ersten molekularen Evolutionsprozesse.

Abstract

Biopolymers like RNA, DNA and proteins are the fundamental actors in all life on earth. It is however unclear, how the first RNA polymers with enzymatic activity could arise in a prebiotic scenario: Even in millimolar concentrations, ribonucleic acids only build short polymers with a length of 20 bases. This work demonstrates, how a reversible polymerization process can be enhanced with the help of a simple thermal gradient. Situated in an elongated compartment comparable to a hydrothermal pore it will create a convective fluid flow and also push biomolecules along the thermal gradient due to thermophoresis. The physical non-equilibrium setting of this so-called thermal trap is able to selectively accumulate longer polymers exponentially better than shorter polymers. Since the formation of longer polymers is coupled to higher local monomer concentrations, polymerization and thermal trapping are mutually self-enhancing. This process is described by a theory of trapped polymerization which is experimentally validated in this work. The results show that a pore height of 5 cm and a temperature difference of 10 K are sufficient to form RNA polymers longer than the shortest RNA based replicator.

The replication of genetic molecules is central to Darwinian evolution. This work demonstrates, how a thermal trap is able to drive an exponential replication reaction via thermal cycling and at the same time protects the replication products against outward diffusion into the diluted reservoir. In a proxy replication reaction, DNA replicating polymerase is able to double the amount of a 143 mer product each 50 s, while the time constant for accumulation is 92 s.

Thermal traps could therefore represent a possible non-equilibrium environment for the formation and replication of the first biopolymers - essential ingredients for the start of molecular evolution.

Contents

1 Introduction

1.1 Evolution of Life

The question of how life on earth originated is as old as humanity itself. Although multiple attempts have been made to answer this question in thousands of years in numerous cultures, the riddle could not be solved to this day. Yet, natural sciences of biological matter have emerged with high speed in the last 150 years and lead to a plenty of diverse theories on how and when life began on earth. One important step in this process of understanding life is the search for a definition of life. Based upon the striking similarity of common principles used by living systems on earth, one of the most valid definitions found so far is that *"Life is a self-sustaining chemical system, capable of Darwinian evolution"* [1]. This definition consists of three important parts: The self-sustainability has little to do with the living system itself but is essential to the process of life. Since external energy is always needed to increase the local complexity of the system, a living system will always depend on external boundary conditions in order to persist. The second point - life as a chemical system - emphasizes the importance of complex chemical reactions and molecular interactions that are essential for all living systems. The most striking part of the definition is the constraint for life to be capable of Darwinian evolution [2]. An entity that evolves in a Darwinian way is able to *replicate* itself, *mutates* at the same time and is then *selected* by its environment. According to this definition, a living system will gradually change its properties (geno- and phenotype) by chance. Entities of the living system that are more competitive than other mutants in terms of reproducibility and viability will therefore persist in the selective environment. The principle of Darwinian evolution is the key mechanism in the modern understanding of life, since it is the first and to this date most plausible approach to explain how life forms developed over millions of years provided that enough genetic and structural information about today's life forms are available.

As a direct consequence of Darwinian evolution the history of species may be plotted as a *tree of life* whose branches are the mutation events. This rooted tree of life started with simple organic molecules approximately 4 billion years ago and developed a remarkable complexity in its own structure (e.g. created by lateral gene transfer [3]) and its newest leafs, today's life forms. There are three different options to approach the question of the origin of life in this picture: The first option is to start a completely new tree using synthetic biology [4]. Complex systems, which do not necessarily have to be similar to existing biological systems, are created from scratch in the lab. If such artificial systems evolve in a Darwinian way, detailed insight into the processes of life could be obtained, since everything is under full experimental control. The second option is to pursue a top-down approach, embodied by the field of paleogenetics that was defined by Zuckerkandl and Pauling [5]. All available genetic material from fossil and living samples is taken together to reconstruct the historic traces of the tree of life, starting from the highest complexity and heading towards more and more ancient organisms. Since the phylogenetic analysis of modern organisms allows to infer the genetic sequences of ancient proteins, the latter can be recreated in e.g. *E. coli* bacteria and tested against environmental stress [6]. Via this method, detailed information on the optimal living conditions of the ancient life forms may be gathered,

leading to a more fundamental understanding of the evolution of organisms. The third method, prebiotic chemistry, is a bottom-up approach, which starts with exploring the first, simple and purely chemical organic systems [7]. Similar to synthetic biology, the tree of life is rebuilt from scratch, but this time using a system that is *plausible* in terms of the origin of life on earth. Here, plausible means that the known physical and chemical constraints of the early earth are taken into account. As a tradeoff, this method can handle only very simple molecular systems and tends to be speculative about the abundance of the involved chemicals. The foremost goal of this last approach is the experimental reconstruction of a plausible Darwinian system without biology, purely based upon basic molecular interactions.

1.2 The Molecular Origins of Life

The research on the molecular origins of life is based on the assumption that Darwinian evolution remains the driving force towards the tree of life, even for pure molecular systems. Therefore, molecules have to be found that are able to replicate their kind. This process should be efficient enough to not completely shuffle the genetic or structural information of the replicators but just slightly modify it in each repetitive cycle. This ensures further improvement by evolution. The important questions that arise are:

1. What are the chemical building blocks of these replicators?
2. How could these molecular replicators arise de novo?
3. How could replication be maintained without protective cells but in a highly diluted prebiotic aqueous world?
4. What was the basic energy source that fed replication and maintained a continuous non-equilibrium system?

The first question addresses a hen-egg problem between proteins and desoxyribonucleic acid (DNA). In modern biology, proteins or polypeptides are mostly used as very effective, nanometer-sized machines which carry out enzymatic functions e.g. in the metabolic pathways of cells or in the replication process of genetic information. This information is stored in DNA as a stable and reliable container which, however, does not show strong enzymatic activities like proteins. Therefore, both, DNA and proteins depend on each other while only their specialization allows the formation of complex life as it exists today. Since it seems improbable that both molecules have occurred simultaneously by chance in the very beginning, it is unclear how this mutual dependence was introduced. A plausible solution to this was given with the RNA-world hypothesis [8]. As a poly-nucleotide, ribonucleic acid (RNA) is able to store genetic information similar to DNA, but also shows enzymatic activities for e.g. self-splicing [9] or RNA polymerization [10, 11]. Additionally, RNA plays an important role in multiple key processes in modern life. Examples are the messenger RNA as an intermediate in the gene expression process, the transfer RNA that connects the RNA codon sequence to a specific, coupled amino acid and the ribosomal RNA, the enzymatic center of ribosomes that catalyzes the bonding of amino acids to polypeptides. Moreover,

the most important energy unit of biological organisms, ATP, is an RNA co-factor despite of the fact that its energy is stored solely in the high energy phophoanhydrid bonds. Since these examples are found in almost all life on earth, RNA must have played a central role right from the start.

Assuming that the first molecular replicator was made of RNA, the question on how this replicator was initially built remains. Recent studies on RNA replicators indicate that these molecules should have had a length of at least 200 nucleotides (nt) even in highly saline solutions [10]. Even if we set the correct sequence aside, this minimal length already represents a problem: the dissociation constant of ribonucleotides is estimated in the mM range. Thus, the initial monomer concentration needed for this task is much too high to be plausible in the prebiotic world. The first part of this work will therefore concentrate on this aspect and show how simple physical boundary conditions may enhance the polymerization of RNA without the help of enzymes, finally leading to complex structures that would not be possible in an equilibrium system according to the second law of thermodynamics.

Even if an RNA replicator could have been built de novo by simple chemistry and physics, it is still unclear, how this replicator was driven energetically. As the prebiotic RNA replication process is assumed to be template based, the problem of template poisoning arises after the first replication cycle. In a homogeneously and statically tempered system, the replicated strand only has a minor chance to unbind from the template strand since it is coupled to it by hydrogen bridge bonds. Even if this problem could be solved, the product strands will simply diffuse into the highly diluted, prebiotic bulk reservoir. The replication system will inevitably approach its steady state of lowest energy as well as maximal entropy and therefore die. The second part of this work will focus on how thermal energy flow inside hydrothermal pores could have been able to drive an replication process based on thermal cycling while at the same time protecting the product from outward directed diffusion.

Part I

Escalation of Polymerization in a Thermal Trap

2 Motivation and Goals

In modern life forms, complex metabolic systems gather free energy from their environment, mostly produced directly or indirectly by the sun. It is used to reduce their local entropy at the cost of heat emission or entropy creation of their environment. Life is therefore a local phenomenon that needs a continuing energy-driven non-equilibrium. However, the physical boundary conditions were different in the early days of (molecular) evolution. On the one hand, extrapolations of lunar and terrestrial impacts lead to the assumption that life could not have been formed more than 3.7 to 4 billion years ago on the earth's surface and not more than 4 to 4.2 billion years ago in protected sub-water sites like hydrothermal vents [12]. On the other hand, the earliest methagen was found to have existed approximately 3.5 billion years ago, pushing the abundance of the last universal common ancestor of all life forms (LUCA) before that time point [13, 14]. Since it is believed that LUCA already had lipid cell walls and a RNA based translation system, the available time span for the molecular origin of life shrinks significantly, making the sub-water / hydrothermal scenario the most plausible one for the first steps of molecular evolution.

To explore the chemical aspects of how the first complex biopolymers could have been built in such an environment, experiments were done starting from millimolar concentrations of energy-rich single nucleotides [15–17] and with the help of catalytic surfaces [18]. Despite the artificial chemical disequilibria used in experiments, the growth of polymers was demonstrated only up to a length of 20 nts, because the polymerization of RNA is inefficient ($K_D \sim$ mM) and limited by the hydrolytic dissociation of nucleotides [15]. In the prebiotic sub-water / hydrothermal setting, an a-priori assumption of chemical disequilibria cannot be made. This calls for a plausible, physical non-equilibrium system that is able to drive the chemical non-equilibrium for RNA polymerization towards long and functional molecules. The first part of this thesis will present a experimentally validated model that describes how a simple thermal gradient is able to boost the polymerization of RNA towards long polymers, even longer than the shortest known RNA replicators [19].

The discussed non-equilibrium system is a thermal gradient within an elongated, water-filled compartment - an abundant physical scenario in the prebiotic sub-water / hydrothermal setting. The compartment could be a pore in volcanic rock, a cleft of mud, or a rock fissure with the temperature gradient caused by the vicinity of a warm hydrothermal or volcanic outflow into a colder ocean [20, 21]. These conditions could be found in both salty oceanic hydrothermal conditions [22] and the fresh water near warm water ponds [23]. A thermal gradient in an elongated, water filled pore causes two orthogonal effects. The first effect is fluid convection, driven by gravitation and the temperature dependent volume expansion of the fluid (Fig. 1 a, circular arrows). The second effect is thermophoresis, the directed movement of solved (bio-)molecules along the thermal gradient (Fig. 1 a, horizontal arrows). The combination of both effects leads to a strong accumulation of the biomolecules at the bottom of the compartment. Since this trapping mechanism exponentially favors longer molecules over shorter ones [20], the simple thermal gradient finally leads to a length selective thermal molecule trap. In the laboratory, such traps have previously been demonstrated to support accumulation of biomolecules [24, 25], formation of cell-

like lipid vesicles [26] and concurrent replication and trapping with a polymerase [27, 28] (see part II). Additionally, a replication of codon information using tRNA is compatible with the temperature cycling in a thermal molecular trap [29]. This previous work mainly focused on the thermal trap as a passive length-selective concentration enhancer without biochemical reactions [24, 25] or with replicators that could not change the product length arbitrarily [26–28]. On the contrary, a non-terminated, reversible polymerization reaction shows arbitrary product lengths whose average value depends on the total local concentration of monomers (Fig. 1 b). Since in a thermal trap this concentration is exponentially dependent on the polymer length, polymerization and thermal trapping establish a mutual enhancing feedback loop (Fig. 1 c).

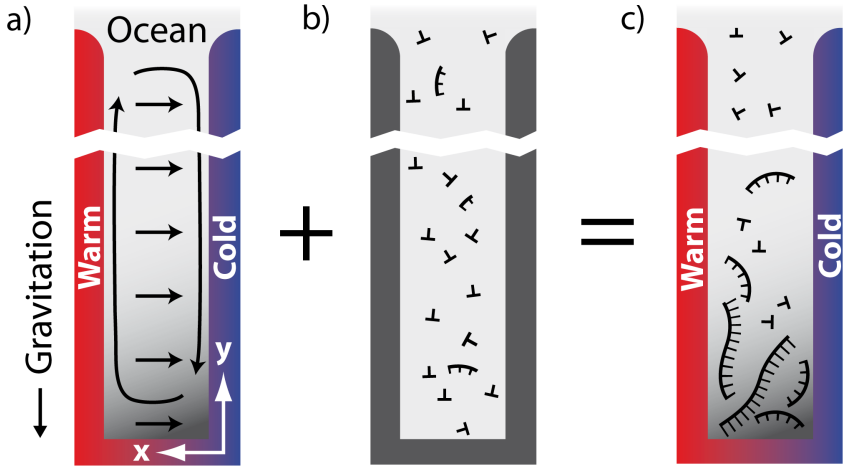

Figure 1: Proposed polymerization in a thermal gradient: Cross section of a water filled pore that is exposed to the ocean as an infinite reservoir at the top. Significant temperature differences between and across the pores are plausible in hydrothermal systems [20] . (a) Thermal trapping. The temperature gradient across the pore drives thermal convection due to gravitation and the thermal expansion/contraction of water at the hot/cold side (circular arrows). Additionally, solved biomolecules move along the thermal gradient due to thermophoresis via $v_T = -D_T \cdot \nabla T$ (e.g. horizontal arrows). If $D_T > 0$, as given for RNA/DNA in the conditions defined in this work (see Fig. 3), the combination of both effects leads to an accumulation of biomolecules at the bottom of the pore, exponentially dependent on their Soret coefficient $S_T = D_T/D$. As S_T increases with molecule length, longer molecules are trapped exponentially more efficient at the optimal trap width [27, 30]. (b) Polymerization. If reversible polymerization is in steady state the concentration of longer polymers decays exponentially with polymer length. The mean length strongly depends on the local total concentration of monomers and is too short to allow for self-replicating polymers under dilute primordial conditions. (c) Trapping and polymerization. The exponential thermal accumulation of monomers enhances the concentration dependent polymerization. The resulting longer polymers are exponentially better trapped which leads to a positive mutual feedback of accumulation and polymerization.

Spoken in terms of equilibrium, the thermal trap increases the total local concentration of monomers and therefore disturbs the chemical equilibrium of the polymerization represented by a certain steady

state length distribution. The relative timescales that define how fast the disturbed equilibria of the trap (physical) and the polymerization (chemical) will revert to their steady state determine how strong this mutual feedback and how long the resulting polymers will be. The case of very different timescales will be answered by the following theoretical considerations.

3 Theoretical Considerations

3.1 Model

3.1.1 Thermophoresis

Thermophoresis is defined as the directed movement of (bio-)molecules with a thermophoretic mobility D_T along a temperature gradient ∇T with the speed $\mathbf{v} = -D_T \cdot \nabla T$ [31]. Since this movement establishes a concentration difference, the diffusive mobility D of the particles also has to be taken into account which leads to a total flow density of

$$\mathbf{j} = \mathbf{j}_D + \mathbf{j}_{D_T} = -\nabla c \cdot D - c \cdot \nabla T \cdot D_T \tag{1}$$

The process is then described using the equation of continuity $\partial c/\partial t = -div\mathbf{j}$. In steady state, the resulting current will vanish ($\mathbf{j} = 0$) which leads to a relative equilibrium concentration distribution

$$c(T_1) = c(T_2) \cdot exp(-(D_T/D) \cdot (T_1 - T_2)) \tag{2}$$

between the temperatures T_1 and T_2 [32]. The ratio of the diffusive mobilities is defined as the Soret coefficient $S_T = D_T/D$ which describes the relative strength of thermodiffusion against the counteracting diffusive equilibration of the concentration gradient. For a small, quasi-constant temperature step under constant pressure, the depletion by thermophoresis may also be written using the Gibbs free energy G using a Boltzmann distribution [33]:

$$c(T_1) = c(T_2) \cdot exp\left(-\frac{(G(T_1) - G(T_2))}{kT}\right) \tag{3}$$

where k is denoted as the Boltzmann constant. For small thermal gradients $\nabla T < (aS_T)^{-1}$ compared to the hydrodynamic particle radius a, larger temperature differences may also be expressed by a successive application of Eq. 3. Comparison of Eq. 2 and Eq. 3 leads to $S_T \cdot kT = \Delta G/\Delta T = -S$ where S is the local negative entropy of the particle-solvent system. Taking into account the entropy of the hydration shell s_{hyd} per surface molecule area A and ionic contributions [33], this equilibrium model leads to:

$$S_T = \frac{A}{kT}\left(-s_{hyd} + \frac{\gamma\sigma_{eff}^2}{4\varepsilon\varepsilon_0 T} \times \lambda_{Debye}\right) \tag{4}$$

Here, γ is denoted as the relative change of the solvent's dielectric constant $\varepsilon(T)$ with temperature, σ_{eff} as the effective surface charge density and λ_{Debye} as the Debye-Hückel length. Obviously, the Soret coefficient increases with the particle surface and therefore the size of the molecule which is the reason for the length selectivity of thermal traps that are discussed now.

3.1.2 Thermal Trapping

The mechanism of thermal trapping was discovered by Clusius and Dickel in the beginning of the 20th century for the separation of different gases and isotopes by a thermal gradient in an elongated compartment [34]. In the sub-water scenario covered in this work (Fig. 1 a), the solvent is water and the solutes are biomolecules like ribonucleotides. In this water-filled pore, the vertically (y-axis) directed gravitation and the horizontally (x-axis) aligned temperature gradient ∇T lead to a laminar convective flow due to the thermal expansion of the fluid. Moreover, the dissolved bio-molecules with a thermodiffusion coefficient D_T will move along the thermal gradient according to $v = -\nabla T \cdot D_T$. For most charged molecules like RNA or DNA, D_T is positive (Eq. 4) and thermophoresis is therefore directed towards the cold side, where the molecules are pushed downwards to the trapping center at the bottom of the pore. To theoretically describe this process, the flow densities of Eq. 1 are expanded by a coupling term $\mathbf{j}_c$ which denotes the contribution to the convective flow $\mathbf{v}_c$:

$$\mathbf{j} = \mathbf{j}_D + \mathbf{j}_{D_T} + \mathbf{j}_c = -\nabla c(x,y,t) \cdot D - c(x,y,t) \cdot \nabla T(x,y) \cdot D \cdot S_T + \mathbf{v}_c(x)\, c(x,y) \tag{5}$$

As an approximation, the turning points of the convective flow are not considered, so that $\mathbf{v} = \mathbf{e}_y v(x)$ is constant along the vertical axis. Since the temperature gradient is assumed to be linear $\nabla T = \mathbf{e}_x \cdot \Delta T / w$ over the horizontal width w of the pore, the equation of continuity leads to the full two dimensional transport equation of the drift-diffusion type with $c(x,y,t)$ being the concentration of the solved biomolecules [30]:

$$\frac{\partial c}{\partial t} = D\left(\frac{\partial^2 c}{\partial x^2} + \frac{\partial^2 c}{\partial y^2}\right) + D \cdot S_T \cdot \frac{\Delta T}{w} \cdot \frac{\partial c}{\partial x} - v(x)\frac{\partial c}{\partial y} \tag{6}$$

From the equilibrium buoyancy forces in a volume element, Debye derived a x-dependent differential equation of the velocity in y-direction:

$$\frac{\partial^3 v}{\partial x^3} = \frac{-\beta g \rho \Delta T}{\mu w} \tag{7}$$

Here, β is denoted as the thermal volume expansion, g as gravitational acceleration, ρ as fluid density and μ as viscosity. For non slip boundary conditions, the convective flow between two large plates of different temperatures is calculated to be [19, 30] (see Fig. 12 d):

$$v_c(x) = -\underbrace{\frac{\beta g \rho \Delta T w^2}{6\mu}}_{v_0}\left(\frac{1}{2}\frac{x}{w} - \frac{3}{2}\frac{x^2}{w^2} + \frac{x^3}{w^3}\right) \tag{8}$$

which is then applied to Eq. 6. To solve the resulting differential equation, all variables are transformed to be non-dimensional by using $\tau \equiv Dt/w^2$, $q \equiv v_0 w/D$, $p \equiv S_T \Delta T$, $\eta \equiv y/w$, $\xi = x/w$. Eq. 6 then reads:

$$\frac{\partial c}{\partial \tau} = D\left(\frac{\partial^2 c}{\partial \xi^2} + \frac{\partial^2 c}{\partial \eta^2}\right) + p \cdot \frac{\partial c}{\partial \xi} + q \cdot f(\xi)\frac{\partial c}{\partial \eta} \tag{9}$$

with $f(\xi) \equiv \left(1/2 \cdot \xi - 3/2 \cdot \xi^2 + \xi^3\right)$. With a separation of variables $c(\xi,\eta) = U(\xi)V(\eta)$, the assumption of V to be exponential in η, $V(\eta) = exp(\alpha\eta)$ and of p to be small ($p \ll 1$), a steady state solution for concentration $c(\xi,\eta)$ can be written as

$$c(\xi,\eta) = \left(1 + p\left(-\xi + \frac{84pq}{10080+q^2}\left(\frac{1}{20}\xi^5 - \frac{1}{8}\xi^4 + \frac{1}{12}\xi^3\right)\right)\right) \times \exp\left(\frac{84pq}{10080+q^2}\eta\right) \tag{10}$$

This is plotted for a sample set of parameters in Fig. 12 e (see the work of Schink, Gerland and Debye [19, 30]). The maximal accumulation is found for $q_{opt} = \sqrt{10080} \sim 100$ yielding an exponent $\alpha_{max} \sim 0.42p$. With the transformation $q = v_0 w/D$ an optimal pore width $w_{opt} = q_{opt} D/v_0$ for a molecule species with a diffusion coefficient D is found. In this optimal case, the concentration ratio of biomolecules with a Soret coefficient S_T between the top c_{top} and the bottom c_{bottom} of a trap of height h reads $c_{bottom}/c_{top} = \exp\left(0.42 \cdot S_T \Delta T \cdot {}^{h}/_{w}\right)$. This illustrates the thermal trap's exponential selectivity on the length of the trapped molecules [20] and motivates the combination with a polymerization reaction that allows for arbitrary product lengths.

3.1.3 Polymerization

This work focuses on a non-terminated, fully reversible and linear polymerization reaction governed by the random aggregation and dissociation of polymers with arbitrary length, assuming that all bonds of the polymer are of equal strength. This is a plausible approximation for the polymerization of RNA, a linear polymer of similar nucleotides, held together by nearly identical phosphodiester bonds which are able to dissociate via hydrolysis at arbitrary binding sites. Following [19], the aggregation and dissociation of polymers of sizes i and j are described by the rates k_{ij}^{off} and k_{ij}^{on}, leading to a master equation for the concentration c_n of a polymer with length n :

$$P_i + P_j \rightleftharpoons P_{i+j} \; \forall (i+j) = n \tag{11}$$

$$\frac{dc_n}{dt} = \frac{1}{2}\sum_{i,j}\left(k_{ij}^{on} c_i c_j - k_{ij}^{off} c_{i+j}\right) \cdot \left(\delta_{i+j,n} - \delta_{i,n} - \delta_{j,n}\right) \tag{12}$$

For a closed and isolated system that has reached full equilibrium ${}^{dc_n}/_{dt} = 0 \; \forall n$, the net-flux of polymerization of two polymers with lengths i and j to a polymer of length $i+j$ vanishes. This represents a detailed balance condition between all polymerization states. In a thermal trap, the concentrations c_n are constantly changed by the in- and outflow of polymers from the bulk reservoir. Therefore the system described by Eq. 12 is not closed anymore. However, when the trapping timescale is much slower than

the timescale of polymerization $\tau_a \gg \tau_p$, the polymerization reaction has enough time to equilibrate after every perturbation of c_n by the trap. In the steady state of this quasi-closed system, detailed balance therefore reads

$$k_{ij}^{on} c_i c_j = k_{ij}^{off} c_{i+j} \; \forall i, j \tag{13}$$

with k_{ij}^{on} and k_{ij}^{off} still to be specified. The dissociation rate is expected to be temperature dependent but constant for all molecule lengths $k_{ij}^{off} = k^{off}$, since all polymer bonds are of equal strength. The same is correct for the on-rates $k_{ij}^{on} = k^{on}$ assuming that the polymerization is limited by chemical formation of the bond itself (reaction-controlled) and not by the diffusion of the reaction partners. The prebiotic RNA-polymerization is assumed to be reaction controlled. Therefore Eq. 13 leads to an exponentially decaying length distribution:

$$c_n = \frac{c_1^n}{(K_D)^{n-1}} \tag{14}$$

with $K_D \equiv {}^{k^{off}}\!/_{k^{on}}$ denoted as the equilibrium dissociation constant of the polymer bond. The complete distribution c_n is fully determined by the local steady state monomer concentration c_1 or the local total monomer concentration $c_0 \equiv \sum n c_n$ which will be used from now on, since it is a directly accessible parameter in the experimental model system. After numerical inversion, the polymer length distribution may also be written as $c_n(c_0)$ which is plotted in Fig. 2 as the relative frequency of polymers c_n/c_0 depending on the polymerization strength c_0/K_D . For concentrations lower than the dissociation constant, almost only monomers exist in equilibrium. Long polynucleotides are virtually non-existent in this regime.

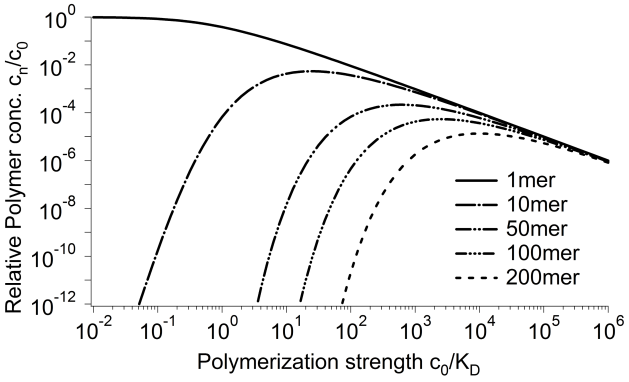

Figure 2: Relative frequency of polymers depending on the polymerization strength c_0/K_D . A monmer solution with the initial or total concentration $c_0 = \sum_n nc_n$ that obeys a fully reversible polymerization with a dissociation constant K_D will equilibrate towards an exponentially decaying length distribution. This distribution can be translated to relative frequencies to estimate threshold ratios of the polymerization strength for the appearance of of polymers with a given length. For instance, a 200mer will only appear for $c_0/K_D > 10^2$. Since the dissociation constant of RNA-polymerization was recently estimated to be in the higher µM to mM range [15], the emergence of long, potentially catalytic RNA polymers is improbable even under controlled experimental conditions [16, 17].

The experimental model system described below is not reaction but diffusion limited, so that the on-rates of polymerization scale with the diffusion coefficients of the reaction partners, $k_{ij}^{on} \propto (D(i) + D(j))$. Since k^{off} is independent of the molecule length and the monomer-monomer dissociation constant $K_{D,1,1}$ was measured separately (see Fig. 9), the monomer to n-mer dissociation constant is obtained with $K_{D,n,1}/K_{D,1,1} = (D(n) + D(1))/(2D(1))$. The remaining dissociation constants are defined via the detailed balance requirement that the product of equilibrium constants are the same along all pathways to a given multimerization state:

$$K_{D,n,m} = K_{D,n,1} \cdot K_{D,n+1,1} \cdot \ldots \cdot K_{D,n+m-1,1} \tag{15}$$

This results in the length distribution for a diffusion limited polymerization:

$$c_n = \frac{c_1^n}{\prod K_{D,1,x}} \tag{16}$$

As pointed out by S. Schink [35], the dependence of the average polymer length on the dissociation constant can be calculated by obtaining the zeroth momentum of length distribution. With $M_k = \sum_n n^k c_n$ defined as the k-th momentum of c_n, the mean length reads as:

$$\langle n \rangle = \frac{\sum_{n>0} nc_n}{\sum_{n>0} c_n} = \frac{M_1}{M_0} = \frac{c_0}{M_0}$$

For a reaction controlled system ($k_{ij}^{on} = k^{on}$), the steady state value of M_0 is then calculated by using

Eq. 12:

$$\begin{aligned} 0 = \frac{dM_0}{dt} &= \sum_n \frac{dc_n}{dt} \\ 0 &= \frac{1}{2}\sum_{n,i,j}\left(\frac{1}{K_D}c_i c_j - c_{i+j}\right)\cdot\left(\delta_{i+j,n} - \delta_{i,n} - \delta_{j,n}\right) \\ &= -\frac{1}{2K_D}\sum_{i>0} c_i \sum_{j>0} c_j + \frac{1}{2}\sum_{i,j>0} c_{i+j} \\ &= -\frac{1}{2K_D}M_0^2 + \frac{1}{2}\sum_n (n-1)\,c_n \\ &= \frac{M_0^2}{K_D} - M_0 + c_0 \rightarrow \\ \langle n\rangle &= \frac{2\cdot c_0/K_D}{\left(-1+\sqrt{1+4c_0/K_D}\right)} \end{aligned} \tag{17}$$

leading to $\langle n\rangle = \sqrt{c_0/K_D}$ for small K_D. This explains the threshold concentration K_D of the total monomer concentration c_0 to get longer polymers shown in Fig. 2.

3.1.4 Thermal Trapping and Polymerization

To approximate the solution of the given polymerization reaction inside a thermal trap, the solution of Eq. 12 given in Eq. 14 (RNA / reaction controlled) or Eq. 16 (Experiment / diffusion controlled) is used to calculate the effective diffusion coefficient

$$\bar{D} = \frac{\sum nc_n D(n)}{\sum nc_n} \tag{18}$$

and the effective Soret coefficient

$$\bar{S}_T = \frac{\sum nc_n S_T(n)}{\sum nc_n} \tag{19}$$

Here, $S_T(n)$ and $D(n)$ are the respective length dependent functions that have to be determined for the RNA-based system and the experimental model system. For RNA polymerization at 55 °C and 150 mM NaCl (Fig. 4), the Soret coefficient was found to fit $S_T(n) = \left(5.3+5.7n^{0.73}\right)\times 10^{-3}\mathrm{K}^{-1}$ while the diffusion coefficient matched $D(n) = 643n^{-0.46}\mu\mathrm{m}^2/\mathrm{s}$ [36–38]. In the experimental model system, $D(1)$ and $S_T(1)$ were measured separately and then extrapolated using the scaling laws presented in [33] which leads to $D(n) = 65n^{-0.75}\,\mu\mathrm{m}^2/\mathrm{s}$ and $S_T(n) = 0.1n^{0.5}\,\mathrm{K}^{-1}$. In the experiment each monomer was coupled to one fluorescent dye which defines the general measure of polymer concentration to be c_0, while $D(n)$ and $S_T(n)$ are weighted with nc_n instead of c_n. In the limit of fast polymerization ($\tau_p \ll \tau_a$), the effective values in Eq. 18-19 allow to calculate of the full polymerization reaction with a finite element solver (see chapter 4) for the experimental model system or with the purely numerical treatment as done for the RNA polymerization shown in chapter 3.2 ([19], SI Text A).

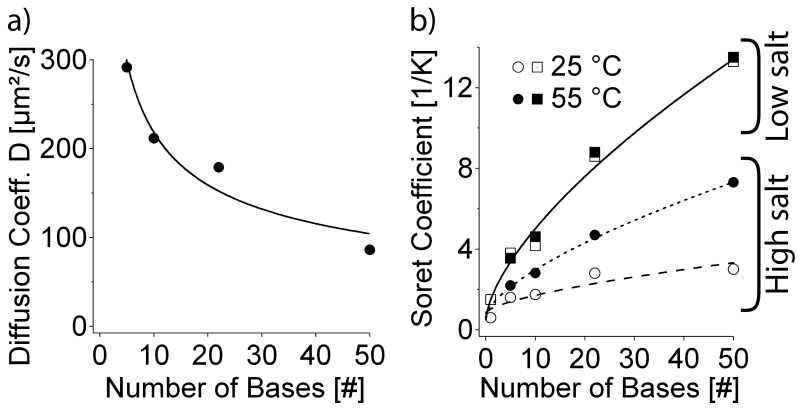

Figure 3: Diffusion and Soret coefficients of RNA. To extrapolate the polymerization and trapping theory to RNA-world conditions, the values for the diffusion constant D and Soret coefficient $S_T = D_T/D$ were previously measured for RNA-polymers of 1-50 nucleotides in [36]. (a) The diffusion constant D scales with $D = 643 \cdot n^{-0.46}\,\mu\text{m}^2/\text{s}$. (b) The Soret coefficient S_T was measured under high salt ($\lambda_{Debye} = 0.8\,\text{nm}$, $[NaCl] = 150\,\text{mM}$) and low salt ($\lambda_{Debye} = 5.6\,\text{nm}$, $[NaCl] = 3\,\text{mM}$) conditions at 25 °C and 55 °C. At 55 °C and high salt, the length dependent Soret coefficient could be fitted to $S_T(n) = \left(5.3 + 5.7 \cdot n^{0.73}\right) \times 10^{-3}\text{K}^{-1}$.

For these numerical calculations, the dissociation constant K_D was assumed to be temperature independent which is reasonable for temperature differences along the x-axis of $\sim 10K$ while the concentration differences along the x-axis were assumed to be in the order of $S_T \nabla T$ [19].

3.2 Results

The theoretical model of thermal trapping and polymerization is now extrapolated to the scenario of a hypothetical RNA-polymerization. A rectangular, elongated compartment as shown in Fig. 1 is considered as a thermal trap, while the boundary conditions are now exemplary fixed to a temperature difference of $\Delta T = 10\,\text{K}$ and a width of $w = 100\,\mu\text{m}$ which corresponds to the optimal trapping of RNA with a diffusion constant $D_{opt} \sim w \cdot v_0/100 = 42\,\mu\text{m}^2/\text{s}$ and an optimal polymer length of 377 nts (see chapter 3.1.2). The pore is further assumed to be coupled to an infinitely large ocean or pond that keeps the top boundary concentration at a fixed total monomer concentration $c_0 = 1\,nM$. As written above, the RNA-polymerization is assumed to be reaction controlled with a constant on-rate $k_{ij}^{on} = k^{on}$. k^{off} is assumed to be temperature independent (see chapter 3.1.4) and is an upper bound for long polymers in which hybridization may stabilize the bonds against breakage [39]. Two solvent conditions were taken into account, a salt deprived scenario (3 mM NaCl) independent from the absolute average temperature (see Fig. 3 and Fig. 7) as well as a salt enriched scenario (150 mM NaCl, physiological) at $T_{avg} = 25\,°\text{C}$ (Fig. 6) and $T_{avg} = 55\,°\text{C}$ (Fig. 4 and Fig. 5).

The most dominant approximation of the theory of thermal trapping and polymerization derived in chapter 3.1 is the separation of timescales between the trapping mechanism τ_a and the polymerization

reaction τ_p. While solutions with similar timescales $\tau_p \sim \tau_a$ turned out to be numerically intensive, the separated cases can be solved over a large parameter space (trap-height, K_D) which allows to use the theoretical model as a versatile tool set for different RNA-polymerization models. The lower bound of the trapping timescale $1/\alpha v_{max}$ for this specific trap is expected to be around 30 min, which defines the limit for $\tau_p \ll \tau_a$. The opposite limit in the separation of timescales $\tau_a \ll \tau_p$ is also taken into account by assuming that the fast thermal trap simply accumulates the existing length distribution from the bulk reservoir. Any perturbation of the polymer length distribution by association or dissociation of n-mers will lead to an immediate return to the original steady state that is solely defined by the exterior length distribution and the thermal trapping characteristics described in chapter 3.1.2. This approximation seems plausible but is still left to be validated theoretically. In the case of fast trapping or slow polymerization, the mutual enhancement of both effects does not exist. This allows to estimate the influence of positive feedback compared to the case of fast polymerization.

Fig. 4 a shows the length distribution in the chemical steady state of a fast polymerization reaction for pore lengths between 2.5 and 4 cm (black boxes 1-4) with a dissociation constant of $K_D = 10\,\mu M$ as an optimistic estimate with and without the continuing physical non-equilibrium of a thermal trap [15]. In the latter case, the exponentially decaying length distribution is clearly visible with dimer concentrations in the femtomolar range. In the former case with the thermal trap switched on, a pore height of 4 cm is already sufficient to create micromolar concentrations of 200 nts RNA-polymers. The total monomer concentration c_0 at the bottom of the trap is plotted in Fig. 4 b in dependence on the trap height. For ribonucleotides without the ability to polymerize the dashed line shows the exponential trapping characteristic known from chapter 3.1.2. Polymerizing monomers lead to an over exponential increase in the total monomer concentration at the pore bottom due to the length selectivity of the trap. The threshold for this behavior is the height at which the total monomer concentration overcomes K_D, leading to polymers with a length $n > 1$ and therefore an improved trapping efficiency. The effective Soret coefficient $\bar{S}_T$ becomes height dependent, so that the qualitative trapping efficiency can be described by $c_{trap}(h_{trap}) \sim exp\left(const. \cdot \overline{S_T}(h_{trap}) \cdot h_{trap}\right)$.

In Fig. 4 c, the numerical calculations are done for a broad range of dissociation constants. An exponential increase in K_D corresponding to a lower binding affinity is balanced by a linear increase in trap length at the cost of longer trap equilibration times, since all accumulated material priorly has to enter the trap by a slow, inward directed, diffusive transport process.

For slow polymerization $\tau_a \ll \tau_p$, Fig. 5 shows a similar but much less pronounced behavior. Due to the lack of a positive feedback between concentration dependent polymerization and length dependent accumulation, the deviation from the exponential trapping efficiency (Fig. 5 b) is solely explained by the simultaneous trapping of polymers of multiple lengths already present in the outer bulk reservoir, $c_{trap}(h_{trap}) \sim \sum_n n \cdot c_{n,bulk} \cdot exp(const. \cdot S_{T,n} \cdot h_{trap})$. Despite the missing mutual enhancement, a thermal trap with a height of 4 cm is still capable to accumulate 10 mers at micromolar concentrations given a dissociation constant for polymerization of $K_D = 0.1\,\mu M$. The qualitative behavior of mutual enhancement for fast polymerization also persists at 25 °C and high salt (Fig. 6) as well as in the low salt case

(see Fig. 7), compatible to the hydrothermal setting found in e.g. the Yellowstone lake [23]. The polymerization of long polymers by thermal traps is therefore a robust phenomenon compatible to a wide range of possible primordial conditions.

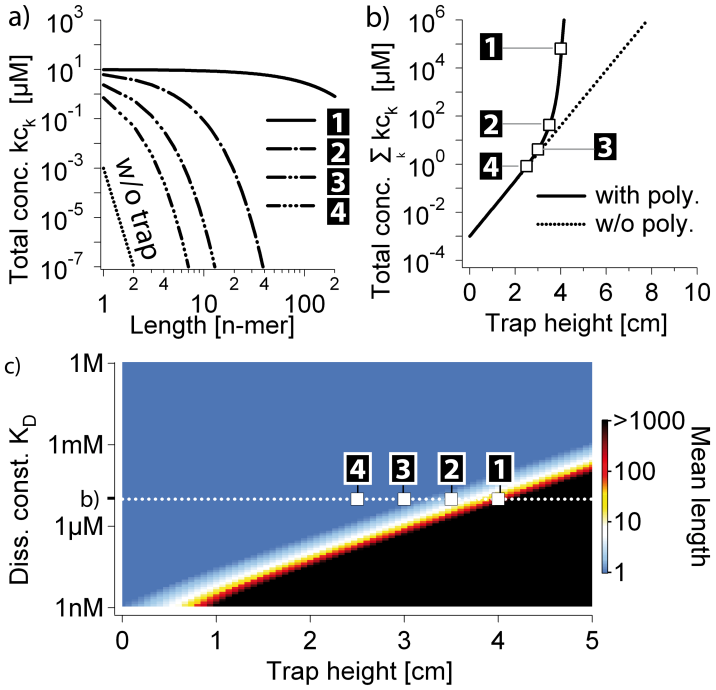

Figure 4: Generation of long RNA polymers at 55 °C and high salt at the bottom of a thermal trap by a fast polymerization reaction. Results of the theory of trapped polymerization at high salt ($\lambda_{Debye} = 0.8\,\text{nm}$, $[NaCl] = 150\,\text{mM}$) and high temperature conditions (55 °C) similar to oceanic hydrothermal pores comprising a polymerization reaction that is fast compared to the accumulation process inside the thermal trap ($30\,\text{min} \sim \tau_a \gg \tau_p$). The ribonucleotide concentration was chosen to be 1 nM with a reasonably high dissociation constant $K_D = 10\,\mu\text{M}$ [15]. (a) Length distribution of RNA-polymers inside thermal traps of 2.5 cm to 4 cm length (black boxes 1-4) at a trap width of 100 µm and a temperature difference of 10 K. Oligomers with the size of active RNA enzymes are predicted to exist already at moderate trap heights. (b) Escalation of polymerization. Compared to the thermal trapping of monomers not able to polymerize, the process of trapped polymerization will exceed the exponential height dependence $c\,(h_{trap}) \sim exp\,(const. \cdot \overline{S_T} \cdot h_{trap})$ shown in [20, 30]. The length averaged Soret coefficient $\overline{S_T}$ changes with a changing polymer length distribution and the polymerization is dependent on the local total concentration of trapped monomers $c_0\,(h_{trap})$. Thus, the exponent of the trapping characteristic $c\,(h_{trap})$ gets non linear, leading to $c_{trap}\,(h_{trap}) \sim exp\,(const. \cdot \overline{S_T}\,(h_{trap}) \cdot h_{trap})$. (c) The expected mean length of trapped polymerization is plotted against the dissociation constant K_D and the height of the thermal trap. For a wide range of dissociation constants, a transition point of trap height may be found where the polymerization escalates (here: black box 1, $h_{trap} = 4\,\text{cm}$ for $K_D = 10\,\mu\text{M}$). It is expected that beyond this transition point, the accumulation process is limited by the finite inflow of fresh monomers which will greatly increase the time to reach the steady state plotted here. For a polymerization slower than the accumulation, a similar but less pronounced behavior is found (Fig. 5). To conclude, the escalated growth of RNA-length by a thermal trap is shown to be a robust phenomenon.

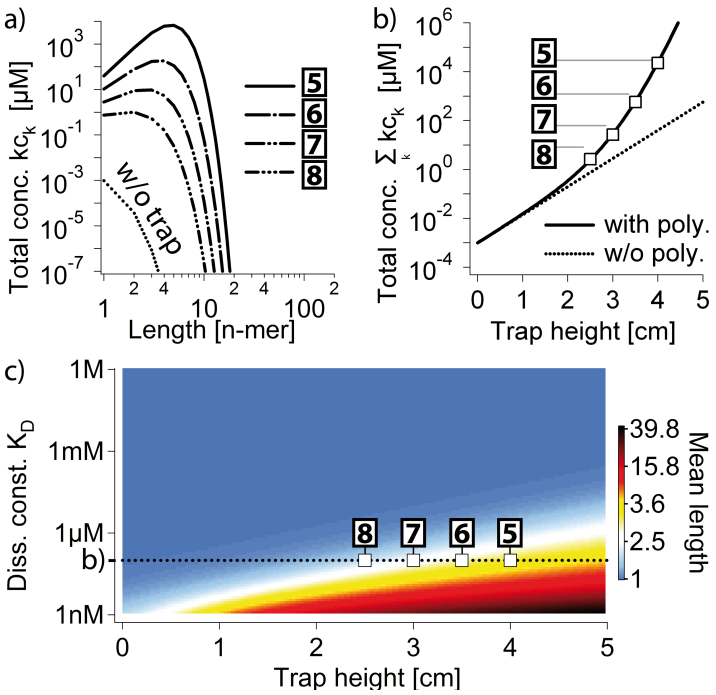

Figure 5: Slow RNA polymerization at 55 °C in high salt at the bottom of a thermal trap. Results of the theory of trapped polymerization at the same conditions used in Fig. 4 with a temperature difference of 10 K across the trap at 55 °C average temperature, 1 nM monomer concentration and $K_D = 0.1\,\mu M$, but under the assumption of slow polymerization timescales $\tau_p \gg \tau_a \sim 30\,min$. As an approximation, the trap is simply thought to accumulate the steady state length distribution found in the bulk ocean [20, 27, 30]. Any change in the trapped length distribution by polymerization will lead to an instant return to the original steady state by trap-driven out- and inflows of polymers. (a) Length distribution of RNA-polymers for different trap heights. Longer molecules are still built, but much less than in the case of fast polymerization. The thermal trap only accumulates the polymer length distribution of the bulk ocean and does not benefit from a polymerization inside the trap. Therefore, no feedback mechanism is present in contrast to the case shown in Fig. 4. (b) Slow polymerization also shows an accumulation characteristic greater than exponential compared to the trapping of a pure monomer solution. The accumulated total concentration of monomers may now be described by the sum of independent accumulations over all polymer lengths $c_{trap}(h_{trap}) \sim \sum_n n \cdot c_{n,bulk} \cdot exp(const. \cdot S_{T,n} \cdot h_{trap})$. The difference to Fig. 4 b can be explained by the absence of the mutual enhancement of polymerization and trapping. (c) The average polymer length is plotted against the dissociation constant K_D and the height of the thermal trap. While the transition range to larger polymers is broadened compared to the case of fast polymerization, the trap is still able to accumulate enough large polymers out of the bulk steady state length distribution to significantly increase the mean length to values more than 30 monomers.

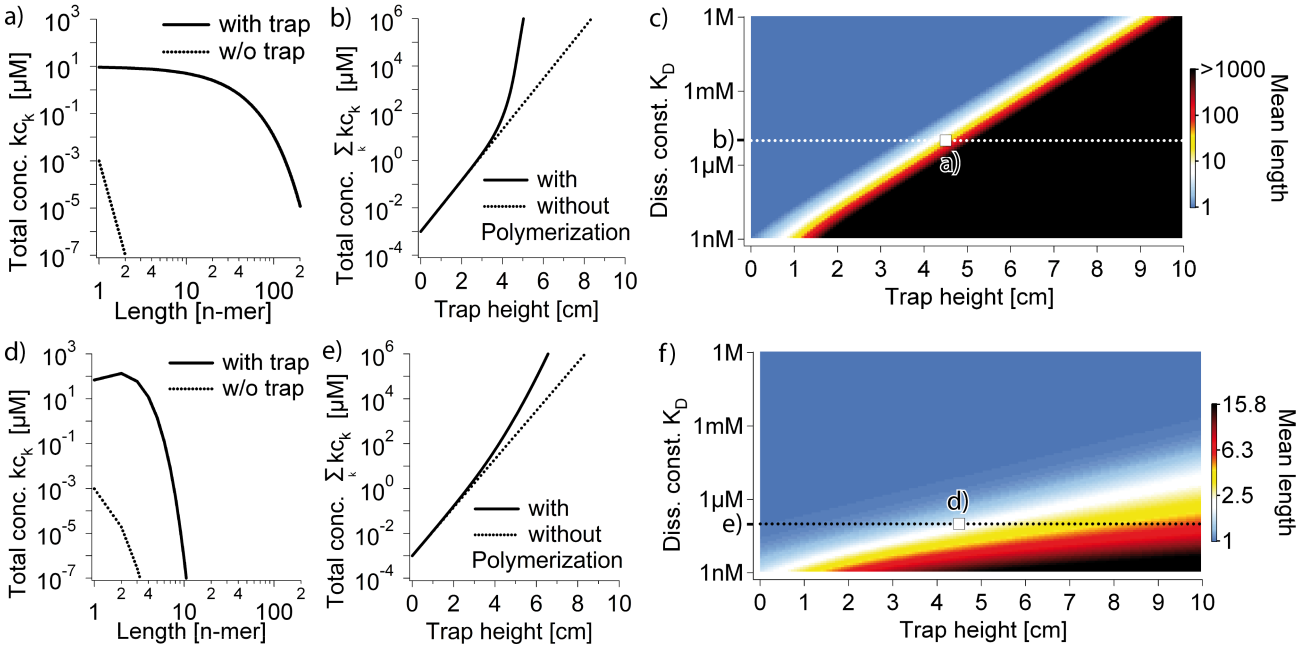

Figure 6: RNA polymerization at 25 °C and low salt at the bottom of a thermal trap. Accumulation inside a primordial geothermal pore at 25 °C and 150 mM KCl ($\lambda_{Debye} = 0.8\,\text{nm}$): colder, but otherwise identical to Fig. 4 and Fig. 5. (a) Length distribution of a polymer inside a 4.5-cm long trap, with a temperature difference of 10 K and an RNA dissociation constant $K_D = 10\,\mu\text{M}$. Oligomers the size of active ribozymes are predicted in the trap. (b) The trap efficiency outreaches the exponential trapping characteristics of monomers when the pore height is large enough to accumulate a local total monomer concentration larger than K_D. (c) Mean polymer lengths for varying pore heights and dissociation constants. For every plausible K_D, a trap height exists at which polymerization takes place. (d-f) Extrapolation towards the slow reaction limit, using the identical trap and $K_D = 0.1\,\mu\text{M}$. Again, the trap is able to accumulate long polymers out of the bulk solution without the help of in-trap polymerization which lead to mean lengths around 10 monomers. The advantage of the mutual enhancement of polymerization and trapping shown in (a-c) against the pure accumulation of a polymer mixture shown here is clearly visible by a steeper polymerization transition towards greater trap heights / smaller K_D.

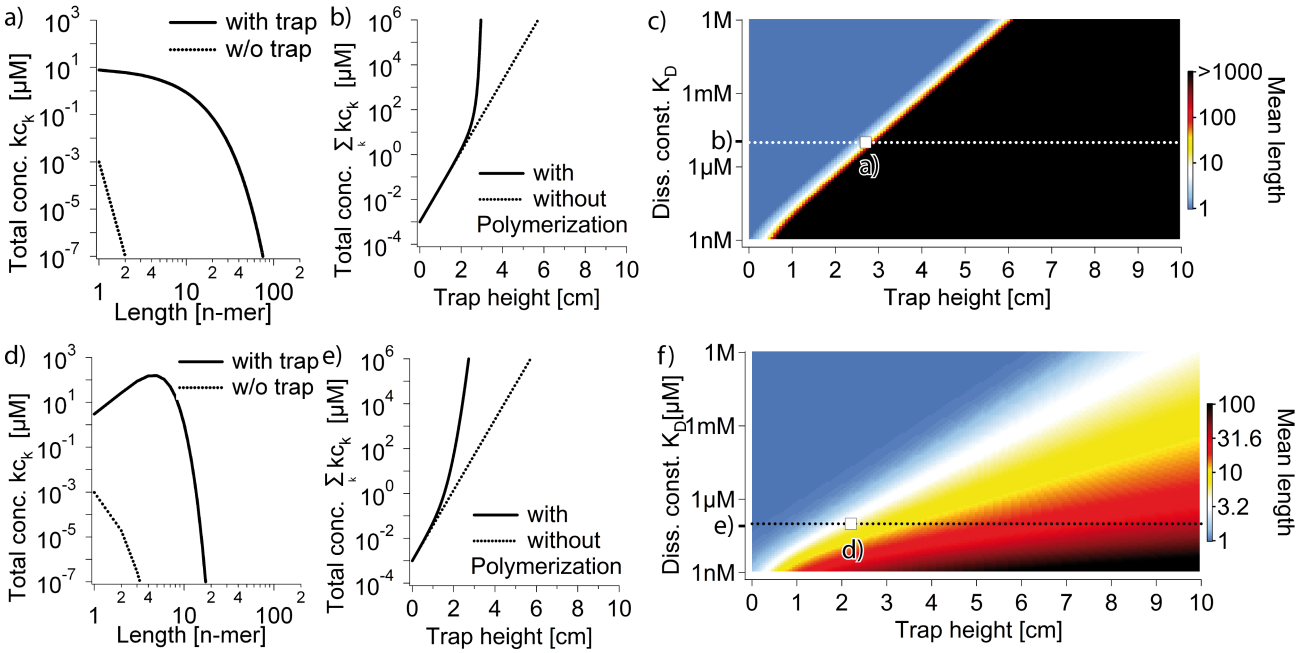

Figure 7: RNA polymerization at 55 °C and low salt at the bottom of a thermal trap. Accumulation inside a primordial geothermal pore surrounded by fresh water (55 °C, mM KCl, $\lambda_{Debye} = 5.6\,\text{nm}$) and with lower salt concentration but otherwise identical to Fig. 4 and Fig. 5. The temperature dependence is small (Fig. 3). (a) Length distribution of a fast-reacting polymer inside a 2.7-cm-long trap, with temperature difference 10 K and RNA dissociation constant $K_D = 10\,\mu\text{M}$. The steady state is reached after 100 years and oligomers the size of active ribozymes are predicted in the trap. (b) The trap efficiency outreaches the exponential trapping characteristics of monomers when the pore heights are large enough to accumulate a local total monomer concentration larger than K_D. (c) Mean polymer lengths for varying pore heights and dissociation constants. For every plausible K_D, a trap height exists at which polymerization takes place. (d-f) Extrapolation towards the slow reaction limit, using the identical trap and $K_D = 0.1\,\mu\text{M}$. Again, the trap is able to accumulate long polymers out of the bulk solution without the help of in-trap polymerization, leading to mean lengths around 30 monomers. The advantage of the mutual enhancement of polymerization and trapping shown in (a-c) against the pure accumulation of a polymer mixture shown here is clearly visible by a steeper polymerization transition towards greater trap heights / smaller K_D.

4 Experimental Realization

4.1 Experimental Model

4.1.1 Polymerization

The theoretical model demonstrates how thermal traps are capable of enhancing polymerization reactions even in the unfavorable prebiotic boundary conditions. Low monomer concentrations and binding affinities are balanced by the traps length selective accumulation and allow for the build-up of RNA-polymers longer than the shortest estimated replicators [10]. This chapter will focus on the experimental validation

of the derived theory with a polymerizing model system that allows for a complete control of all relevant parameters like the temperature dependent dissociation constant of the polymer bond $K_D(T)$, the temperature profile, the convection flow speed, the diffusion coefficient D and the Soret coefficient S_T. In existing RNA-polymerizing systems real-time measurements in the picoliter volumes of the trap via, e.g. fluorescence microscopy are not possible due to the small size of the monomers. We therefore employed an experimental model system that meets all theoretical constraints: A 95 base pair block of double stranded DNA acts as a monomer. The dsDNA block is flanked by a self-complementary, single stranded DNA-piece of 25 nucleotides at each end (Fig. 10 a, Tab. 1). The monomers are stable under experimental conditions ($T_m \sim 85\,^{\circ}\mathrm{C}$) and reversibly bind to each other via their ssDNA ends to form longer linear polymers. The length and GC-content of the sticky ends defines the polymerization affinity K_D which has previously been measured in a melting curve experiment (Fig. 9) [40]. The polymerization kinetics were measured in advance to be in the order of $\tau_p \sim 10\,\mathrm{s}$ while the trapping timescales of the experiment are in the range of $\tau_a \sim 1\,\mathrm{h}$. Although DNA was used, this experimental realization does cover all aspects of the polymerization theory from chapter 3.1. To measure the degree of polymerization, the sticky ends were labeled with complementary fluorophores, the so called donor and acceptor. When a bond is formed, both dyes come into close proximity. The donor dye is quenched by the fluorescence resonance energy transfer (FRET) to the acceptor dye with a rate $k_{ET} = R_0^6/\left(\tau_D \cdot r^6\right)$, with the lifetime of the excited donor state τ_D, the donor acceptor distance r and the Förster radius R_0 at which the energy transfer from donor to acceptor is by definition 50 % [41]. Due to the $1/r^6$-dependence on the fluorophore distance, FRET is an ideal tool to accurately measure distances in the order of R_0, ranging from 1 nm to 10 nm in single molecule experiments. The characteristic radius R_0 depends on the spectral overlap of donor and acceptor via $R_0^6 \propto \int f_D(\lambda)\,\varepsilon_A(\lambda)\,\lambda^4 d\lambda$ with the emission intensity of the donor $f_D(\lambda)$ and the extinction coefficient of the acceptor $\varepsilon_A(\lambda)$. In this work carboxy-X-rhodamine (ROX) was used as a donor and fluorescein amidite (FAM) as an acceptor for which the fluorescence spectra are shown in Fig. 8. Since FRET is a dipole-dipole interaction, the rate of energy transfer also depends on the relative orientation of the fluorophores described by the orientation factor $\kappa^2 = (\cos\theta_{DA} - 3\cos\theta_D \cos\theta_A)^2 \propto R_0^6, k_{ET}$. Here, θ_{DA} denotes the relative angle between donor and acceptor and θ_D or θ_A is denoted as the angel of the donor or acceptor dipole to the connecting vector of both dyes. As the experiments were performed in bulk and not for single molecules, neither κ nor R_0 are accessible. Instead, the ensemble average of the FRET efficiency

$$FRET \equiv \frac{Transferred\,Energy}{Complete\,Excitation\,Energy} \sim k_{ET}/(k_{ET}+k_f) \tag{20}$$

of all dye molecules inside a volume element defined by the reaction chamber width, the microscope magnification and resolution and the binned pixel size of the CCD-camera are measured. Here, k_f is denoted as the rate of the donor's direct fluorescence emission. Due to the $1/r^6$-dependence of the the energy transfer rate on the distance of the dyes or sticky ends, it is further assumed that non-polymeric intermolecular FRET will not occur for µM to mM concentrations of water solved monomers. Preliminary

results show that this assumption has to be abandoned under certain conditions at which massive gel-like structures assembled inside the measurement chamber (shown in chapter 4.3). Polymer cyclization is neglected since the maximum relative amount of cyclic DNA is expected to be 4 % at a length of 150 bp as shown by Podtelezhnikov et al. [42]. Therefore only the monomer is prone to form cyclic products of 120 bp, which adds a false positive signal to the average polymer length. Additionally, Podtelezhnikov et al. used ligation enzymes that shift the polymerization equilibrium and accordingly pronounce cyclization compared to the reversible bond used in this work.

To obtain the FRET-efficiency corresponding to the mean polymer length $\langle n \rangle = \frac{1}{(1-FRET)}$, the polymers solution is exposed to light of the excitation wavelength of the donor (D: 482 nm) or acceptor (A 586 nm). The emitted light is split into two beams with the wavelength of the donor emission (D: 536 nm) and the acceptor emission (A: 630 nm) that are then recorded via a CCD-camera (details see below). Taking into account all combinations of excitation and emission wavelengths, four channels can be recorded (Tab. 2) of which the channel *AD* was omitted since Anti-Stokes scattering is assumed to be negligible. According to Eq. 20 the uncorrected, non-normalized, ensemble averaged FRET ratio is $FRET_{nn,nc} = DA/AA$. In this idealization, only closed bonds contribute to the channel *DA* while the channel *AA* is proportional to the local total monomer concentration c_0. Since the average is taken from $\sim 10^4$ molecules and an exposure time of 500 ms, fluctuations of the orientation factors and from different dye-to-dye distances are assumed to center at a constant mean value.

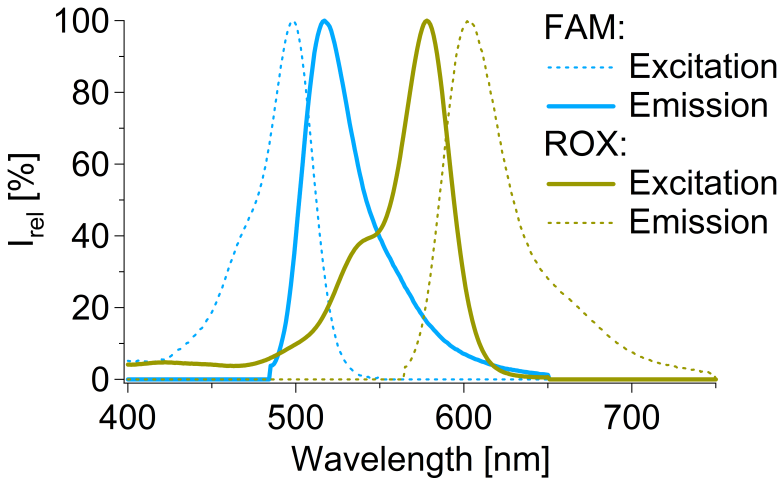

Figure 8: Fluorescence spectra of ROX and FAM. The spectral overlap $J \propto \int f_D(\lambda)\,\varepsilon_A(\lambda)\,\lambda^4 d\lambda$ between the acceptor (ROX) and donor dye (FAM) allow for fluorescence resonance energy transfer (FRET): After the excitation of the donor by light, its energy is transferred to the acceptor with a rate k_{ET} increasing with $\propto 1/r^6$ for smaller dye-to-dye distances r. Source: Invitrogen [43].

Name	Sequence
DNA_A	*3´TGTGAGACCCCCGGGTCACTGATGAGGAGGAGCTGCGGACTCCCGTGAACCAGAACTCTCGG GGAATCCATCAACTTGGCCGGTAAGGGGTCCCG - CAATAACGTG(**ROX**)ACGTACATCGGGACT 5´*
DNA_B	*5´GTTATTGCAC(**FAM**)TGCATGTAGCCCTGA - ACACTCTGGGGGCCCAGTGACTACTCCTCCTC GACGCCTGAGGGCACTTGGTCTTGAGAGCCCCTTAGGTAGTTGAACCGGCCATTCCCCAGGGC 3´*
$DNA_{A'}$	*3' TGTGAGACCCCCGGGTCACTGATGAGGAGGAGCTGCGGACTCCCGTGAACCAGAACTCTCGG GGAATCCATCAACTTGGCCGGTAAGGGGTCCCG - ACCCAGCTGCGAATGATTGAATACG 5'*
$DNA_{B'}$	*5' CATATGCCACATTCATTGGTGGCTG - ACACTCTGGGGGCCCAGTGACTACTCCTCCTCGAC GCCTGAGGGCACTTGGTCTTGAGAGCCCCTTAGGTAGTTGAACCGGCCATTCCCCAGGGC 3'*
H3	$DNA_A + DNA_B$ annealed.
H2	$DNA_A + DNA_{B'}$annealed.
H1	$DNA_{A'} + DNA_B$ annealed.

Table 1: Sequences of oligonucleotides used for the reversible polymerization. DNA_A and DNA_B consist of a complementy part (95 bp) and two opposing self-complementary sticky ends (25 bp) with corresponding FRET fluorophores at the central position. Via annlealing, both DNA oligomers self-assemble to the dsDNA-block H3, the monomer (Fig. 10 a). $DNA_{x'}$ is identical with DNA_x, except for the sticky ends which are not labelled and randomized but of the same GC content. Annealing $DNA_{x'}$ and its labeled counterpart leads to a monomer acting as polymerization chain terminator ($H2 : x = B$, $H3 : x = A$). Annealing was done with a cooling rate of 1 °C/10s from 95 °C to 10 °C.

Channel	Excitation	Emission	Monomer labeling	Polymerizing monomer
DA	FAM 482 nm	ROX 630 nm	ROX / FAM	Yes
DD	FAM 482 nm	FAM 536 nm	ROX / FAM	Yes
AA	ROX 586 nm	ROX 630 nm	ROX / FAM	Yes
AA_A	ROX 586 nm	ROX 630 nm	ROX	No
DD_D	FAM 482 nm	FAM 536 nm	FAM	No
DA_D	FAM 482 nm	ROX 630 nm	FAM	No
DA_A	FAM 482 nm	ROX 630 nm	ROX	No
$dd(T)$	Crosstalk ratio by donor $DA_D(T)/DD_D(T)$			
$aa(T)$	Crosstalk ratio by acceptor $DA_A(T)/AA_A(T)$			

Table 2: Description of the fluorescence channels used to measure the FRET ratio. The distinct fluorescence channels are named after the pattern NM_x. The letter N (M) denotes the excitation (emission) wavelength (D: donor; A: acceptor). The index x denotes which dyes were used for monomer labeling (no index: labeled with both dyes). Example: To record channel DA_A, the probe was only labeled with the acceptor, excited with light of the donor excitation wavelength and read out with a filter set that matches the acceptor's emission wavelength.

As shown in Fig. 8 the emission and excitation spectra of donor and acceptor show unfavorable overlaps, known as crossover or bleed-through, which have to be corrected. The first crossover effect is caused by the direct excitation of the acceptor with light of the donor's excitation wavelength. To quantify this effect, a modified, acceptor labeled monomer was designed to act as a polymerization chain terminator that could not form any polymers. It was tested in the same solution used for the main exper-

iments (see chapter 4.2 and 4.3). The temperature dependent crossover ratio $aa(T) = DA_A(T)/AA_A(T)$ was measured to correct the absolute bleed-through value $DA_A(T)$ at a given total monomer concentration defined by $AA_A(T)$. The second crossover $dd(T) = DA_D(T)/DD_D(T)$ is caused by the direct emission of the donor dye into the acceptor emission channel and measured analogous with a donor labeled, chain terminating and therefore non-polymerizing monomer. Taking into account these major crossover contributions, the non-normalized FRET ratio then reads:

$$FRET_{nn} \equiv \frac{DA(T) - dd(T) \cdot DD(T) - aa(T) \cdot AA(T)}{AA(T)} \tag{21}$$

Normalization between 0 and 1 is needed to correct for the different quantum efficiencies of the dyes and the transmittance of the used filter sets:

$$FRET(t,x,y) \equiv \left(\frac{DA(t,x,y) - dd(T(x,y)) \cdot DD(t,x,y) - aa(T(x,y)) \cdot AA(t,x,y)}{AA(t,x,y)} - \alpha \right) / \beta \tag{22}$$

with α as $\min(FRET_{nn}(T))$ and β as $\max(FRET_{nn}(T)) - \alpha$.

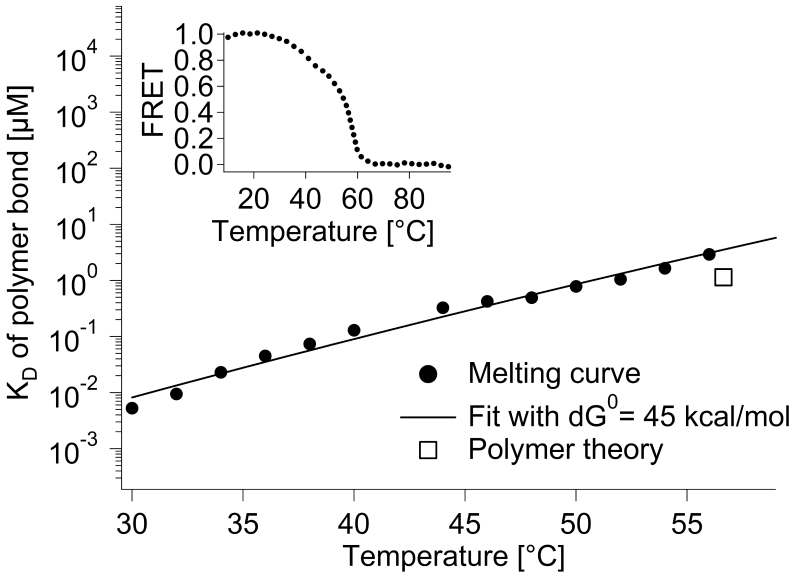

Figure 9: Melting curve measurement of the polymerization dissociation constant. The dissociation constant was measured independently from the polymerization experiment via melting-curve analysis [40]. A modified version of the monomer was used that can only build dimers without any changes in the sequence of the sticky ends that form the bond. The amount of dimers was again determined by the FRET ratio defined in Eq. 22. The measured dissociation constant for the temperature in the polymerization experiment matches $K_{D,polymer} \sim 1\,\mu M$ reasonably well, which was obtained by fitting the experimental data in Fig. 14 b.

One important parameter used in the polymerization theory derived in chapter 3.1.3 is the dissociation constant K_D of the polymer bond. To exclude side effects from the formation of longer polymers, two

separately annealed solutions H2 and H1 that can only form dimers (see Tab. 1) were mixed at equal concentrations of 2 µM in the same buffer (PBS) and reaction chamber as used in the main experiments (see chapter 4.2 and 4.3). The FRET-ratio (Eq. 22) was then measured in a temperature range around the melting temperature $T_m \sim 55\,°\mathrm{C}$. The dimerization process of the two monomers H_1 and H_2 defined in Tab. 1 is described by $H_1 + H_2 \rightleftharpoons H_{12}$ with H_{12} being the dimer construct. Since the normalized FRET-ratio is equal to the relative amount of closed bonds $\theta(T)$, we get in steady state:

$$K_D = \frac{(1-\theta(T))^2 c_0}{\theta(T)} \tag{23}$$

with c_0 denoted as the initial concentration of H1 and H2 (see Fig. 9) [40]. to fit the data obtained by Eq. 23, the relative transition rates of the dimeric and monomeric state are determined by their free energy difference ΔG^0 under standard conditions $k^{off}/k^{on} = K_D(T) = \exp\left(-\Delta G^0/RT\right)$. The fitted value $\Delta G^0 = 45\,kcal/mol$ matches the calculated one within an error margin of 10 % [44].

4.1.2 Thermal Trap

The experimental realization of the thermal trap used in this work is shown in Fig. 10 b [19, 27]. An elongated borosilicate capillary (Vitrocom) with a rectangular cross section of 50 µm x 100 µm is used as reaction chamber. It is sandwiched between an infrared-transparent and heat conducting silicon wafer and a sapphire-coverslip within a layer of immersion oil to improve thermal and optical characteristics. The silicon wafer is cooled with thermoelectric elements (9502/065/018M; Ferrotec) at a constant offset temperature $T_{pelt} = 10\,°\mathrm{C}$ for trapping experiments or scanned through a temperature range of 10 °C to 95 °C for melting curve experiments. The aqueous solution inside the capillary is heated from the bottom using an IR-laser (TLR-20-1940; IPG Photonix, 20 W). The laser is focused with a custom-built scanner lens system that provides a constant spot diameter of 30 µm along the full scan range of 7 mm [19]. Prior to this, the laser beam is deflected by a set of galvo-electric scanning mirrors (6200-XY; Cambridge Technology) to move along the capillary's y-axis in its center. The fast, repetitive movement of the laser spot with the frequency f along a fixed route leads to continuing temperature changes ΔT at every point of the scanning pattern. Accordingly, it creates a thermoviscous flow with a fluid speed $v \sim \Delta T^2 \cdot f \cdot \beta \cdot \varsigma \cdot b$ with the temperature dependence of the fluid viscosity ς and the width of the spatial heat distribution b which is assumed to be Gaussian for moderate f [45]. This system was favored over a gravitationally driven thermal trap since the fluid speed can be adjusted directly via the scanning frequency f or by introducing an inverted, intermediate laser pattern while leaving the temperature distribution in the reaction chamber unchanged. Both, the temperature gradient and the fluid flow inside the capillary are therefore created as well as decoupled by the absorption of the moving IR laser spot. The key benefit of this method is that the optimal velocity can be set independently of the temperature gradient or the capillary geometry which is much cheaper than using different custom-built capillaries for biomolecules with different diffusion constants D. The specific laser pattern used in the trapping experiments created four symmetric convection rolls, equivalent to four thermal traps

that are connected at their hot / bottom sides (Fig. 12 a and Fig. 10 c: Flow). The superposition of the convective fluid flow and temperature profile (Fig. 10 c: Temp) leads to four symmetric accumulation sites (Fig. 10 c: Conc). The theoretical treatment of chapter 3.1.2 also applies to this experimental realization except for an introduced non-slip boundary condition at the hot capillary walls plotted in Fig. 12 d:

$$v(x) = -v_0 \left(6\frac{x}{w} - 15\frac{x^2}{w^2} + 8\frac{x^3}{w^3} \right) \tag{24}$$

The analogous treatment to chapter 3.1.2 leads to the theoretical steady state concentration distribution inside the trap:

$$c(\xi,\eta) = \left(1 + p\left(-\xi + \frac{189pq}{1260+38q^2} \left(\frac{2}{5}\xi^5 - \frac{3}{4}\xi^4 + \frac{1}{2}\xi^3 \right) \right) \right) \times \exp\left(\frac{189pq}{1260+38q^2}\eta \right) \tag{25}$$

The optimal accumulation efficiency is obtained for $q_{opt} \sim 5.8$ which yields $\alpha_{opt} = 0.43p$. Solutions of both trapping scenarios with slip (Eq. 25) and non-slip (Eq. 10) are plotted in Fig. 12 e. They show only slight differences which theoretically confirms the experimental laser driven trap as a valid model for a thermogravitational trap. However, even with optimized convection speeds the relaxation time of the experimental trap is in the order of years, since most of the trapped material has to enter the thermal trap by inward directed diffusion. To overcome this issue, the capillary was connected to a high-precision syringe pump (neMESYS; Cetoni) on one side which created a constant low-speed inflow of fresh monomers. At the cost of the final steady state trapping efficiency the relaxation time was reduced to the order of months which allowed to record the complete separation of material inside the trap within experimentally feasible timescales (Fig. 13). All fluid flow velocities were measured by tracking fluorescently labeled beads (1 µm diameter, F8888, Invitrogen, Fig. 10 c: Flow).

To read out all fluorescence channels as defined in Tab. 2, the capillary was imaged from the top with a fluorescence microscope (Axiotech; Zeiss) using a set of high-power light-emitting diodes (LEDs) for alternating color excitation (blue: 590 nm and amber: 470 nm; Thorlabs) and a 40 x objective (Plan-Neofluar 40 x 0.9 NA; Zeiss). The emitted light was color-separated by a dual view unit (Optosplit II; Cairn Research) and then recorded by a CCD-camera (Sensicam; PCO). Since the concentration of fluorescent molecules inside the trap varies across several orders of magnitude, each excitation channel (blue, amber) was recorded with three different illumination intensities (10 mA, 20 mA and 80 mA) to improve the signal's dynamic range. With dual excitation and dual emission, six CCD-frames and 12 images were recorded for each frame time.

The temperature profile $T(x,y)$ inside the capillary was measured using the temperature dependent fluorescence of the dye 2´,7´–bis–(2–carboxyethyl)–5–(and–6)–carboxyfluorescein (BCECF) that was previously calibrated using thermoelectric elements. Prior to each trapping experiment, $T(x,y)$ was also measured inside the monomer solution by switching off the thermoviscous fluid flow at an unchanged temperature situation: The initial movement of the IR-laser was made symmetric which results in a vanishing net flow inside the capillary at constant IR-absorption. To estimate the temperature, the resulting

FRET-ratio is compared to the melting curve experiments shown in Fig. 9.

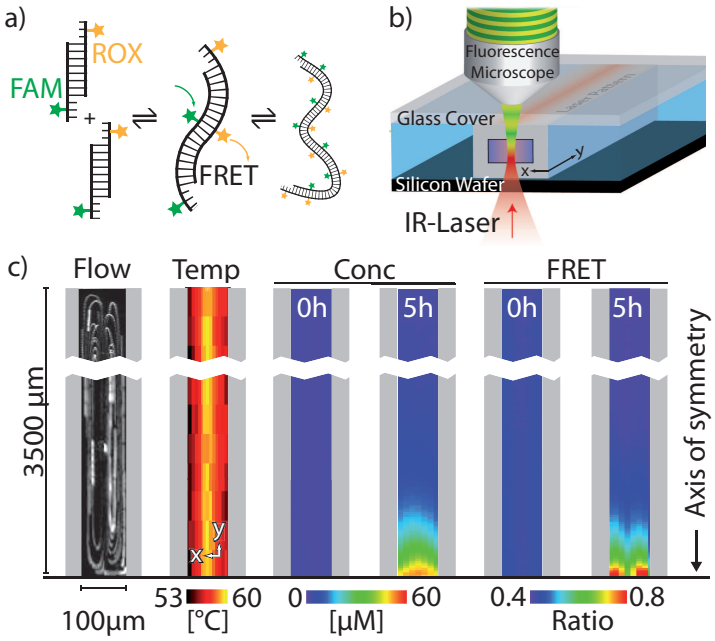

Figure 10: Experimental model system. (a) Double-stranded DNA with two sticky ends serves as a monomer for the reversible polymerization reaction. The sticky ends have a melting temperature of 55 °C and are labeled with a FRET dye pair (FAM as donor, ROX as acceptor). (b) The absorption of a symmetrically moved IR-laser spot in the center of a 50 µm x100 µm borosilicate capillary creates thermoviscous convection flow and thermal gradients. (c) The fluid flow has four symmetric convection rolls that model four hydrothermal pores, connected at their bottom and hot sides (see Fig. 12). The temperature profile (T=53-60 °C) is measured using temperature-sensitive fluorescence. The total monomer concentration c_0 is inferred from the acceptor fluorescence and the polymerization is recorded using FRET.

Not all aspects of the experimental model system of trapped polymerization can be sufficiently described by the theory: The laminar drift flow in the order of 1 µm/s along the y-axis of the capillary breaks symmetry meaning that the four traps shown in Fig. 12 a are not identical anymore. Additionally, the dissociation constant of the polymerization reaction K_D was assumed to be temperature independent in the theoretical treatments. This is sufficient to show that the positive feedback effect exists for e.g. trapped RNA-polymerization and does not change fundamental properties of the given theory. However, in order to precisely describe the experiment with a theoretical model, the assumption of $K_D(T) = const.$ has to be abandoned. As the analytical possibilities to solve this more complex problem are limited, a finite element simulation (Femlab, Comsol) has been developed that describes the full hydrodynamic system (drift flow, convection flow) as well as the drift diffusion problem (Eq 6). The polymerization theory under the assumption of separated timescales was incorporated by considering effective diffusion and Soret coefficients $\bar{D}$ and $\bar{S}_T$ using the scaling laws defined in [33] and a previously done measurement of $D(1)$ and $S_T(T)$ via microscale thermophoresis [33, 37, 46–48]. Furthermore, the separately measured

temperature $T(x,y)$ and the flow profile $v(x,y)$ (Fig. 12 b) as well as the temperature dependent dissociation constant $K_D(T)$ (Fig. 9 and Fig. 12 c) were used as boundary conditions of the simulation. The experimental workflow (laser on-times) was then reproduced within the finite element system while the total local monomer concentration c_0 was measured measured in the experiment or taken at one identical position in the simulation (see Fig. 14).

In order to show that the simulated system and the derived theory of trapped polymerization match, the simulation was simplified according to the theoretical approximations ($K_D(T) = const.$ within the pore, no drift, non-slip boundary). The resulting data was compared to the theoretical predictions of the relative total monomer concentration c_0^{trap}/c_0^{top} at the pore bottom for different dissociation constants K_D. A rather small pore with a height $h = 5\,\mathrm{mm}$ and an examplary temperature difference of $\Delta T = 30\,\mathrm{K}$ was chosen and simulated across a K_D-range. Larger geometries lead to memory problems in the range of small dissociation constants. As shown in Fig. 11 theory and simulation match reasonably well within one order of magnitude and reveales the increase in trapping efficiency due to the formation of longer polymers as soon as c_0^{trap} exceededs K_D.

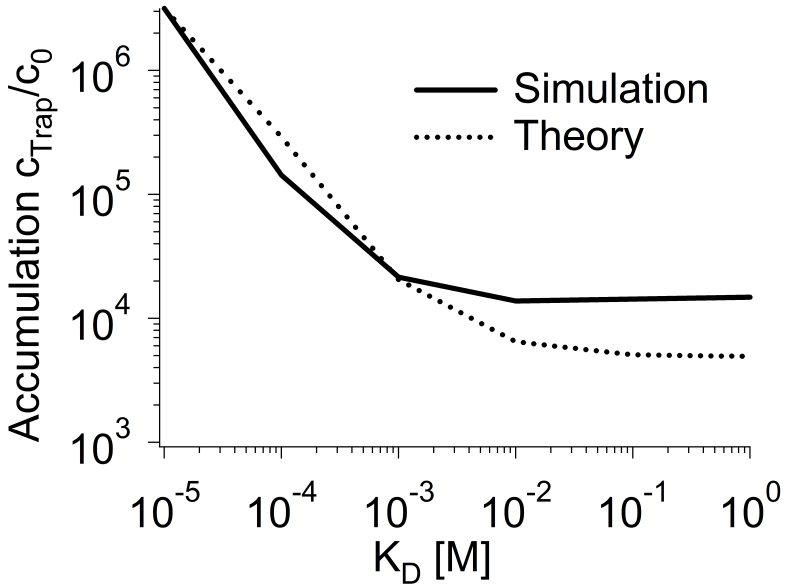

Figure 11: Enhancement of accumulation by polymerization in theory and simulation. The fast polymerization of RNA (D and S_T see Fig. 3) inside a slow trap with $5 \cdot 10^{-3}\,\mathrm{m}$ height, a width of 62.5 µm and a temperature difference of $\Delta T = 30\,\mathrm{K}$ across a broad range of dissociation constants K_D. The initial monomer concentration was $c_0 = 1\,\mu\mathrm{M}$. The transition in the accumulation efficiency by trapping of long polymers is clearly visible in simulation and theory. Simulation and theory match within less than one order of magnitude.

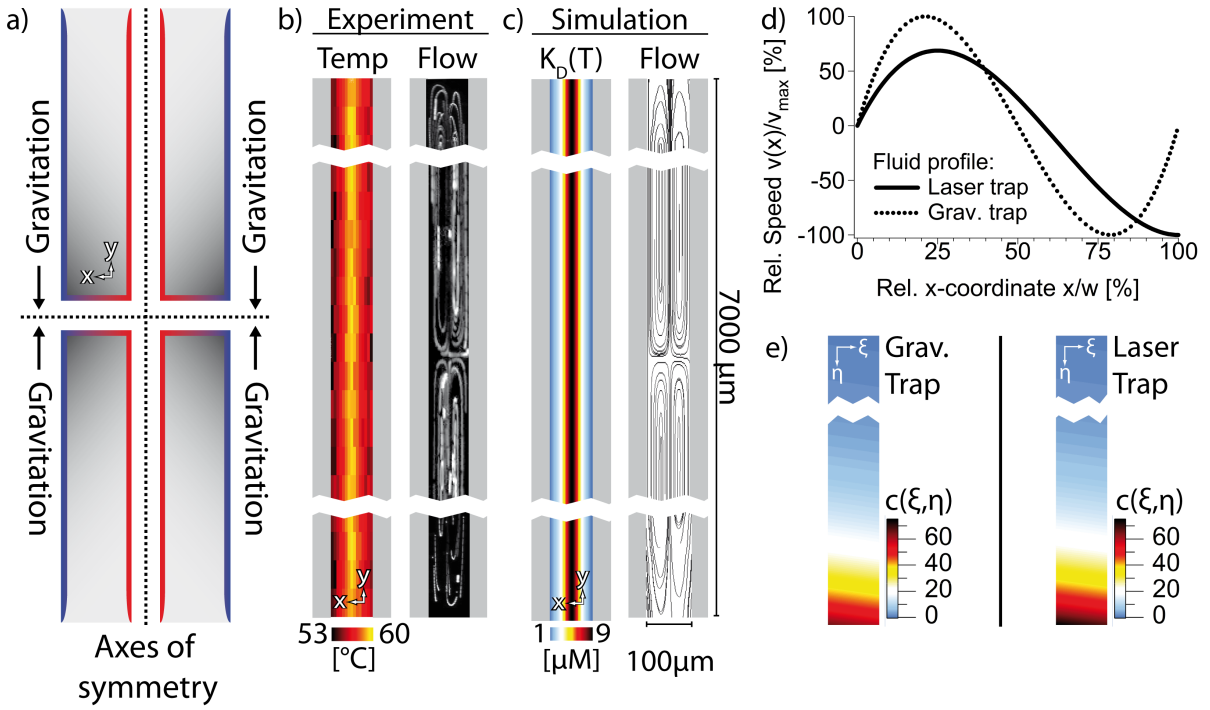

Figure 12: Connection of experimental and theoretical model and simulation. (a) A gravitational trap is driven by a thermal gradient and the buoyancy of water. It has a fixed relation of the diffusion coefficient D of the species to be accumulated and the optimal width w_{opt} of the trap. In a laser-driven trap, the convection speed can be set independently of the temperature gradient, which allows to optimize the convection speed for any biomolecule species at a fixed trap width [27]. The geometry of the laser-driven trap can be thought of as four gravitational traps glued together at their hot and bottom sides with symmetric boundary conditions. (b) The 2D-temperature profile was measured using the temperature dependent dye 2',7'-Bis-(2-Carboxyethyl)-5-(and-6)-Carboxyfluorescein (BCECF) and the temperature dependent fluorescence of the FRET-signal following a melting curve calibration. The fluid flow was measured tracking fluorescent beads. (c) A 2D-finite-element simulation of the experiment. We used the theoretical concentration-dependent diffusion coefficient $D(c)$ and Soret coefficient $S_T(c)$ to take into account the timescale-separated polymerization reaction. The temperature-dependent dissociation constant $K_D(T)$ was measured separately (see Fig. 9) and mapped to the temperature profile inside the trap. Therefore, all relevant experimental parameters ($K_D(T)$, temperature, convection flow, degree of polymerization and monomer concentration) were modeled successfully (see Fig. 14). (d) Convective flow $v(x)$ according to Eq. 8 and Eq. 24. The difference stems from the missing non-slip boundary conditions at the hot side $\xi = 1$ of the convection flow; however, it has no significant effect on the trapping efficiency. (e) Concentration distribution $c(\xi, \eta)$ according to Eq. 10 and Eq. 25 for ribonucleotides with $S_T = 0.01 \cdot 1/\mathrm{K}$, $\nabla T = 10\,\mathrm{K}$, $p = S_T \cdot \nabla T = 0.1$, $q_{grav,opt} = 100$ for the gravitation trap, $q_{laser,opt} = 5.8$ for the laser trap, and an exemplary trap aspect ration of 1:100.

4.2 Results: Trapped Polymerization

The monomers with the ability to polymerize were created by annealing the DNA-oligomers DNA_A and DNA_B (Tab. 1) with a concentration of 100 µM in PBS (137 mM NaCl, 2.7 mM KCl, 10 mM $Na_2^+HPO_4^{2-}$, 2 mM KH_2PO_4) at pH 7.5 from 95 °C to 10 °C with a cooling rate of 1 K/10 s. The resulting monomers (H3) were diluted to 10 µM solutions. For the trapped polymerization experiments, an initial concentration $c_0(t=0) = 2\,\mu M$ in PBS was injected into the borosilicate capillary. The syringe pump at one end of the capillary applied a constant laminar net flow along the capillary with a flow speed of $v_{max} = 1\,\mu m/s$. The outflow at the other capillary end was collected in a water filled microcentrifuge tube to minimize surface tension effects. The IR-laser was switched on while the scanner mirrors were running through a symmetric non-flow pattern for initial temperature equilibration and measurement as explained in the previous chapter. After 10 frames ~ 2 minutes, the scanning mirrors were changed to describe an asymmetric pattern that created four symmetric convection rolls by thermoviscous pumping with a mean fluid speed of $v = 28\,\mu m/s$. All fluorescence data was noise corrected to a water filled capillary at the same illumination settings as a blank measurement. The local total monomer concentration $c_0(t) = \sum kc(t)$ in the trap-center and at the -edge was measured by comparing the fluorescence channel $AA(t,x,y)$ at frame t with the initial, temperature equilibrated value $AA(10,x,y)$ at frame 10. The fluorescence channels *DA* and *DD* were simultaneously recorded and, taking into account the previously done FRET-calibration (Fig. 9), the FRET-ratio was calculated via Eq. 22. The time course of $\sum kc_{Edge}(t)$ and $\sum kc_{Center}(t)$ is plotted in Fig. 14 a. The different time points are indicated by letter A-D. After six hours (time point C in Fig. 13 and 14) the concentration ratio of the trap center and edge reached a fixed value: The monomer concentration was increased in the trap center and reduced at the edges (separation phase). The experimental data (solid line in Fig. 14 a) is in good agreement with the simulation (dashed line in 14 a). Larger timescales (137 days) not accessible in the experiment were extrapolated from the simulation. After time point C the concentration gradient at the edge lead to a diffusive inflow of monomers, supported by the flow produced by the syringe pumps, until the final steady state was reached at time point D (filling phase). At this time point, the edge concentration $\sum kc_{Edge}(t)$ of the trap had equilibrated with the total monomer concentration present in the outer bulk reservoir. Monomers had been accumulated to a more than 1000 fold increased concentration inside the trap. The total local monomer concentration is plotted against the FRET-ratio in Fig. 14 b. The theory (dashed line), the trapped polymerization experiment (solid line) and a previously done titration experiment with a physical equilibrium (open squares) are in good agreement. This shows that the polymerization theory for a diffusion controlled system as well as the assumption of separated timescales is valid for the experiment. The theory is therefore used to describe the time dependent length distributions based on the measured mean length $\langle n \rangle_{Center}$ and total monomer concentration $\sum kc_{Center}(t)$ (Fig. 14 c, d): At time point C, due to trapped polymerization more monomers are incorporated in 11mers than being left unbound. After final equilibration (time point D), the simulation even suggested a mean polymer length of 24 monomers which corresponds to a absolute length of 2880 base pairs. The good agreement of experiment and simulation, backed up by the agreement of simulation and theory shown in Fig. 11 give a solid

fundament for the extrapolation of the theory of trapped polymerization to the prebiotic RNA-world scenario described in chapter 3.2.

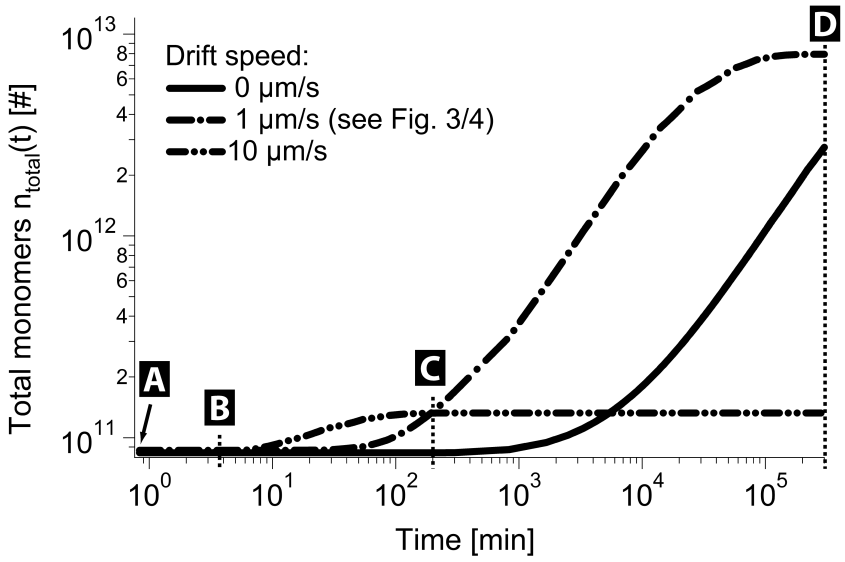

Figure 13: Separation and filling phase in the "total mass" view. The total amount of monomers integrated over the complete simulated area of thermal trapping $n_{total}(t) = \sum_k k \cdot \int_{V(Trap)} c_k \cdot dV$ for different net drift flows through the capillary. In Fig 14, a drift speed of 1 µm/s was used: After six hours, the edge area was depleted by two orders of magnitude and therefore the steady state of the separation ratio $\sum k \cdot c_{k,center} / \sum k \cdot c_{k,edge}$ ($t = 1 \ldots 10^2$min, time points A-C) was reached. Subsequently, at the edges of the trapping area a strong concentration gradient was built up pointing outwards and leading to a diffusive influx of new monomers according to $j_{Drift} = -\nabla c \cdot D_{monomer}$ ($t = 10^2 \ldots 10^5$min, time points C and D), until the edge and bulk concentration of monomers matched ($t > 10^5$min). Higher drift speeds (10 µm/s) lead to a significantly faster equilibration time of the trapped polymerization at the cost of a lower total monomer accumulation. Without drift (0 µm/s), equilibration would take several years.

The influence of an external net flow through the capillary on the separation and filling phase is illustrated in Fig. 13: The total monomer concentration is integrated over the complete simulated trapping area and plotted against time for different external net flow speeds. In all cases, the total monomer content in the trapping region is constant for a certain amount of time (separation phase). In this period, the monomers that have been present inside the trapping region from the start are collected in the center and depleted at the edge. The resulting concentration gradient leads to a diffusive inflow of new monomers into the trapping region. The external net flow also pushes trapped material towards the syringe-opposing end of the capillary, leading to a shorter trap relaxation time at the cost of a lower trapping efficiency.

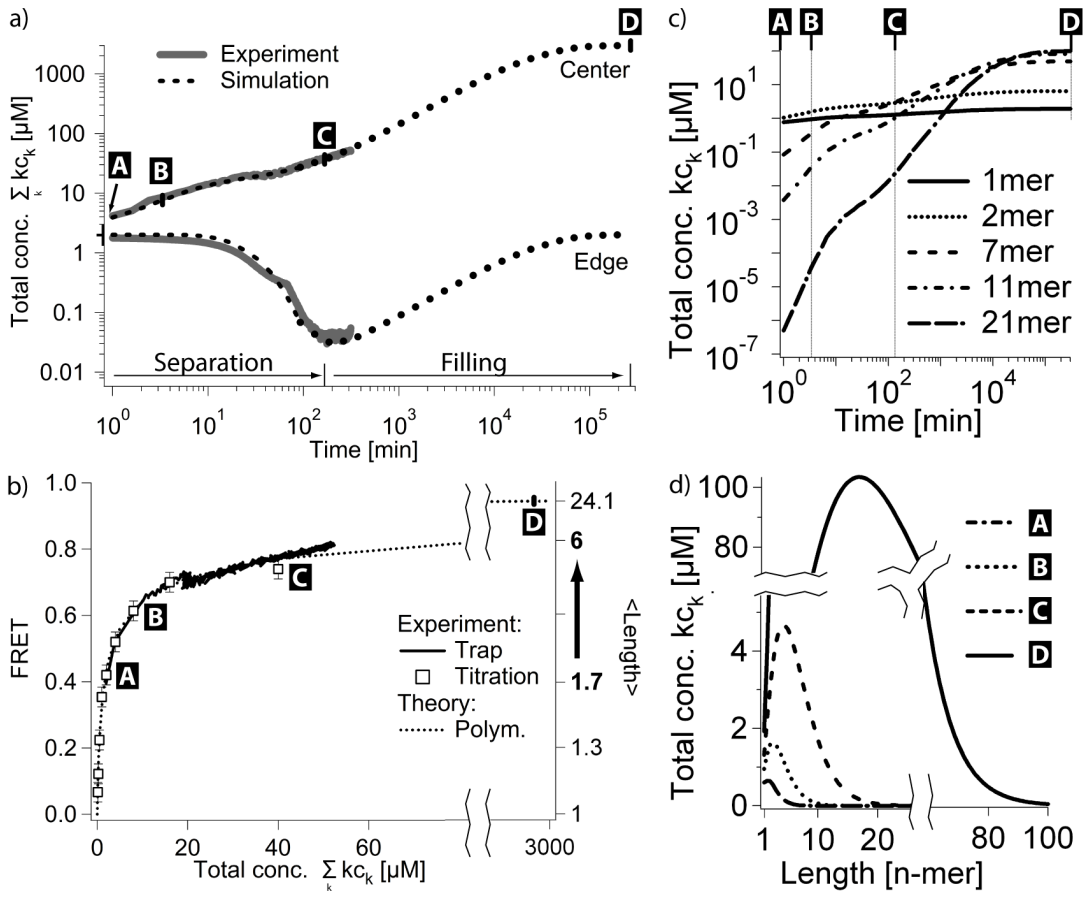

Figure 14: Results of polymerization theory, finite element simulation and experiment. (a) Simulated and measured monomer concentration in the center and at the edge of the trap. A net flow of 1 µm/s was applied from the outside using a syringe pump to reduce the relaxation time of the trap (from years to one month, see Fig. 13) at the cost of trapping efficiency. The initial monomer concentration was 2 µM (time point A). The separation ratio $\sum kc_{k,center} / \sum kc_{k,edge}$ was increased (separation phase) until the steady state was reached after 6 h (time point C). The monomer concentration at the trap edges has been depleted by two orders of magnitude. By drift and diffusion from the surrounding bulk reservoir, the trap was filled until the concentration at the trap edges reached the one of the reservoir (filling phase). Due to the restricted one-dimensional geometry outside the trap, filling is inefficient and required several weeks even in presence of the applied net flow (time point D). (b) The FRET-signal is a direct measure for the monomer concentration in the trap center. During the complete experiment, the relationship between concentration and mean length matched the polymer theory without fitting parameters when taking into account the previously measured dissociation constant K_D (see Fig. 9). The same relationship was obtained by titration in bulk solution (open squares). This validates the approximation of separating the polymerization and trapping time scales made in the theory. (c, d) The time evolution for the total monomer concentration of a selection of various polymer lengths was obtained using the experimental FRET- and concentration values as parameters for the polymerization theory. The same set of data was used to show the complete length distributions for time-points A-D. The mean polymer length increased from 1.7 (equivalent to ~200 bp, time point A) to 24 monomers (equivalent to ~2,880 bp, time point D).

The theory of trapped polymerization derived in part I is based on realistic assumptions and uses experimentally measured parameters. The chemical system of polymerization and the physical system of the thermal trap are combined and show a mutual enhancement in case of fast polymerization ($\tau_p \ll \tau_a$). As the thermophoretic parameters of RNA for different lengths at various salt concentrations are available, the polymerization of RNA in thermal traps can be predicted. All results are presented for a broad range of the dominant parameter of polymerization, K_D, and are therefore applicable to various RNA-polymerization models [15–18]. Interestingly, the mechanism of trapped polymerization is enhanced in solvents with low salt concentrations. These boundary conditions also favor the polymerization of RNA [16, 17] and the formation of proto-cell like fatty acid vesicles [49]. Compared to modern phospholipid membranes, the fatty acid membranes used in these vesicles have a higher permeability for ions, sugars and nucleotides. This is essential since membrane transport proteins were not initially present in the primordial scenario. The results therefore represent a missing step in the molecular evolution of life and describe how complex and long polymers are created with the help of a simple physical non-equilibrium system at already proposed and plausible boundary conditions.

4.3 Results: DNA-Gels

The aggregation and self assembly of polynucleotides exhibits interesting possibilities and insights into some of the most important processes of living organisms. Examples are the condensation of DNA and proteins in chromatin where the DNA is reduced by a factor of 50,000 in length, yet still accessible for regulatory proteins [50]. Chromatin structures also play an import role as biological micro-lenses in mammalian photoreceptor cells [51]. It was shown that high concentrations (100-200 mg/ml) of rod like DNA-polymers in aqueous solvents are able to form liquid crystalline structures without the help of enzymes at various salt concentrations [52, 53]. At lower concentrations of 5-20 mg/ml, sonicated calf-thymus DNA with a length of ~200 base pairs gelated with the help of Na^+ and Mg^{2+} ions [54]. Defined and complex structures completely made from DNA can be formed using DNA-origami techniques. Therefor, a long viral ssDNA (scaffold) is connected by short synthesized DNA-oligomers (staples) via hydrogen bridge bonds stabilized with a slow thermal annealing process [55]. The DNA origami technique has been used used to create plasmonic nanostructures [56], molecular drug carriers for cell-uptake [57] or metallized nanostructures [58]. The question arises if similarly complex and specific structures made out of polynucleotides can also be formed in the system of trapped polymerization.

In the last chapter, the continuing physical non-equilibrium of a thermal molecule trap was shown to enhance reversible polymerization. The presented results revealed the degree of polymerization and the total monomer concentration at the trapping center as well as at the edge of the trap. However, in the analysis of the complete trapping region described in the following, highly fluorescent aggregates were found on the cold bottom side of the capillary (Fig. 15 a). The pattern of molecular aggregates reproduces the laser pattern, similar to the accumulation of DNA in a convection chamber shown in [24]. This suggests that a second, upward directed convection is created by the light pressure of the IR-laser and the buoyancy of the heated liquid. Both effects yield a mean convection speed of $\bar{v}_z = 3.8\,\mu$m/s along

the z-axis, measured by tracking fluorescent beads in the laser heated capillary without thermoviscous flow. When the thermoviscous flow along the y-axis is switched on ($\bar{v}_y = 28\,\mu$m/s), the superposition of both orthogonal flows and thermophoresis yields a spiral molecule-flow pattern that crosses the thermal gradient multiple times in the complete reaction volume and not only in the trapping center (Fig. 15 b). Since this complex three dimensional system is not analytically accessible and the according finite element simulation showed to be incompatible with the incorporation of phase transitions so far, a purely experimental approach is used to determine the properties of the molecular aggregates formed in the thermal trap. Interestingly, this combination of two traps is equivalent to a tilted gravitational trap that should be far more prevalent in the prebiotic environment than its non-tilted counterpart.

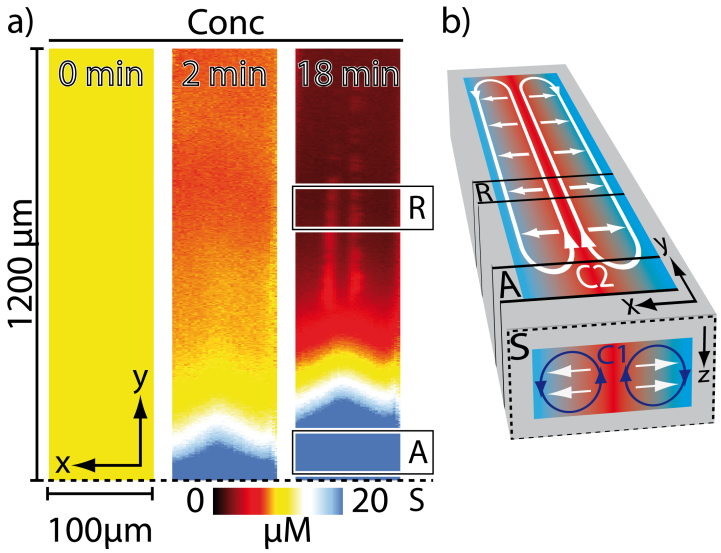

Figure 15: DNA aggregates and proposed dual trap mechanism: (a) After a trapped polymerization experiment with identical conditions to those used in chapter 4.2 but with a higher starting monomer concentration of 10 µM, small fluorescent DNA-aggregates could be found in the central accumulation region A of the symmetric trap. The concentration measurement is averaged over the z-axis of the capillary. The observation region R has a distance of 710 µm to the center A and is used in Fig. 16-18. The axis of symmetry S is analog to Fig. 10. (b) Proposed trapping mechanism. Since the light pressure of the IR-laser and buoyancy are directed upwards, an additional convection flow $C1$ is induced perpendicular to the thermoviscous flow $C2$. This is equivalent to the prebiotically far more abundant szenario of a tilted thermogravitational trap and leads to more complex trapping characteristics. Accumulation region A, observation region R and plane of symmetry S are analog to (a).

Formation

The formation of aggregates was recorded with the setup described in the previous chapter. A borosilicate capillary was filled with a 10 µM solution of monomer blocks (H3, Tab. 1) solved in physiological buffer (PBS). The IR-laser pattern was shifted along the x-axis to be slightly off-center which improves aggregation (Fig. 17 c). Time traces of the total monomer concentration (Fig. 17 a) and the FRET-ratio (Fig. 17 b) for the off-center area R at which aggregates were (point A) and were not found (points B and

B') after one hour are shown in Fig. .17. Since the observation region R was not placed directly in the accumulation center (Fig. 15), the total local monomer concentration was depleted by the thermal trap. At $t = 60\,\mathrm{min}$, the IR-laser spot movement was changed to be symmetric which resulted in a vanishing thermoviscous flow at an unchanged temperature profile. In the absence of trapping, the accumulated polymers diffused out of the trapping center. This lead to a short increase of the total local monomer concentration $c_{total} = \sum k c_k$ at all points A, B and B'. Subsequently, outward directed thermodiffusion at the borders of the heated capillary region lead to a complete depletion of c_{total}. Aggregates and an increased steady state depletion plateau of c_{total} were found at position A during the thermal trapping (solid black line) compared to points B and B'. The concentration traces for c_{total} at points B, B' and A diverged at $t = 13\,\mathrm{min}$ in combination with the visible occurrence of aggregates (Fig. 17 d-e). The same behavior was observed for the FRET-ratio at points A, B and B' (Fig. 17 b). At the gelation site A, the local mean length exceeded 200 monomers according to the polymerization theory derived in [19]. After switching off the trap at $t = 60\,\mathrm{min}$, the relatively large aggregation region shown in Fig. 17 f reduced to some stable fluorescence spots shown in Fig. 16. This aggregation could not be found when cycling equal monomer solutions with a standard thermocycler between the same temperatures. Accordingly, the accumulation of material seems to be the driving force of the DNA aggregate formation.

Specificity

To characterize the nature of the aggregates, melting curves were measured at the end of the experiments shown in Fig. 17. As most of the solved polymers were depleted by outwards directed thermodiffusion, the remaining aggregates could be investigated with a low background signal. The fluorescence channel $DA\,(T)$ (Tab. 2) at a temperature T was normalized to the channel $DA\,(65\,^{\circ}\mathrm{C})$ and is shown in Fig. 16. The temperature profile of the thermal trap was still established by IR-laser absorption while the increase of the offset temperature was realized using thermoelectric elements. The signal was compared to a melting curve derived from the absorption of the same solution in bulk with a UV-VIS spectrometer. The aggregate at site D (Fig. 16 b, c) disappeared completely after the first melting transition at $T = T_{m,1}$ which is identical to the melting temperature of the polymer bond. Since the trapping experiment started with a temperature of 65 °C at the sites C-E, only the falling edge of this melting transition is visible. The second, less pronounced melting transition at $T = T_{m,2}$, shown in the inlet of Fig. 16 a, is comparable to the melting transition of the aggregates at point C and E. It corresponds to the melting of the monomer (H3) into its constituent oligomers DNA_A and DNA_B. Accordingly, the aggregates consist of labeled monomer H3 and seem to form at least two different types of DNA gel-like structures: A weaker type (site D, C and E in Fig. 16, site A in Fig. 17) that is dominated by the sticky end polymer bond and a stronger type that is only dissolved if the dsDNA monomer block itself is going to melt (site C and E in Fig. 16).

To further prove that the DNA-aggregation specifically depends on the polymer bond, the polymerizing monomer H3 was exchanged for the monomers H1 and H2 in which one sticky end is randomized to prevent polymerization (Fig. 18). The same trapped polymerization was repeated multiple times. The

time until the appearance of DNA aggregates τ_{gel} was measured by calculating the overall contrast inside the same off-center capillary region R observed in Fig. 15 and Fig. 17. Aggregation was only found for H3 whereas even several hours of trapping of H1 and H2 did not lead to visible structures.

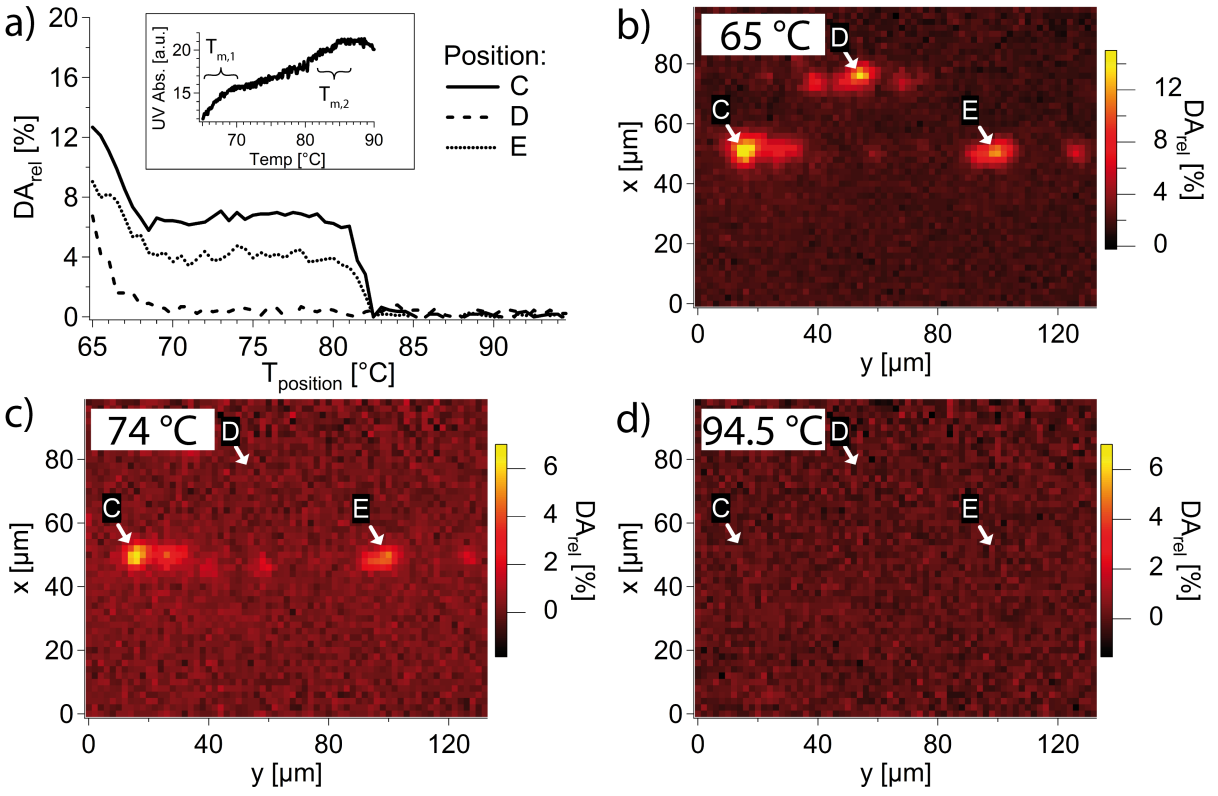

Figure 16: Different melting temperatures of DNA-aggregates. After the formation of the DNA-gel and subsequent removal of remaining free polymers and weakly bound aggregates by outwards diffusion (trap switched off, temperature unchanged, see Fig. 17) the melting temperatures of the remaining aggregates were measured. Since the local concentration is too low to measure a concentration corrected FRET-signal (Eq. 22), the DA channel relative to the first frame of the measurement was used to visualize the melting transitions without further corrections. (a, b) The local temperature for three points C-E (see Fig. 17 c) was increased in 0.5 K steps using thermoelectric elements. Since the starting temperature is already 10 K higher than the regular melting temperature $T_{m,1} = 55\,°C$ of the polymer bond, only the falling edge of the melting transition is visible ($T = 65 \ldots 68\,°C$). (inlet) Melting curves measured via fluorescence and UV-absorption are comparable, which connects the fluorescence data to the actual melting of the polymer bond and the hybridized monomer. (c) Surprisingly, not all DNA-aggregates disappeared after the first melting transition (points D, E). (d) After a second melting transition at $T_{m,2} = 82\,°C$ all aggregates dissolved. $T_{m,2}$ corresponds to the melting temperature of the monomer (see (a): inlet).

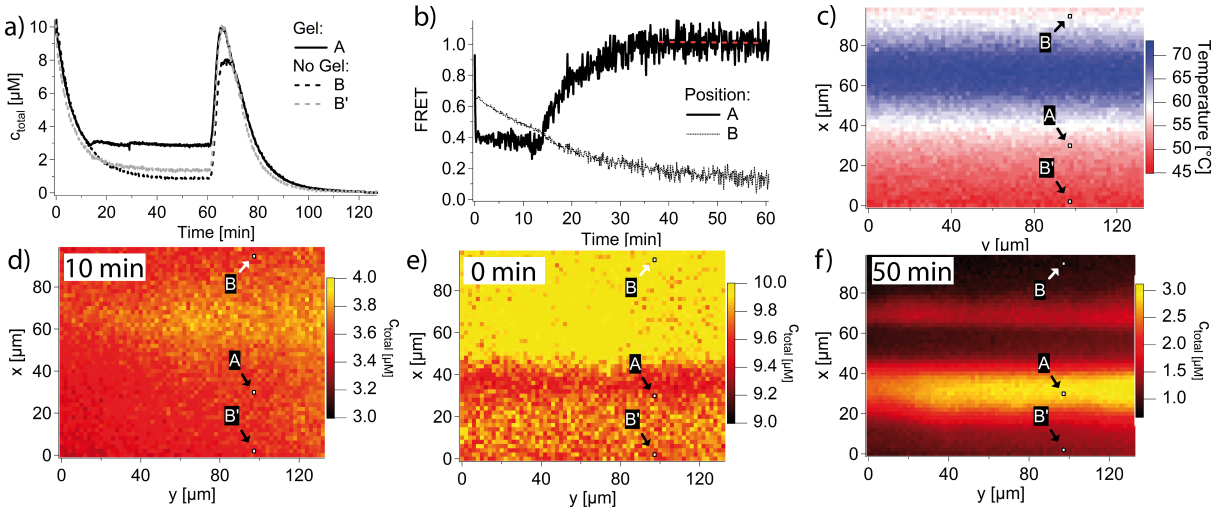

Figure 17: Aggregation of DNA in a thermal trap. (a) The symmetric laser-driven thermal trap shown in Fig. 12 was used to create off-center DNA-aggregates in the observation area R shown in Fig. 15. x- and y-axis are equivalent to previous figures. The camera was focused to the lower wall of the borosilicate glass capillary, where the DNA-gel settled. The laser pattern shown in (c) was slightly shifted along the x-axis to enhance the total amount of aggregates. To record the dynamic formation of the DNA-aggregates and for melting analysis, the area of observation was moved off-center inside the trap along the y-axis by 710 µm. At point A the formation of a gel-like structure was observed, while at point B at the edge of the capillary no gel was found during the whole experiment. The laser that created the fluid flow and temperature gradient was switched on at $t = 0\,\text{min}$. Since the trap accumulates all material with a positive S_T in the center, a depletion of the total monomer concentration can be observed at the off-center position. The first gel appears at point A after 13 min of active trapping, clearly visible by the deviation of $c_{total}(t) = \sum_k k c_k$ between point A and B. After one hour, the trap was switched off by making the laser pattern symmetric which stopped the thermoviscous pumping but left the temperature profile unchanged. Accordingly, the previously trapped DNA-polymers diffused out of the center region into the observation region, which leads to a strong transient peak in $c_{total}(t) = \sum_k k c_k$ and a subsequent diffusive depletion towards the edges of the trap. (b) Degree of polymerization at point A and B inside the observation region measured via FRET. At point B, the FRET-ratio follows the total local concentration of monomers according to the polymerization theory. The formation of DNA-aggregates is clearly visible at point A as a sudden increase of the FRET-value at $t = 13\,\text{min}$ which approaches $FRET = 1$ until the trap is switched off after 1 h. Since the determination of the mean length obtained via $\langle n \rangle = 1/(1 - FRET)$ is diverging when $FRET \to 1$, exact values cannot be given but just lower limits. A linear fit (red, dotted line) reveals a lower limit of $FRET \geq 0.995$ which corresponds to a mean length of $\langle n \rangle \geq 200$. (c) 2D-map of the temperature in the observation region measured with the temperature dependent dye BCECF. The laser power was slightly increased compared to the previous polymerization experiments to enhance the temperature gradient and therefore the efficiency of trapping and the DNA-aggregation. (d,e) The total concentration of monomers $c_{total}(t)$ for different trapping times. Before gel creation ($t = 0 \ldots 13\,\text{min}$), the monomer distribution in the off-center observation area is almost homogeneous. (f) After 50 min, the DNA aggregates are clearly visible.

Kinetic Model

A simple kinetic model to describe the aggregation is now derived after measuring the gelation times t_{gel} for different initial total monomer concentrations c_0. As a simple nucleation model, we assume the de novo formation of gel-like aggregates by distinguishing between monomers incorporated into an aggregate (state G with concentration $c_g(t)$) and those which are not (state N with concentration $c_{ng}(t)$). Since t_{gel} is the time to build up a new gel, the growth of an already existing aggregate $G+N \rightleftharpoons 2G$ is neglected. The nucleation model is therefore characterized by $N+N \rightleftharpoons G$ and the resulting rate equation reads:

$$\frac{dc_{ng}(t)}{dt} = -2 \cdot c_{ng}\left(c_{ng} \cdot k^{on} + k^{off}\right) + 2 \cdot c_0 k^{off} \tag{26}$$

The solution to this equation reads

$$c_{ng} \propto \tanh\left(t \cdot \sqrt{4 \cdot c_0 \cdot k^{off} \cdot k^{on} + k^{off} \cdot k^{off}} + const.\right) \tag{27}$$

and leads to a characteristic timescale [59]:

$$\tau_{gel}(c_0) \quad = \quad 1/\sqrt{k^{off}\left(4 \cdot c_0 \cdot k^{on} + k^{off}\right)} \tag{28}$$

which is fitted against the initial total monomer concentration shown in Fig. 18 b with the inclusion of a trap dependent offset value. The mean error of $\Delta t \sim 400\,\mathrm{s}$ for the experimental gelation time was obtained from H3 accumulation experiments shown in Fig. 18 a. Despite this extremely simplified model, the dissociation constant $K_D \equiv k^{off}/k^{on}$ fitted to 1 µM which matches the K_D of the polymer bond. In combination with the experiments shown in Fig. 16 and 18 we therefore conclude that the gel-like aggregation of DNA in a thermal trap is a highly bond specific process: Without complementary sticky ends, aggregates are not found even for long accumulation times. With complementary sticky ends, aggregates formed within 13 minutes that are specific to the polymer bond itself (points C, D and E in Fig. 16) as well as specific to the bond of the monomer constituents (points C and E in Fig. 16). Since the gelation of non-specific DNA under similar salt conditions and even lower temperatures is already possible at DNA concentrations of $> 16.2\,\mathrm{mg/ml} \sim 200\,\mu\mathrm{M}$, the additional convection flow C1 shown in Fig. 15 b and the polymerization are able to accumulate and stabilize the DNA by a factor $\gg 20\times$ at an off-center position [54]. This is not expected from a trap driven by the thermoviscous flow C2 alone.

The selective aggregation of genetic material could have played an important role in molecular evolution. The mechanical stabilization of specific polymer sequences inside porous structures means a protection of a highly concentrated phase against perturbations of the trap by pulsating flows due to e.g. hydrothermal activities. The DNA-aggregates found in the experimental thermal trap are stable against high speed flows up to 1 ml/min through the capillary at room temperature. These advantages could have favored the formation of specific, complementary sequences in the randomized sequence space of genetic information similar to the tRNA replicators presented in [29, 39].

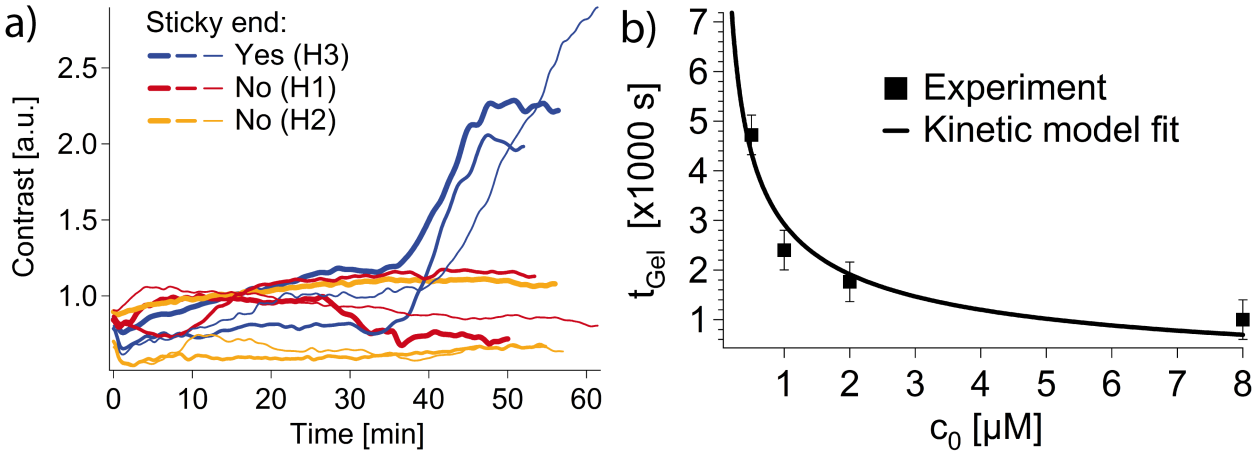

Figure 18: Specific gelation and kinetic model. (a) DNA-gelation is specific for the polymerization bond. A 1 µM solution of the polymerizing monomers (H3) as well as of modified monomers with one of the two sticky ends being incompatible (H1/H2) were treated in the thermal trap. The normalized RMS contrast of the concentration signal was taken over time as an optical measure of gelation. It revealed gelation times almost identical to the polymerizing monomer. The non-polymerizing monomers did not show gelation within the experimental time of 1 h. (b) Fit of gelation times t_{gel} for different total monomer concentrations c_0 according to Eq. 28. The resulting dissociation constant matches the dissociation constant of the polymer bond $K_D \sim 1\,\mu M$.

Part II

A Thermal Trap for DNA Replication

5 Motivation

As shown in the last chapter, the physical non-equilibrium of a simple thermal gradient is sufficient to build up complex, biologically relevant molecules such as RNA or DNA. Biomolecules must have reached a certain degree of complexity to be able to replicate structural or genetic information, the key requirement for molecular evolution. However, the de novo formation of molecular replicators from prebiotically plausible building blocks could not be achieved in the lab to this date. The available sequence space that would need to be sampled is just too large without further constraints and the corresponding experiments would take to long. Even if it is assumed that such a replicator could have formed, many problems persist. One issue is the protection of the replication product against dilution due to diffusive outflow into the bulk ocean. The use of lipid bilayers as walls of protective proto-cells was limited in this prebiotic era, as transmembrane proteins for the transport of nutrients were not available. Also the more plausible fatty acid membranes proposed by Szostak and co-workers require a critical aggregation concentration to form, so that the dilution problem persists in principle [26, 49]. A second problem is the driving force of the replication process itself: Since replication of genetic information in modern life is based on the ability of DNA or RNA to act as a template to which the replication product is bound via hydrogen bridge bonds, prebiotic replication is also assumed to use the same template based mechanism. However, helicase enzymes that could have separated the template and product strand for a new replication cycle were not present in the prebiotic days. The template strand is therefore poisoned with the product and the replicative system persists in its equilibrium, which means death. This issue is addressed in the second part of this work which focuses on the ability of thermal traps to not only protect the replication product from outward diffusion but also to allow for an exponential replication process via the inhibition of template poisoning.

6 Accumulation

As pointed out in part I, thermal trapping results from the superposition of a convective fluid flow and a perpendicular thermophoretic diffusion in an elongated chamber (Fig. 19 a), both caused by the same temperature gradient. Solved biomolecules follow the convective flow and are exposed to a continuing thermal cycling while their cycle times will be shortened by the thermophoretic movement. The thermal cycling represents an effective way to prevent template poisoning in replication processes: At the cold side, the replicator is able to attach to the template strand. The replication process is then governed by the specificity of the hydrogen bridge bonds between template and product which leads to a bound complex after a successful replication cycle. Following the convective flow, the complex enters the hot side of the chamber. Here, product and template melt into two separate strands that may act as further templates in the next replication cycle (Fig. 19 a). The thermal restart of this process is highly effective and leads to an exponential replication of the initial template information. This principle of a thermally cycled replication is known from the polymerase chain reaction (PCR) for which temperature-stable polymerase

proteins are used. Such PCR-processes ([28, 60–64]) as well as the exponential replication of information purely based on tRNA ([29]) were found to be compatible with thermal cycling by convection. As PCR is a well established standard procedure in research and the unspecific labeling of dsDNA-products with intercalating dyes like e.g. Sybr Green I (Invitrogen) is very convenient, PCR is the preferred proxy method to show the exponential replication of genetic material in a thermal trap without the loss of generality [27].

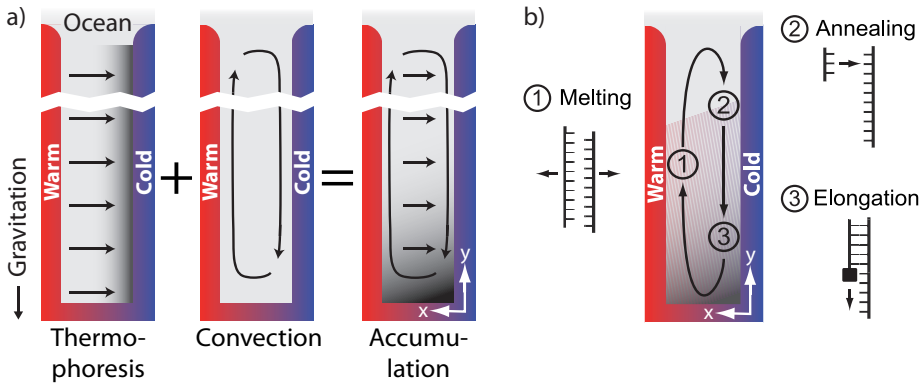

Figure 19: Thermal trapping and replication of genetic information. (a) Molecules shuffeled to the cold side by thermophoresis are transported downward by convection and accumulate at the bottom of the chamber. The replication product is trapped at the bottom of the capillary and therefore protected against diffusion into the highly diluted bulk solution. (b) Convection provides a temperature oscillation to periodically denature DNA with subsequent binding of short primers and replication by a polymerase protein. This experimental model of exponential replication acts as proxy for a temperature driven replication reaction that could rely solely on RNA [29]. The experimental setup is in principle identical to the one used in part I, yet slightly modified in order to reach higher temperature differences $\Delta T \geq 25\,\mathrm{K}$ for the polymerase chain reaction (PCR).

Since the experimental setup is similar to the one used in part I, only its modifications will be explained in the following (Fig. 10 b). As a reaction chamber, a borosilicate capillary with a rectangular cross section of 100 µm x 50 µm was embedded into immersion oil and sandwiched between an IR-transparent silicon wafer and a sapphire coverslip. The silicon wafers were tempered to 24 °C with thermoelectric elements. The convection speed inside the thermal trap was increased to a mean of $\bar{v} = 45\,\mu\mathrm{m/s}$, leading to fast trapping relaxtion times (experimental value: $\tau_a \sim 92\,\mathrm{s}$). An external drift flow through the capillary thus did not have to be applied. Both ends of the capillary were sealed with a reservoir of paraffin oil to prevent fluid drift. Imaging was done with the same fluorescence microscope as in part I using an air objective (20x, UPlanSApo NA = 0.75, Olympus), a CCD-camera (Luca SDL-658M, Andor) and a cyan high power LED (Luxeon V Star, Lumiled lighting). Temperature gradient and thermoviscous flow were established by the absorption of an IR-laser spot (1940 nm, 10 W, TLR-10-1940, IPG, Burbach) moving along the y-axis in the capillary center using a x-y- scanning mirror array. The IR-laser was focused with a single high aperture lens (C240TM, Tholabs) that allowed a scanning range of 1800 µm. The mean fluid speed $\bar{v}$ was measured using fluorescent beads with a diameter of

1 µm (F8888, Invitrogen, Fig. 20 a). To obtain the two dimensional temperature map $T(x,y)$ the relative fluorescence decrease of 50 µM BCECF in 10 mM TRIS was measured after 150 ms of laser heating (Fig. 20 c). The temperature dependence has been measured in a fluorometer before (Fluoromax-3, Horiba). The experimentally accessible parameters $T(x,y)$ and $\bar{v}$ were used as boundary conditions for a finite element simulation that describes the full hydrodynamic and diffusive system (see chapter 4). As a template, a synthetic 143mer ssDNA-strand with a random internal sequence was used. The primers were optimized to avoid intra- (e.g. hairpins) or intermolecular (e.g. primer dimers) structures by minimizing the according hybridization energies (Tab. 3). The PCR-solution was mixed to obtain various final template concentrations between 0 nM and 3.5 nM. The final concentrations were 500 nM of primers, 1x (~2 µM [65]) of SybrGreen I and 6 mg/ml of BSA. Nucleoside-triphophates (NTPs), buffer and TAQ-polymerase were taken from a ready-to-use master mix (FastPCR, Quiagen) at a final 1 x concentration. The product of trapped replication was compared to a reference of externally cycled (RapidCycler, Idaho Technology) PCR solutions with templates of different length (86 bp, 143 bp and 1530 bp). The PCR was done with 30 reaction cycles containing a denaturation step at 96 °C, an annealing step at 53 °C and an elongation step at 68 °C with each step lasting 30 s. Before each replication experiment, the the hot-start-polymerase enzyme was activated by heating the solution at 95°C for 5 minutes. The products of the reference solution were additionally compared to a ladder in a 1.5 % agarose gel (Fig. 22 a).

Compared to the previous part of this work, the laser driven thermal trap was adjusted to allow for a PCR by increasing the laser power and therefore the thermal gradient to $\Delta T \sim 27\,K$ with an edge (annealing and elongation) temperature of $T_{edge} \sim 59\,°C$ and a center (melting) temperature of $T_{center} \sim 86\,°C$ (Fig. 20 c). While thermal cyclers are optimized to reach the different temperature levels for melting, primer annealing and primer elongation with heating / cooling rates of up to 100 K/s throughout the complete solution [29], thermally driven convective cycling in a single compartment is less defined and allows the diffusive transfer of molecules between differently tempered convection paths. The width of the compartment therefore does not only define the accumulation efficiency but also the effective convection times, even for a geometrically decoupled, laser driven convection. Since the diffusion coefficient of the product was measured to be $D = 23\,\mu m^2/s$ (see chapter 7), an approximate cycle time of $t_{cycle} \sim w^2/D \sim 100\,s$ or faster is needed to ensure a stable thermal cycling. The higher convection speed of $\bar{v} = 45\,\mu m/s$ therefore does not only shorten the trap relaxation time, but also allows for short and stable replication cycles.

To experimentally validate the finite element simulation and illustrate the connection to the steady state theory derived in chapter 3.1.2, an externally cycled PCR-solution with a final concentration of 0.49 µM of the SybrGreen I labeled 143mer product was accumulated inside the laser driven thermal trap under the conditions described above (Fig. 20 e, f). The simulated and experimental accumulation time trace match and both run into a plateau of 1.7 µM after 300 s, corresponding to a characteristic time of the separation phase of $\tau_a \sim 92\,s$ (Fig. 20 g). As the gravitational trap was shown to be a valid approximation for the laser driven trap (Fig. 12), the accumulation length scale derived in the exponent

of Eq. 10 is:

$$\alpha' = \frac{w}{\alpha} = w \cdot \left(\frac{84pq}{10080 + q^2} \right)^{-1} \sim 6.3 \cdot 10^{-3}\mathrm{m} \tag{29}$$

with $q = v_0 \cdot w/D \sim 3246$, $v_0 = \frac{64}{3} \cdot v_{max}$, $p = \Delta T \cdot S_T = 27\,\mathrm{K} \cdot 0.01\frac{1}{\mathrm{K}} \sim 0.3$. S_T was measured via microscale thermophoresis (see next chapter). With a maximum convection speed of $v_{max} = 70\,\mu\mathrm{m/s}$, the estimation of the characteristic time of the separation phase $\tau_a \sim \alpha'/v_{max} = 90\,\mathrm{s}$ matches the experimental value. Eq. 10 can be transformed to:

$$\frac{c_{trap}}{c_{edge}} = \exp\left(\frac{504 \cdot vS_T \Delta T h D}{2835D^2 + 128v^2w^2} \right) \tag{30}$$

for the concentration ratio between the trap center c_{trap} and the trap edge c_{edge} with h being the trap height. Eq. 30 is plotted in Fig. 20 h which illustrates the dependence of the product concentration on the convection speed [27]. Obviously, the fast convective flow causes a large trade-off in the trap's steady state accumulation efficiency in favor of its replication relaxation time.

Name	Sequence
Product 143mer	5' - *CCCAGCTCTGAGCCTCAAGACGAT* - CCTGACCATTTCCATCATTCCAGTC GAACTCACACACAACACCAT ATGCATTTAAGTCGCTTGAAATT GCTATAAGCAGAGCATGTTGCGCCAG *TGGGTTGGACTTCTGCTTTTAAGCC* - 3'
Forward Primer	5' - CCCAGCTCTGAGCCTCAAGACGAT - 3'
Reverse Primer	5' - GGCTTAAAAGCAGAAGTCCAACCCA - 3'

Table 3: Primer and product sequences of the PCR: The synthetic 143mer template has a random internal sequence with a GC-content of 45 %. The primers also bind λ-DNA (Promega), which yields a product length of 1530 bp that is used to estimate the product length of trapped replication (Fig. 22). The primer sequences were chosen from the λ-DNA sequence and designed to have minimal hairpin ($\Delta G_{hairpin} \sim -1\frac{\mathrm{kJ}}{\mathrm{mol}}$) and dimerization energies ($\Delta G_{dimer} \sim -3\frac{\mathrm{kJ}}{\mathrm{mol}}$) using the tool Genamics Expression (Genamics, New Zealand).

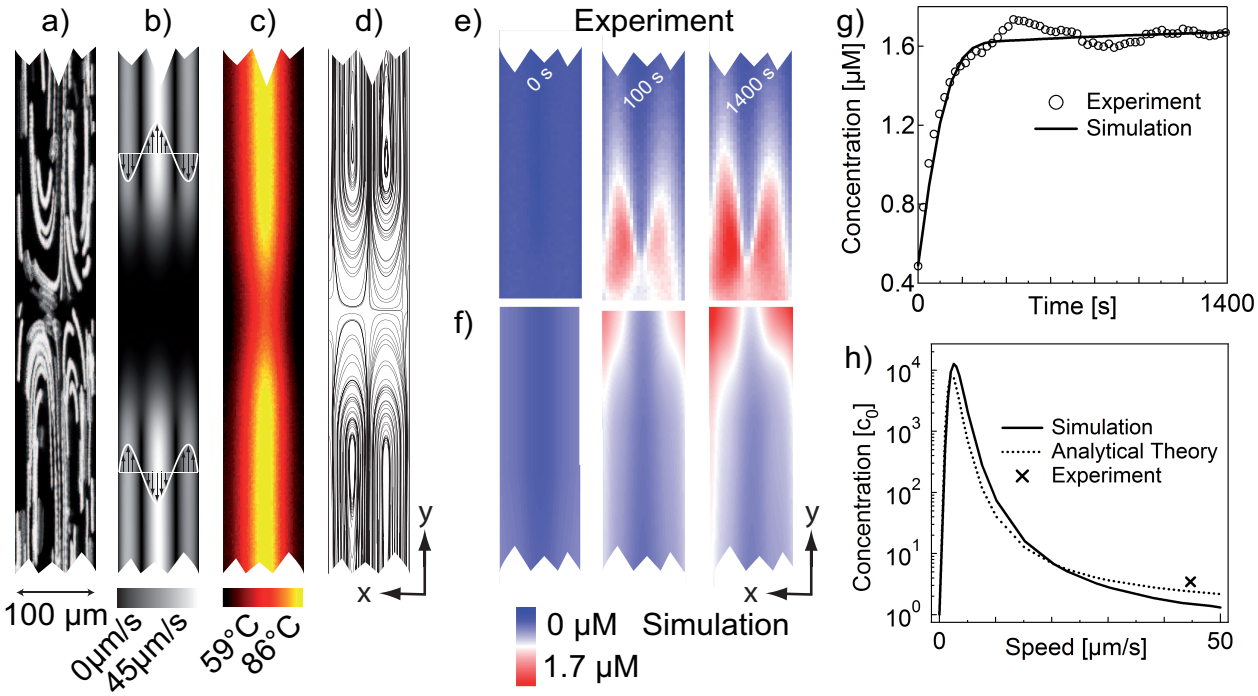

Figure 20: DNA accumulation in experiment, simulation and theory. (a) In the thermal trap's central region, the convection flow was tracked with 1 µm particles. The chamber averaged flow speed is 45 µm/s. (b) The flow profile used in the corresponding hydrodynamic finite element simulation was set to match (a). (c) The temperature profile was measured using a temperature dependent dye [33]. (d) Molecular trajectories from the superposition of fluid flow and thermophoresis. Brownian motion of single particles was not taken into account. (e) Fluorescence images visualize the DNA-accumulation over time. (f) The concentration timetrace is reasonably described with a finite element simulation. (h) The optimum convection speed for accumulation is approximately 2.5 µm/s. The experimental conditions favor faster PCR-replication at the cost of a reduced trapping efficiency. The given pore geometry and the high convection speed favor the accumulation of DNA monomers ($D_{opt} \sim 450\,\mu m^2/s$, Eq. 10).

7 Trapped Replication

A simple model to describe the growth of a population $c(t)$ is obtained using the kinetic equation $dc(t)/dt = kc(t)^p$ with k being a constant whereas p describes the type of growth. The case of hyperbolic growth ($p > 1$) has been described in the context of hyper-cycles [66, 67]. Here, multiple self-replicating units are interconnected in an auto-catalytic manner which leads to a complex behavior of their current concentrations over time. Systems that diverge in infinite time are called exponential ($p = 1$). The growth rate of a population then directly depends on its current size. This is the case for e.g. bacterial growth or PCR with small concentrations supported by a large amount of resources. In contrast, sub-exponential or parabolic growth ($0 < p < 1$) is self limiting and leads to finite populations. The previously mentioned template poisoning is an exemplary reason for replication reactions to be parabolic [68].

Like most realistic growth systems, PCR is not able to sustain unlimited growth of DNA in a closed system but runs into a plateau phase after the initial exponential replication phase. This is also expected to happen in a thermal trap that is filled with the 143mer-PCR-solution and connected to an outside reservoir via diffusion. The major contributions to this behavior are utilization of substrates like dNTPs or primers, thermal inactivation of the polymerase enzyme, polymerase inhibition by the PCR side product pyrophosphate, or annealing of DNA-product and template poising by high product concentrations [69]. Since all these contributions are caused by the limited size of the system, the kinetic growth equation for the exponential case ($p = 1$) can be expanded by a "resource" term $(Y - c(t))$ with Y being the initial total amount of resources or the absence of inhibitors:

$$\frac{dc_{PCR}}{dt}(t) = k \cdot c_{PCR}(t) \cdot (Y - c_{PCR}(t)) \tag{31}$$

The solution to this non-linear differential equation is found to be logistic:

$$c_{PCR}(t) = \frac{Y}{1 + \exp\left(-kYt\left(\frac{Y}{c(0)} - 1\right)\right)} \tag{32}$$

In terms of the concrete experimental values, this is renamed to:

$$c_{PCR} = \frac{c_{max}}{1 + \exp\left(ln(2)(t_{del} - t)/\tau_{doubling}\right)} \tag{33}$$

whereas t_{del} is introduced as an additional delay time for replication after the hot start procedure, c_{max} is denoted as final product concentration and $\tau_{doubling}$ as the doubling time of replication. The product is assumed to be replicated homogeneously in the complete compartment of the thermal trap due to the high convection speed and comparably low trapping efficiency. All product material created at a time $t - \tau$ is then trapped at the trap center with a time delay τ. The phenomenological time trace $c_{trap}(\tau)$ has previously been determined by fitting an exponential model to the accumulation of a 143mer without replication (Fig. 20 g). Accordingly, the concentration of the trapped replication product reads:

$$c_{TrappedPCR}(t) = \int_0^t c_{Trap}(\tau)\, \dot{c}_{PCR}(t - \tau)\, d\tau \tag{34}$$

Eq. 34 is numerically fitted against the experimental data shown in Fig. 21 a, c which revealed a doubling time of $\tau_{doubling} = 74\,\mathrm{s}$. However, the relative delay of replication $\Delta t_{del} = t_{A,del} - t_{B,del}$ for different initial template concentrations $c_A(0), c_B(0)$ is assumed to be more reliable in order to get $\tau_{doubling}$ [70]. Accordingly, the experiment was repeated for $c_A(0) = 3500\,\mathrm{pM}$ and $c_B(0) = 20\,\mathrm{pM}$, yielding $\Delta t_{del} = 388\,\mathrm{s}$. The doubling time is then inferred to be $\tau_{doubling} = ln(2) \cdot \Delta t_{del}/ln(c_A(0)/c_B(0)) = 50\,\mathrm{s}$. The small value of $\tau_{doubling}$ compared to the cycling time $\tau_{cycle} = 80\,\mathrm{s}$ indicates a minor shortening of the DNA trajectories by thermophoretic and ordinary diffusion. The negative control without template did not show replication (Fig. 21 b).

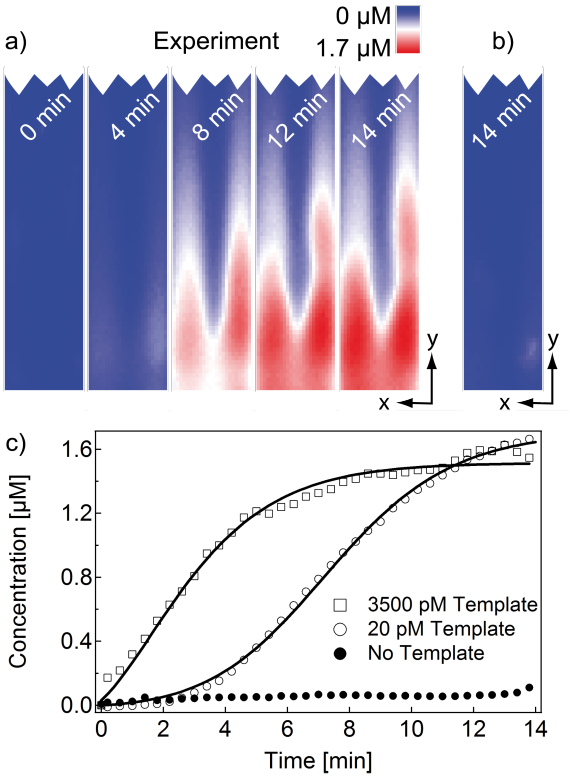

Figure 21: Quantitative, exponential DNA replication in a thermal trap. (a) Accumulation of the PCR-product by convection and thermophoresis, visualized by SYBR Green I fluorescence. (b) The negative control did not show a fluorescence increase. (c) The time trace of the central concentration fits with Eq. 34. Delays of replication due to different initial template concentrations allow to infer the replication doubling time with $\tau_{doubling} = 50\,\mathrm{s}$.

PCR in small volumes is often prone to the formation of primer dimers, especially for long template DNAs due to surface effects (e.g. sticking). Also denaturation of the polymerase at the surface is a common problem. Both effects are minimized by surface passivation with BSA (6 mg/ml). However, it has to be tested whether the product is not a short primer dimer but the expected 143mer. Despite the fact that SybrGreen I shows a higher fluorescence intensity in A-T bonds compared to G-C bonds, it is not sequence specific which would allow to discriminate between the unwanted (primer dimers) and the wanted (template) products [71]. The available sequence specific probing techniques like Molecular Beacons® or TAQ-Man® are costly and have to be redesigned for every single template sequence [72, 73]. In our case, the size determination of the products is a proper way to distinguish between short primer dimers (~50 bp) and long template based products. Gel-based methods cannot be used due to the low product volumes (~pl) of the reacted sample inside the capillary. Also, the extraction of samples out of the capillary is prone to redilution of the product that had been accumulated previously in the trap center.

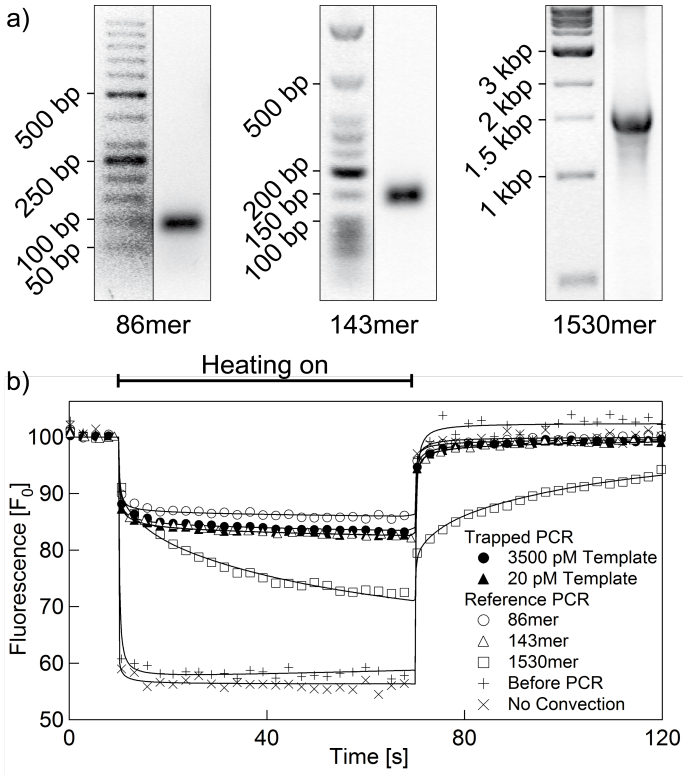

Figure 22: Verification of the product lengths. (a) Gel electrophoresis of the PCR product from a standard thermo-cycler. Different primers yield product lengths of 86, 143 and 1530 base pairs. (b) In the capillary, the product is identified using microscale thermophoresis [33, 37, 46–48]. Upon heating with a laser spot, DNA is locally depleted. The amplified product matches the 143 base pair product and is well bracketed by the 86 mer and 1530 mer product.

We therefore chose microscale thermophoresis for size determination [33, 37, 46–48]: After trapped replication, a low power IR-laser spot with a width of 100 µm leading to a modest temperature increase of 9 K was created in the trapping center. The resulting temperature gradient induces a thermophoretic depletion of labeled product which was measured over time (Fig. 22 b). To determine the relative size of the product of trapped replication, a previously cycled PCR-solution with λ-DNA and a synthetic 86mer ssDNA template was used to obtain µM concentrations of products with sizes of 1530 and 86 bases. These solutions were analyzed using microscale thermophoresis in the same borosilicate capillary used before for trapped replication. Larger product sizes yield slower relaxation times and more pronounced depletion levels. Diffusion coefficient D and thermodiffusion coefficient D_T were obtained by fitting the experimental data to the results of a finite element simulation with the experimental geometry and temperature profile as boundary conditions. The product of the replication trap agrees with the 143mer in both $D = 23\,\mu m^2/s$ and $D_T = 0.24\,\mu m^2/sK$ (solid line) and is bracketed by the shorter and longer DNA-signals. For the longer reference product (1530mer) $D = 1.7\,\mu m^2/s$ and $D_T = 0.24\,\mu m^2/sK$ was found, whereas for the shorter reference product (86mer) we obtained $D = 25\,\mu m^2/s$ and $D_T = 0.15\,\mu m^2/sK$. Microscale thermophoresis for a solution without product was found to show only the fast diffusion ki-

netics and high temperature dependence of the unbound SybrGreen I dye. The same characteristics were obtained in a PCR-solution that contained the 143mer template but was not cycled. Trapped replication therefore lead to a specific and quantitative, exponential replication of the given template.

8 Conclusion

How could molecular evolution start in the early days of earth? Though a *definite* answer to this question cannot be given, this work illustrates milestones along a *possible* pathway:

The physics of a simple thermal gradient can push forward the formation of long polymers and complex structures that are otherwise unlikely to form under prebiotic conditions. Instead of using complex chemical systems whose plausibility is still matter of discussion in the community, experiments were done using a stable and well controllable model system that applies to the given theory of trapped polymerization without the loss of generality. On the one hand, the basic theoretical model (random aggregation / dissociation) allows for a broad applicability for prebiotic polymerization reactions. On the other hand, more complex geometries could be modeled using the technique of finite element simulation combined with the steady state polymerization theory. Combined, the presented tool set states a valuable help in the search for the prebiotic process suiting best to start molecular evolution.

Interestingly, the same hydrothermal setting of trapped polymerization also suits to thermally trigger a trapped replication process. The prevention of template poisoning by the coordinated thermal reset of the replication partners allows interesting scenarios in which the advantage of faster replication of shorter templates shown by Spiegelmann ([74]) is avoided under optimal conditions: Thermal traps therefore not only increase complexity in a polymerization process but also help to maintain the complexity in a replication process ([75]) and protect the replication product against outward directed diffusion [27]. The use of a polymerase chain reaction as a proxy process for a thermally triggered replication is valid since a replication based solely on tRNA was shown to be compatible to convective thermal cycling too [29]: Here, no nucleotide but a codon sequence was replicated which maybe a bridge to the first synthesis of proteins.

Concerning boundary conditions, the process of thermal trapping in general is thought to be more efficient under low salt conditions [20]. Coincidentally, the polymerization of RNA using cGMP ([16, 17]) and the formation of the first plausible fatty acid membranes ([26, 49]) also prefer a low salt environment which may lead to the conclusion that prebiotic live started in fresh water environments. Apart from these speculations, hydrothermal pores cannot only reduce local entropy via thermogravitational trapping, but also act as a source of small organics (e.g. methane) and sulfur. It has been proposed that sulfur could have reated with iron solved in the ocean, to form micrometer thick FeS-membranes. The metallo-clusters in such membranes could have acted as a first electron transfer chain for carbon fixation, similar to that found in mitochondrial membranes [22, 76].

All these aspects represent a plausibility chain that cannot be proven for historical correctness. Nevertheless, it clearly points to a crucial role of hydrothermal pores in the origin of life. Chemical and

physical processes act together in a synergistic way that could not yet be found elsewhere. Future experiments will therefore focus on the connection and extension of these milestones, finally leading to a molecular Darwinian process as a representation of the first life form on earth.

Acknowledgments

I want to thank all people that supported me:

- Dieter Braun: This work would not have been possible without the help and guidance of my advisor. His interest and curiosity in the questions on the origin of life are infectious and very motivating.
- Ulrich Gerland: My second advisor who always had time to answer theoretical questions.
- Severin Schink: Trapped polymerization as theoretical construct confronted us with a lot of problems - Severin addressed and solved them all.
- All "Braun"-group members for being excellent and helpful colleagues. Especially I want to thank Susanne Seidel and Friederike Möller for reading the manuscript and giving valuable comments.
- All members of the group of Hermann Gaub for the nice and fruitful communication and for sharing their lab equipment (Nanodrop, GelDoc, Laser-Scanner). Especially I want to thank Angelika Kardinal and Thomas Nikolaus for the nice introduction into lab work and helpful comments.
- All members of the group of Joachim Rädler for the help in various situations and sharing their lab equipment (TEM, AFM).
- All members of the group of Tim Liedl, especially Verena Schüller and Susanne Kempter for giving the possibility to measure at the TEM.
- I want to thank my whole family for their support - especially I want to thank my wife, Elisabeth Mast.

References

[1] Benner SA (2010) Defining life. *Astrobiology* 10:1021–1030.

[2] Darwin C (2006) *On the origin of species by means of natural selection, or, The preservation of favoured races in the struggle for life* (Dover Publications, Mineola, NY), Dover giant thrift ed edition.

[3] Doolittle WF (1999) Phylogenetic classification and the universal tree. *Science (New York, N.Y.)* 284:2124–2129 PMID: 10381871.

[4] Endy D (2005) Foundations for engineering biology. *Nature* 438:449–453.

[5] Pauling L, Zuckerkandl E, Henriksen T, Loevstad R (1963) Chemical paleogenetics. molecular "Restoration studies" of extinct forms of life. *Acta Chemica Scandinavica* 17 supl.:9–16.

[6] Benner S (2007) Protein evolution. *Advances in Enzymology and Related Areas of Molecular Biology* 75:1–132.

[7] Ricardo A (2004) Borate minerals stabilize ribose. *Science* 303:196–196.

[8] Gilbert W (1986) Origin of life: The RNA world. *Nature* 319:618–618.

[9] Kruger K, et al. (1982) Self-splicing RNA: autoexcision and autocyclization of the ribosomal RNA intervening sequence of tetrahymena. *Cell* 31:147–157 PMID: 6297745.

[10] Wochner A, Attwater J, Coulson A, Holliger P (2011) Ribozyme-catalyzed transcription of an active ribozyme. *Science* 332:209–212.

[11] Johnston WK (2001) RNA-Catalyzed RNA polymerization: Accurate and general RNA-Templated primer extension. *Science* 292:1319–1325.

[12] Maher KA, Stevenson DJ (1988) Impact frustration of the origin of life. *Nature* 331:612–614.

[13] Glansdorff N, Xu Y, Labedan B (2008) The last universal common ancestor: emergence, constitution and genetic legacy of an elusive forerunner. *Biology Direct* 3:29.

[14] Ueno Y, Yamada K, Yoshida N, Maruyama S, Isozaki Y (2006) Evidence from fluid inclusions for microbial methanogenesis in the early archaean era. *Nature* 440:516–519 PMID: 16554816.

[15] Zhang N, Zhang S, Szostak JW (2012) Activated ribonucleotides undergo a sugar pucker switch upon binding to a single-stranded RNA template. *Journal of the American Chemical Society* 134:3691–3694.

[16] Costanzo G, Pino S, Ciciriello F, Di Mauro E (2009) Generation of long RNA chains in water. *The Journal Of Biological Chemistry* 284:33206–33216.

[17] Costanzo G, et al. (2012) Generation of RNA molecules by a base-catalysed click-like reaction. *ChemBioChem* 13:999–1008.

[18] Ferris JP, Hill, A R J, Liu R, Orgel LE (1996) Synthesis of long prebiotic oligomers on mineral surfaces. *Nature* 381:59–61 PMID: 8609988.

[19] Mast CB, Schink S, Gerland U, Braun D (2013) Escalation of polymerization in a thermal gradient. *Proceedings of the National Academy of Sciences* 110:8030–8035.

[20] Baaske P, et al. (2007) From the cover: Extreme accumulation of nucleotides in simulated hydrothermal pore systems. *Proceedings of the National Academy of Sciences* 104:9346–9351.

[21] Mielke RE, et al. (2011) Iron-sulfide-bearing chimneys as potential catalytic energy traps at life's emergence. *Astrobiology* 11:933–950.

[22] Martin W, Baross J, Kelley D, Russell MJ (2008) Hydrothermal vents and the origin of life. *Nature Reviews Microbiology* 6:805–814.

[23] Morgan L, et al. (2003) Exploration and discovery in yellowstone lake: results from high-resolution sonar imaging, seismic reflection profiling, and submersible studies. *Journal of Volcanology and Geothermal Research* 122:221–242.

[24] Braun D, Libchaber A (2002) Trapping of DNA by thermophoretic depletion and convection. *Physical Review Letters* 89:188103.

[25] Weinert FM, Braun D (2009) An optical conveyor for molecules. *Nano Letters* 9:4264–4267.

[26] Budin I, Bruckner RJ, Szostak JW (2009) Formation of protocell-like vesicles in a thermal diffusion column. *Journal of the American Chemical Society* 131:9628–9629.

[27] Mast CB, Braun D (2010) Thermal trap for DNA replication. *Physical Review Letters* 104:188102.

[28] Braun D, Goddard N, Libchaber A (2003) Exponential DNA replication by laminar convection. *Physical Review Letters* 91:158103.

[29] Krammer H, Moeller FM, Braun D (2012) Thermal, autonomous replicator made from transfer RNA. *Physical Review Letters* 108:238104.

[30] Debye P (1939) Zur theorie des clusiusschen trennungsverfahrens. *Annalen der Physik* 428:284–294.

[31] Ludwig C (1856) in *Sitzungsbreicht Kaiser Akad Wiss*, ed W B (Mathem-Naturwiss Cl, Vienna, AT), p 539.

[32] Duhr S, Braun D (2006) Thermophoretic depletion follows boltzmann distribution. *Physical Review Letters* 96.

[33] Duhr S, Braun D (2006) From the cover: Why molecules move along a temperature gradient. *Proceedings of the National Academy of Sciences* 103:19678–19682.

[34] Clusius K, Dickel G (1938) Neues verfahren zur gasentmischung und isotopentrennung. *Die Naturwissenschaften* 26:546–546.

[35] Schink S (2011) in *On origin and structure of RNA, Master Thesis* (Munich, BA), pp 35–36.

[36] Herzog M (2012) in *Thermophoresis and Cooperative Binding of Nucleotides* (Munich, BA), pp 25–33.

[37] Wang Z, Kriegs H, Wiegand S (2012) Thermal diffusion of nucleotides. *The Journal of Physical Chemistry B* 116:7463–7469.

[38] Reineck P, Wienken CJ, Braun D (2010) Thermophoresis of single stranded DNA. *Electrophoresis* 31:279–286.

[39] Obermayer B, Krammer H, Braun D, Gerland U (2011) Emergence of information transmission in a prebiotic RNA reactor. *Physical Review Letters* 107:018101.

[40] Mergny JL, Lacroix L (2003) Analysis of thermal melting curves. *Oligonucleotides* 13:515–537.

[41] Stryer L (1978) Fluorescence energy transfer as a spectroscopic ruler. *Annual Review of Biochemistry* 47:819–846.

[42] Podtelezhnikov AA, Mao C, Seeman NC, Vologodskii A (2000) Multimerization-cyclization of DNA fragments as a method of conformational analysis. *Biophysical journal* 79:2692–2704 PMID: 11053141.

[43] Life-Technologies (2013) Fluorescence Spectraviewer.

[44] Integrated-DNA-Technologies (2013) OligoAnalyzer 3.1.

[45] Weinert FM, Braun D (2008) Optically driven fluid flow along arbitrary microscale patterns using thermoviscous expansion. *Journal of Applied Physics* 104:104701.

[46] Duhr S, Braun D (2006) Optothermal molecule trapping by opposing fluid flow with thermophoretic drift. *Physical Review Letters* 97:038103.

[47] Seidel SAI, et al. (2012) Label-free microscale thermophoresis discriminates sites and affinity of protein-ligand binding. *Angewandte Chemie International Edition* 51:10656–10659.

[48] Wang X, et al. (2011) Peptide surfactants for cell-free production of functional g protein-coupled receptors. *Proceedings of the National Academy of Sciences* 108:9049–9054.

[49] Schrum JP, Zhu TF, Szostak JW (2010) The origins of cellular life. *Cold Spring Harbor Perspectives in Biology* 2:a002212–a002212.

[50] Olins AL, Olins DE (1974) Spheroid chromatin units (ngr bodies). *Science* 183:330–332.

[51] Solovei I, et al. (2009) Nuclear architecture of rod photoreceptor cells adapts to vision in mammalian evolution. *Cell* 137:356–368.

[52] Strzelecka TE, Rill RL (1991) Phase transitions in concentrated DNA solutions: ionic strength dependence. *Macromolecules* 24:5124–5133.

[53] Strzelecka TE, Davidson MW, Rill RL (1988) Multiple liquid crystal phases of DNA at high concentrations. *Nature* 331:457–460 PMID: 3340191.

[54] Fried MG, Bloomfield VA (1984) DNA gelation in concentrated solutions. *Biopolymers* 23:2141–2155 PMID: 6498295.

[55] Rothemund PWK (2006) Folding DNA to create nanoscale shapes and patterns. *Nature* 440:297–302 PMID: 16541064.

[56] Kuzyk A, et al. (2012) DNA-based self-assembly of chiral plasmonic nanostructures with tailored optical response. *Nature* 483:311–314.

[57] Schueller VJ, et al. (2011) Cellular immunostimulation by CpG-Sequence-Coated DNA origami structures. *ACS Nano* 5:9696–9702.

[58] Schreiber R, et al. (2011) DNA origami-templated growth of arbitrarily shaped metal nanoparticles. *Small* 7:1795–1799.

[59] Schoen I, Krammer H, Braun D (2009) Hybridization kinetics is different inside cells. *Proceedings of the National Academy of Sciences* 106:21649–21654.

[60] Krishnan M (2002) PCR in a rayleigh-benard convection cell. *Science* 298:793–793.

[61] Braun D, Libchaber A (2004) Thermal force approach to molecular evolution. *Physical Biology* 1:P1.

[62] Agrawal N, Hassan Y, Ugaz V (2007) A pocket-sized convective PCR thermocycler. *Angewandte Chemie International Edition* 46:4316–4319.

[63] Hennig M, Braun D (2005) Convective polymerase chain reaction around micro immersion heater. *Applied Physics Letters* 87:183901.

[64] Wheeler EK, et al. (2004) Convectively driven polymerase chain reaction thermal cycler. *Analytical Chemistry* 76:4011–4016.

[65] Gudnason H, Dufva M, Bang D, Wolff A (2007) Comparison of multiple DNA dyes for real-time PCR: effects of dye concentration and sequence composition on DNA amplification and melting temperature. *Nucleic Acids Research* 35:e127–e127.

[66] Eigen M, Schuster P (1978) The hypercycle. *Naturwissenschaften* 65:7–41.

[67] Eigen M (1971) Selforganization of matter and the evolution of biological macromolecules. *Die Naturwissenschaften* 58:465–523.

[68] von Kiedrowski G (1986) A self-replicating hexadeoxynucleotide. *Angewandte Chemie International Edition* 25:932–935.

[69] Kainz P (2000) The pcr plateau phase, towards an understanding of its limitations. *Biochimica et Biophysica Acta (BBA) - Gene Structure and Expression* 1494:23–27.

[70] Swillens S, Dessars B, Housni HE (2008) Revisiting the sigmoidal curve fitting applied to quantitative real-time PCR data. *Analytical Biochemistry* 373:370–376.

[71] Zipper H (2004) Investigations on DNA intercalation and surface binding by SYBR green i, its structure determination and methodological implications. *Nucleic Acids Research* 32:e103–e103.

[72] Tyagi S, Kramer FR (1996) Molecular beacons: probes that fluoresce upon hybridization. *Nature biotechnology* 14:303–308 PMID: 9630890.

[73] Holland PM (1991) Detection of specific polymerase chain reaction product by utilizing the 5' 3' exonuclease activity of thermus aquaticus DNA polymerase. *Proceedings of the National Academy of Sciences* 88:7276–7280.

[74] Spiegelman S, Haruna I, Holland IB, Beaudreau G, Mills D (1965) The synthesis of a self-propagating and infectious nucleic acid with a purified enzyme. *Proceedings of the National Academy of Sciences* 54:919–927.

[75] Lanzmich S (2012) in *Accumulation and Replication in Prebiotic Environments* (Munich, BA), pp 29–42.

[76] Russell MJ, Hall AJ (1997) The emergence of life from iron monosulphide bubbles at a submarine hydrothermal redox and pH front. *Journal of the Geological Society* 154:377–402.

Part III
Appendix

10 Publications

1. C. B. Mast, S. Schink, U. Gerland, and D. Braun:
   "Escalation of polymerization in a thermal trap"
   PNAS, 2013, doi: 10.1073/pnas.1303222110

2. C. B. Mast, D. Braun:
   "Thermal Trap for DNA Replication"
   PRL., 2010, 104, 188102

---

1. C. B. Mast, N. Osterman, and D. Braun:
   “Thermal Solutions for Molecular Evolution”
   IJMPB, 2012, doi: 10.1142/S0217979212300174

2. F. M. Weinert, C. B. Mast, and Dieter Braun:
   "Optical fluid and biomolecule transport with thermal fields"
   PCCP, 2011, doi 10.1039/C0CP02359K

3. C. B. Mast, N. Osterman, and D. Braun:
   "Disequilibrium First: The Origin of Life"
   Journal of Cosmology, 2010, Vol 10, 3305-3314

Escalation of polymerization in a thermal gradient

Christof B. Mast[a,1], Severin Schink[b,1], Ulrich Gerland[b], and Dieter Braun[a,2]

[a]Systems Biophysics, Physics Department, Center for Nanoscience, and [b]Arnold-Sommerfeld-Center for Theoretical Physics and Center for Nanoscience, Ludwig-Maximilians-Universität München, 80799 Munich, Germany

Edited* by Nigel Goldenfeld, University of Illinois at Urbana–Champaign, Urbana, IL, and approved April 3, 2013 (received for review March 1, 2013)

For the emergence of early life, the formation of biopolymers such as RNA is essential. However, the addition of nucleotide monomers to existing oligonucleotides requires millimolar concentrations. Even in such optimistic settings, no polymerization of RNA longer than about 20 bases could be demonstrated. How then could self-replicating ribozymes appear, for which recent experiments suggest a minimal length of 200 nt? Here, we demonstrate a mechanism to bridge this gap: the escalated polymerization of nucleotides by a spatially confined thermal gradient. The gradient accumulates monomers by thermophoresis and convection while retaining longer polymers exponentially better. Polymerization and accumulation become mutually self-enhancing and result in a hyperexponential escalation of polymer length. We describe this escalation theoretically under the conservative assumption of reversible polymerization. Taking into account the separately measured thermophoretic properties of RNA, we extrapolate the results for primordial RNA polymerization inside a temperature gradient in pores or fissures of rocks. With a dilute, nanomolar concentration of monomers the model predicts that a pore length of 5 cm and a temperature difference of 10 K suffice to polymerize 200-mers of RNA in micromolar concentrations. The probability to generate these long RNAs is raised by a factor of $>10^{600}$ compared with polymerization in a physical equilibrium. We experimentally validate the theory with the reversible polymerization of DNA blocks in a laser-driven thermal trap. The results confirm that a thermal gradient can significantly enlarge the available sequence space for the emergence of catalytically active polymers.

molecular evolution | nonequilibrium | RNA world | (nonenzymatic) emergence of RNA | hydrothermal vents

Polymers are the vital building blocks of all known life forms. According to the central dogma of molecular biology (1), DNA stores the information for how and when to build proteins, which for their part carry out catalytic tasks like the polymerization of DNA. How this self-perpetuating cycle has started is unknown. The RNA-world hypothesis posits that RNA molecules were the central players in prebiotic evolution, because they exhibit both a catalytic function similar to that of proteins and the information storage capabilities of DNA (2). However, how could such an RNA world have emerged from the prebiotic soup?

A key element of the RNA world is a ribozyme that catalyzes RNA replication. Directed in vitro evolution and engineering have shown that such ribozymes exist, but require a length of 200 bases or more, even in favorable high-salt conditions (3). Starting from chemical nonequilibrium conditions with millimolar concentrations of energy-rich nucleotides (4–6) and with the help of catalytic surfaces (7), only the formation of much shorter polynucleotides on the order of 20 bases was demonstrated in the laboratory. Slow kinetics and cleavage due to hydrolysis limit the formation of long polynucleotides and finally lead to a length distribution that decays exponentially in the case of reversible polymerization, i.e., RNA constantly being randomly built up and cleaved. A simple estimate shows that to obtain a traceable concentration of 200-mer RNAs, the concentration of nucleotides has to exceed the effective dissociation constant by at least 100-fold (Fig. S1). Plausible concentrations of nucleotides in primordial settings, e.g., a hydrothermal vent or a warm pond, should be at most in the nanomolar to low micromolar range. However, the binding affinity for nucleotide monomer binding to an oligomer is weak, with estimates for the dissociation constant in the millimolar range (4). Even if dissociation constants in the micromolar range can be reached by specifically activated nucleotides, the nonenzymatic formation of 200-mers seems impossible in a setting that is not supported by an additional physical nonequilibrium.

In this work we demonstrate escalated polymerization in a spatially confined thermal gradient as a possible pathway for RNA to overcome this barrier. The physical nonequilibrium condition in the form of an ordinary temperature gradient will lead to exceedingly long polymers, even under the conservative assumption of reversible polymerization. In an elongated convection cell, thermophoresis accumulates macromolecules like DNA and RNA in a length-selective manner (Fig. 1*A*). We study how such a thermal molecule trap produces a continuing chemical nonequilibrium condition and thereby affects a weak, reversible polymerization reaction based on bonding of monomers and oligomers and random dissociation (Fig. 1*B*). Using a combination of experimental and theoretical methods, we identify conditions under which the interplay of these mechanisms dramatically increases the length range and efficiency of the polymerization process (Fig. 1*C*).

A thermal gradient in an elongated compartment arguably was an abundant physical scenario in the prebiotic world. The compartment could be a pore in volcanic rock, a cleft of mud, or a rock fissure with the temperature gradient caused by the vicinity of a warm hydrothermal or volcanic outflow into a colder ocean (8, 9). This could be found in both salty oceanic hydrothermal conditions (10) and the fresh waters near warm water ponds (11). In the laboratory, thermal molecule traps have previously been demonstrated to support accumulation of biomolecules (12, 13), formation of cell-like lipid vesicles (14), and concurrent replication and trapping with a polymerase (15, 16). Additionally, a replication of codon information using tRNA is compatible with the temperature cycling in a thermal molecule trap (17).

This previous work used the thermal trap as a passive length-selective concentration enhancer without biochemical reactions (12, 13) and replicators with fixed product length (14–16). Here, we show how the length selectivity of thermal traps and a linear polymerization reaction with arbitrary product lengths mutually enhance each other by a coupling between physical and chemical nonequilibrium (Fig. 1*C*): The thermal trap accumulates monomers and thereby pushes the system out of chemical equilibrium. Longer polymers are created due to the concentration-dependent polymerization. The longer polymers are accumulated more efficiently by the length-selective physical nonequilibrium of the thermal trap, which in turn leads to higher local concentrations. The positive feedback loop allows the formation of long RNA polymers even at low nucleotide concentrations. We validate our theory experimentally in the fast polymerizing regime, using a laser-

Author contributions: C.B.M., S.S., U.G., and D.B. designed research; C.B.M., S.S., U.G., and D.B. performed research; C.B.M., S.S., U.G., and D.B. analyzed data; and C.B.M., S.S., U.G., and D.B. wrote the paper.

The authors declare no conflict of interest.

*This Direct Submission article had a prearranged editor.

Freely available online through the PNAS open access option.

[1]C.B.M. and S.S. contributed equally to this work.

[2]To whom correspondence should be addressed. E-mail: dieter.braun@lmu.de.

This article contains supporting information online at www.pnas.org/lookup/suppl/doi:10.1073/pnas.1303222110/-/DCSupplemental.

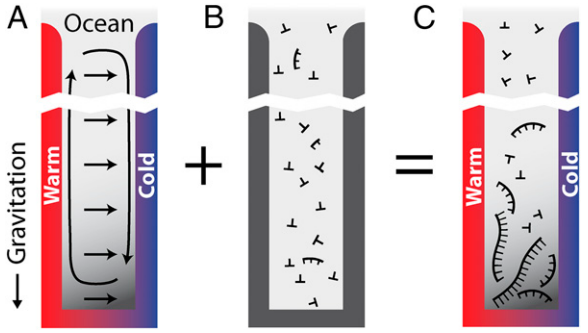

Fig. 1. Proposed polymerization in a thermal gradient: cross section of a water-filled pore that is exposed to the ocean at the top and subjected to a spatially confined horizontal temperature gradient. (*A*) Thermal trapping. The temperature gradient drives thermal convection (circular arrows) due to the thermal expansion of water at the hot side. Additionally, solved biomolecules move from hot to cold via thermophoresis with a drift speed $v_T = D_T \cdot \nabla T$ (horizontal arrows). In combination, solved biomolecules are accumulated at the pore bottom, exponentially dependent on their Soret coefficient $S_T \equiv D_T/D$. Because S_T increases with the molecule length, longer molecules are trapped exponentially more efficiently at the optimal trap width. (*B*) Polymerization. If polymerization and dissociation are in steady state, the concentration of longer polymers decays exponentially with polymer length. The mean length strongly depends on the concentration of monomers and is too short to allow for self-replicating polymers under dilute primordial conditions. (*C*) Trapping and polymerization. The exponential thermal accumulation can counterbalance the exponentially decaying polymerization. As a result, both the concentration and the mean length of the polymers are enhanced massively.

driven thermal trap filled with a solution of double-stranded DNA blocks, which reversibly polymerize at specifically designed sticky ends. The experiment was designed to fully control all parameters of the system. We record this polymerization process in real time and find a quantitative agreement with our theoretical model.

Theory

Thermal Molecule Trap. To study the interplay between thermal trapping and polymerization, we first describe the dynamics of each process separately and then consider the coupled processes. In a water-filled compartment, vertical gravitation and a horizontal temperature gradient ∇T lead to a laminar convective flow due to the thermal expansion of the fluid (Fig. 1*A*). Additionally, dissolved biomolecules with a thermodiffusion coefficient D_T will thermophoretically move along the thermal gradient with a drift speed $v_T = D_T \cdot \nabla T$. Charged molecules have a tendency to move toward the cold, a trend that can be understood from local free energy considerations (18–21). In a thermal molecule trap, both effects are combined: The biomolecules are accumulated at the bottom corner of the compartment until a steady state of thermodiffusion and the counteracting diffusion is reached. Such an accumulation effect was first observed in gases by Clusius and Dickel for chlorine isotopes (22).

We describe the accumulation of molecules inside a thermal trap, using a 2D transport equation of the drift-diffusion type for the concentration $c(x,y,t)$ of biomolecules (23),

$$\frac{\partial c}{\partial t} = D\left(\frac{\partial^2 c}{\partial x^2} + \frac{\partial^2 c}{\partial y^2}\right) + S_T D \frac{dT}{dx}\frac{\partial c}{\partial x} + v(x)\frac{\partial c}{\partial y}. \qquad [1]$$

Here, x is the horizontal coordinate in Fig. 1*A*, y is the vertical coordinate, and t denotes time. The three terms on the right account for diffusion, thermodiffusion, and convection. The two latter effects are evoked by the linear temperature gradient $dT/dx = \Delta T/w$ over the horizontal width w of the pore, where ΔT denotes the (fixed) temperature difference between the left and right boundaries. On the one hand, the gradient yields a thermodiffusive flux in the x direction with D the diffusion coefficient and $S_T \equiv D_T/D$ the length-dependent Soret coefficient of the dissolved molecule (18). On the other hand, thermal expansion leads to a vertical convection flow with the velocity profile $v(x)$ (*SI Text A*). The characteristic velocity, $v_0 = \beta g \rho \Delta T w/72\sqrt{3}\eta$, also depends on the gravitational acceleration g and the density ρ, viscosity η, and thermal expansivity β of the solvent (Fig. S2*D*).

Eq. **1** can be solved by separation of variables. In the steady state, the concentration $c(x,y) = U(x)V(y)$ increases exponentially along the vertical direction, $V(y) = \exp(-\alpha y)$ with the accumulation coefficient α fixed by the solution of $U(x)$. The detailed calculation (*SI Text A*) shows that $\alpha \sim S_T \partial T/\partial x$, predicting that the total accumulation in the vertical direction scales exponentially with the Soret coefficient S_T. Because longer DNA or RNA molecules have larger S_T, they can be exponentially stronger accumulated in the thermophoretic trap.

Polymerization. We describe the chemical dynamics of a generic polymerization process as a reversible aggregation–fragmentation reaction (24),

$$\frac{dc_n}{dt} = \frac{1}{2}\sum_{i+j=n} k_{ij}^{on} c_i c_j - c_n \sum_{j>0} k_{nj}^{on} c_j + \sum_{j>0} k_{nj}^{off} c_{j+n} - \frac{1}{2} c_n \sum_{i+j=n} k_{ij}^{off}, \qquad [2]$$

for the concentration c_n of a polymer with length n. The concentration c_n can increase via bonding of two shorter polymers (first term on right-hand side) or via the dissociation of a longer polymer (third term), whereas it can also decrease via bonding (second term) and dissociation (fourth term). Cyclization or formation of nonproductive complexes is not considered here. The dynamics are governed by the on and off rates, k_{ij}^{on} and k_{ij}^{off}. Under the "worst-case" assumption that these rates satisfy the detailed balance condition (25) (instead of supporting a finite flux driven by a separate chemical activation process), the steady state of Eq. **2** is

$$c_n = c_1^n \prod k_{1x}^{on}/k_{1x}^{off}, \qquad [3]$$

see *SI Text A* for details. Via summation over Eq. **3** the concentration of free monomers, c_1 can be related to the total local concentration $c_0 = \sum n c_n$ of all monomers inside a finite volume element ΔV. By inverting this functional dependence numerically, we obtain the polymer length distribution $c_n(c_0)$. The $c_n(c_0)$ fully characterizes the steady state of the polymerization process. The simplest observable is the mean polymer length $\langle n \rangle = c_0/\sum c_n$, which corresponds to the ratio of the total monomer concentration to the total concentration of polymer molecules of any size inside ΔV. We will see that the experimental fluorescence resonance energy transfer (FRET) signal considered below is directly related to the mean length via $FRET = 1 - 1/\langle n \rangle$.

Polymerization and Trapping. The precise interplay of polymerization and thermal trapping depends on the relation between their characteristic timescales. A full analysis of the coupled dynamics would require solving Eqs. **1** and **2** simultaneously, which is computationally intensive. For our purposes it suffices to consider the two adiabatic limits of this system: The limit where the polymerization reaction is fast and always remains equilibrated during the accumulation process is adequate to describe the experiments reported below, as well as for the prebiotic scenario of RNA polymerization explored below. The opposite limit where polymerization is slow or quasi-frozen over the timescale of the accumulation is covered in *SI Text C*.

The characteristic timescale $\tau_a = 1/\alpha v_0$ of accumulation is the transport time for a molecule over the accumulation length scale of the trap $1/\alpha$ at the characteristic flow velocity v_0. In the polymerization reaction, a characteristic time τ_p is obtained from the typical on rate and polymer concentration. For fast

polymerization ($\tau_p << \tau_a$), $c_n(c_0)$ always equilibrates according to the current local concentration $c_0 = c(x,y)$ inside the trap. One can then approximate the accumulation process by solving Eq. **1** with an effective diffusion coefficient $\overline{D}(c_0)$ and Soret coefficient $\overline{S}_T(c_0)$ (*SI Text A*). In the other extreme of slow polymerization ($\tau_p >> \tau_a$), the trapped concentrations of the polymer are independently amplified for each length by the accumulation factor of the thermal trap (8).

Trapped RNA Polymerization Under Primordial Conditions. We extrapolate our theory to the scenario of RNA polymerization inside a thermal trap (8) (Fig. 2). We consider a rectangular elongated compartment and assume a reasonable temperature difference of 10 K. Smaller temperature gradients would require only linearly elongated pores with slower equilibration times (16). We assume that the pore is diffusively coupled to an infinitely large ocean or pond, and therefore we fix the local monomer concentration at the top of the pore at c_0. The bottom of the pore is closed and the fluid flow is fully characterized by convection. We assume that the RNA polymerization reaction is in the activation-controlled regime where the diffusive association is faster than the binding reaction and the on rate is independent of length, $k_{nm}^{on} = \text{const}$. A constant off rate is a good approximation for short polymers and poses an upper bound for long polymers, because base pairing can significantly enhance the stability of a bond. As a reference, we chose an outside concentration of 1 nM and keep it smaller than the temperature-averaged dissociation constant K_D to reflect that only monomers exist in the primordial solution outside the trap.

Concerning thermophoretic properties of RNA, we use recent measurements of diffusion and Soret coefficients of RNA (20, 26) as documented in *SI Text A* (Fig. S3 *C* and *D*). Temperature and salt concentration play a crucial role because they have a considerable impact on the Soret coefficient of RNA. We investigated three possible primordial scenarios. For a physiological salt concentration (150 mM NaCl, $\lambda_{Debye} = 0.8$ nm) we consider an enhanced average trap temperature (55 °C, Fig. 2 and Fig. S4, *III*) and colder water (25 °C, Fig. S4, *I*). In addition, a salt-deprived scenario (3 mM NaCl, $\lambda_{Debye} = 5.6$ nm, Fig. S4, *II*) is analyzed, where the temperature does not change the Soret coefficients sufficiently. For the warm and salty scenario shown in Fig. 2, the experimental scaling laws for diffusion and Soret coefficients were fitted by $D(n) = 643 n^{-0.46}$ μm^2/s and $S_T(n) = (5.3 + 5.7 n^{0.73}) \times 10^{-3}$ K^{-1} (Fig. S3 *C* and *D*). Despite the fact that the Soret coefficients decrease with increasing salt concentration (18, 20), we will see that the exponential trap results in very similar outcomes for our three scenarios, demonstrating the robustness of the escalation effect.

Theoretical Results. The capability of the thermal trap to produce long polymers is shown in Fig. 2. We discuss fast polymerization (Fig. 2 *A*–*C*) and slow polymerization (Fig. S4, *III*) for various dissociation constants of polymerization K_D. In both regimes, polymers of considerable size are found inside the trapping region. To stay in the fast reaction regime, the relaxation time of the polymerization process has to obey $\tau_p << 1/\alpha v_{max} \approx 30$ min. The concentration distribution inside the compartment is solved using the adiabatic treatment described above, with effective diffusion and Soret coefficients defined according to the polymer length distribution as a function of the total concentration of monomers. Fig. 2*A* shows the length distribution in the chemical steady state for pore lengths between 2.5 and 4 cm (black boxes 1–4) at fixed width of 100 μm [which is optimal for the trapping of longer polymers (*SI Text A*)] and with a dissociation constant of $K_D = 10$ μM with and without the continuing physical nonequilibrium of a thermal trap. Although dimers are barely existent outside the trap, RNA polymers of more than 100 bases are produced, exceeding even the nanomolar monomer concentration outside the trap. The dependence on trap length is illustrated in Fig. 2*B*. As soon as the accumulated monomer concentration reaches the threshold K_D, long polymers with higher Soret coefficients are formed. Therefore, the effective Soret coefficient $\overline{S}_T$ becomes

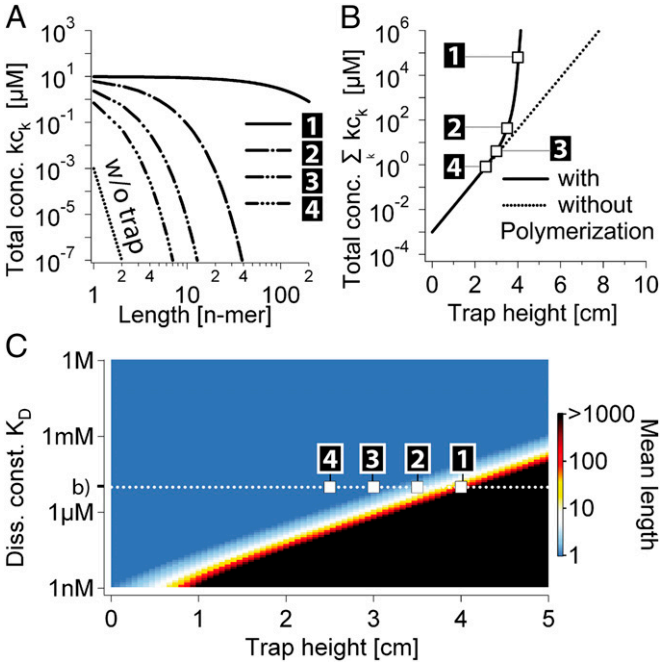

Fig. 2. RNA polymerization: accumulation and polymerization of RNA at the bottom of a primordial geothermal fissure. (*A*) Length distribution of a fast-reacting polymer ($\tau_p < 30$ min) inside a 2.5- to 4-cm (black boxes 1–4)-long trap at 100 μm width with a temperature difference of 10 K, an average trap temperature of 55 °C, a dissociation constant of $K_D = 10$ μM for polymerization, and an outside monomer concentration of 1 nM at physiological salt concentration (150 mM NaCl, $\lambda_{Debye} = 0.8$ nm). Oligomers with the size of active ribozymes are predicted to exist in the trap. (*B*) Escalation of polymerization. As soon as the total concentration of RNA monomers reaches the K_D of polymerization, the polymer length and therefore the effective Soret coefficient of the polymers increase with the trap height h_{trap}. Therefore, $c(h_{trap}) \sim \exp(\text{const} \cdot h_{trap} \cdot \overline{S}_T(h_{trap}))$ grows hyperexponentially with h_{trap}. (*C*) Mean polymer length vs. pore heights and a broad range of dissociation constants K_D. Even for low affinities, a plausible trap height is found at which polymerization escalates and the polymer length diverges. For polymerization slower than the accumulation, a similar behavior is found (Fig. S4, *III*). We conclude that the escalating growth of RNA length by a thermal trap is a robust phenomenon irrespective of the speed of polymerization.

dependent on the trap length h_{trap}, leading to a hyperexponential escalation of the total RNA concentration with the trap length according to $c(h_{trap}) \sim \exp(a \cdot h_{trap} \cdot \overline{S}_T(h_{trap}))$ with a being a constant value (Eq. **S9a**). The time at which hyperexponential trapping is found strongly depends on the trap length and specific shape. A 1,000-fold drop in polymerization affinity is easily balanced by a mere extension of the trap. Also a larger trap aperture presumably leads to faster trap relaxation. Because in literature values of K_D for a possible RNA polymerization reaction are only vaguely known, Fig. 2*C* shows the mean polymer length for a broad range of possible dissociation constants and pore lengths, including a K_D of around 10 mM for RNA polymerization measured by the Szostak group (4). In all cases, moderate trap geometries of less than 10 cm lead to polymers longer than the above-mentioned 200 nt needed for a self-replicating ribozyme. Considering the worst-case character of our reversible polymerization, models based on activated monomers are expected to generate longer polymers in even smaller traps.

For a slow polymerization ($\tau_p >> \tau_a$), we similarly find oligomers of considerable length inside the trap (Fig. S4, *III*). Therefore, we conclude that the growth of RNA by a thermal trap mechanism is a robust phenomenon, significantly enhancing the range within which RNA can be polymerized, even with inefficient polymerization reactions. The escalation of polymerization by thermal traps persists over a wide range of possible primordial conditions.

Experiment

Experimental Model System. To verify the theory of accumulation-enhanced polymerization, we locally accumulated a reversibly polymerizing model system with a laser-driven thermal trap (16). The degree of polymerization as well as the local polymer concentration was measured in real time and comparable with the predicted values from theory and simulation. Care was taken to be able to define and measure all relevant parameters. In existing RNA polymerizing systems the small size of the monomers does not allow for real-time measurements in the picoliter volumes of the trap via, e.g., fluorescence microscopy. We chose larger fluorescently labeled and reversibly polymerizing DNA blocks to implement the polymerization scheme (Fig. 3*A*). This model system allows for a complete control over all relevant experimental parameters [D, S_T, $K_D(T)$], which is not possible in an RNA-based system to this date. Despite using DNA, the experimental realization covers all aspects of the used polymerization theory without loss of generality.

We chose two single strands of DNA with a 95-bp-long homologous sequence flanked by 25-bp long sticky ends. At experimental trap conditions, this yields a stable block of double-stranded DNA (dsDNA) with two self-complementary binding sites. The dsDNA blocks are able to reversibly bind to each other via hybridization to form polymers. The polymer-binding energies are directly correlated to the length of the sticky ends. With known hybridization kinetics of DNA, polymerization kinetics ($\tau_p \approx 10$ s) were faster than the trap kinetics ($\tau_a \approx 1$ h). To measure the degree of polymerization, each sticky end is labeled with a complementary fluorescent dye called donor and acceptor. When a dimer is created, both dyes are brought in close proximity. The donor dye is then quenched by FRET toward the acceptor dye, which will emit the transferred energy as fluorescent light. The normalized efficiency of this transfer is a direct measure for the degree of polymerization, whereas the direct acceptor fluorescence determines the absolute concentration of dsDNA blocks. At a trap temperature of 53 °C, the initial average polymer length equilibrated at a value of 1.7 DNA blocks, which corresponds to a total average length of ~200 bp.

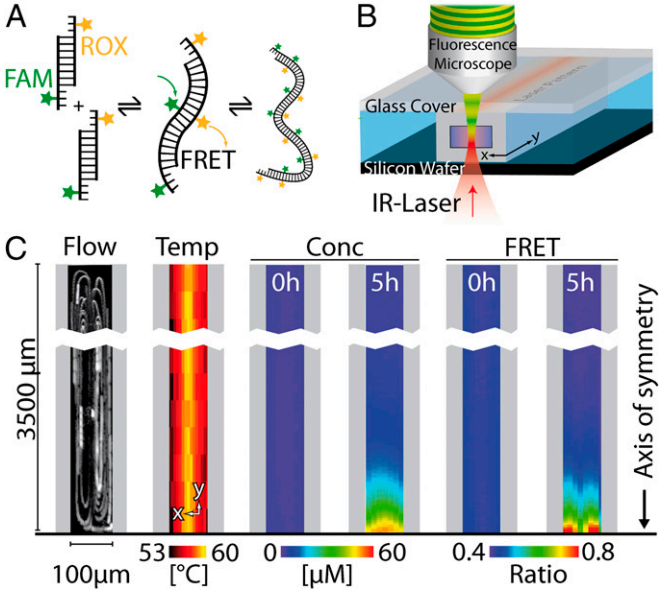

Fig. 3. Experimental model system. (*A*) Double-stranded DNA with two sticky ends serves as a monomer for the polymerization. The sticky ends have a melting temperature of 55 °C and are labeled with a FRET dye pair (FAM as donor, ROX as acceptor). (*B*) The absorption of a symmetrically moved IR laser spot in the center of a 50-µm (height) × 100-µm (width) borosilicate capillary creates thermoviscous convection flow and thermal gradients. (*C*) The fluid flow has four symmetric convection rolls that model four hydrothermal pores connected at their bottom and hot sides. The temperature profile ($T = 53$–60 °C) is measured using temperature-sensitive fluorescence. The total monomer concentration c_0 is inferred from the acceptor fluorescence and the polymerization is recorded using FRET.

We used an improved version of the laser-driven thermal trap described in ref. 16, which allows us to set the convection speed and the temperature gradient independently of the pore width w (Fig. 3*B*). An infrared laser was focused inside the filled 50-µm (height) × 100-µm (width) borosilicate capillary from below. Light absorption and the rapid movement of the IR laser along the long symmetry axis of the capillary created an elongated (length: 2 × 3,500 µm) and inwardly directed temperature gradient. Additionally, thermoviscous pumping (27) induced four symmetric convection rolls, when an asymmetric laser pattern was applied (Fig. 3*C*, Flow), which corresponds to four thermal traps that are connected at their hot and bottom sides as symmetric boundaries (Fig. 1*A* and Fig. S2). Alternating light-emitting diode (LED) excitation provided access to all four excitation and emission channels of the carboxy-X-rhodamine (ROX) and fluorescin amidite (FAM) dye, which was required to measure the fraction of closed bonds and the local concentration of monomers. A typical experimental temperature profile, monomer concentration, and FRET signal at the beginning and end of an experiment are shown in Fig. 3*C*.

The dsDNA block has three relevant physical parameters: The diffusion coefficient D, the Soret coefficient S_T, and the temperature-dependent monomer–monomer dissociation constant, $K_D = k_{11}^{off}/k_{11}^{on}$. We determined all three parameters in independent experiments. K_D was measured via a melting-curve analysis of a modified DNA that could form only dimers (Fig. S3*A*). D and S_T were both quantified by microscale thermophoresis (18, 26, 28–30), using an unreactive control monomer lacking sticky ends. To obtain the diffusion and Soret coefficients for multimers, we combined the monomer properties with the scaling laws established in ref. 18, yielding $D(n) = 65n^{-0.75}$ µm^2/s and $S_T(n) = 0.1n^{0.5}$ K^{-1}. These experimental constraints turn Eqs. **1** and **2** into a predictive theoretical model for our system. Due to its size, the dsDNA monomer diffuses slowly and reacts quickly via base pairing; we assumed diffusion-controlled association rates between monomers and multimers, $k_{1n}^{on} \sim [D(1) + D(n)]$. As all bonds within the polymer are identical, a length-independent dissociation rate can be assumed, $k_{nm}^{off} = k^{dis}$. Taken together, this yields $k_{1n}^{off}/k_{1n}^{on} = 1.14 \times (0.5 + 0.5n^{-0.75})^{-1} \times 10^{-6}$ M, which allows a theoretical prediction of the steady-state concentrations $c_n(c_0)$, using Eq. **3**.

Experimental Results. In Fig. 4*A*, the time lapse of accumulation in the trap center and at the edge is shown. Laser pumping drove the fluid in circular motion at a speed of 28 µm/s and established a temperature gradient of 7 K. Accumulation sets in immediately, depleting the edges of the trap and filling the center, reaching a constant concentration ratio between the trap center and the edge after 6 h. The edge was subsequently filled via diffusive influx from the outside of the trap, a process that is predicted to take several months (Fig. S3*B*). Therefore, linear syringe pumping across the capillary was performed during the complete experiment. An average flow speed of 1 µm/s was used to enhance diffusion-driven filling of the trap in a reasonable amount of time. To describe this more complex system, we included the analytical results of Eq. **1** in a 2D finite-element simulation by considering effective diffusion and Soret coefficients $\overline{D}$ and $\overline{S}_T$ and a temperature-dependent dissociation constant $K_D(T)$ (Fig. S2). Because all relevant parameters [diffusion and Soret coefficients, $K_D(T)$, temperature, and convection flow velocity] were measured separately, no fit parameters were required to describe the experiment by the simulation. The 2D approximation of the 3D experimental system has been verified in previous work (8, 16). Boundary effects can be neglected for large dimensions in the z direction whereas for smaller dimensions, the effect of a parabolic profile is averaged by diffusion.

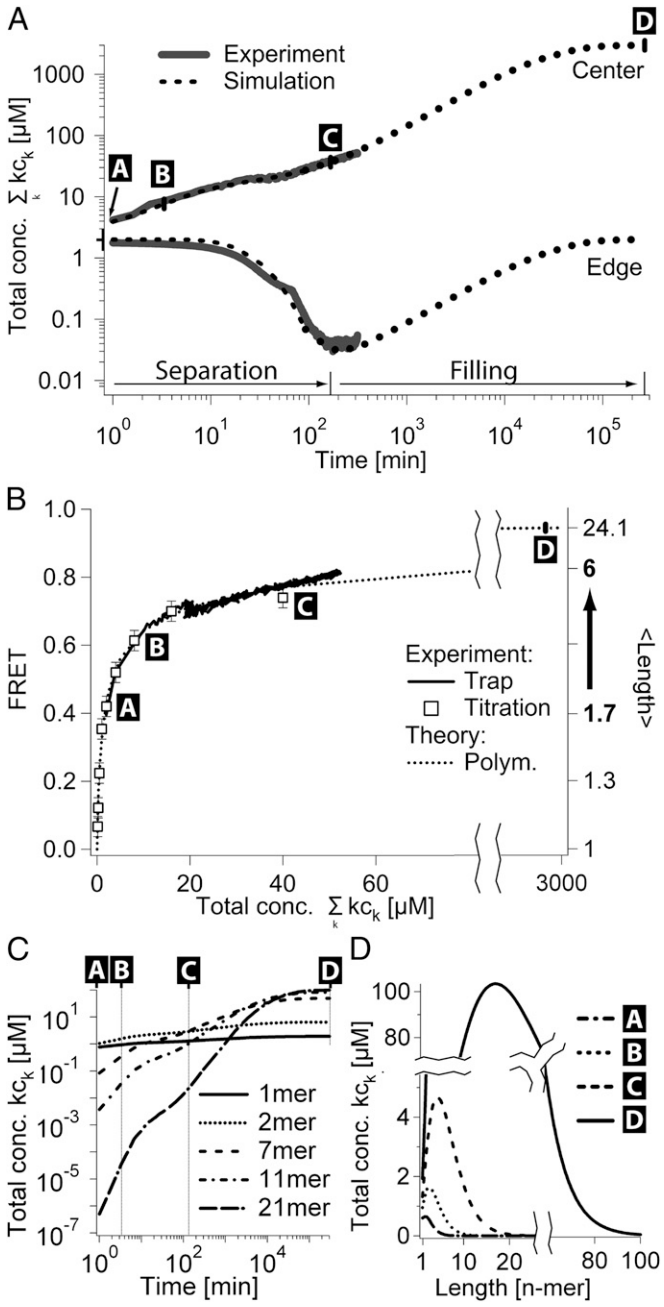

Fig. 4. Experimental data compared with simulation. (*A*) Simulated and measured monomer concentration in the center and at the edge of the trap with a flow-through drift of 1 μm/s. The initial monomer concentration was 2 μM (time-point A). The separation ratio $\sum kc_{k,center} / \sum kc_{k,edge}$ is increased (separation phase) until the steady state of concentrations within the trap is reached after 6 h (time-point C). The monomer concentration in the trap edges is depleted by two orders of magnitude. By drift and diffusion from the surrounding bulk reservoir, the trap is filled until the trap edge reaches the concentration of the outside bulk reservoir (filling phase). Due to the restricted one-dimensional geometry outside the trap, filling is inefficient and requires several weeks (time-point D). (*B*) The FRET signal is a direct measure for the mean length of the polymer, plotted against the total monomer concentration in the trap center. During the complete experiment, the relationship between concentration and mean length matches the polymer theory without fitting parameters. The same relationship is obtained by titration in bulk solution (open squares). (*C* and *D*) The polymerization theory describes the time evolution of length distribution and polymer concentration. The mean polymer length increases from 1.7 (equivalent to ~200 bp, time-point A) to 24 monomers (equivalent to ~2,880 bp, time-point D).

Four different time points are indicated by letters A–D in Fig. 4 and Fig. S3*B*. After 6 h (C in Fig. 4 and Fig. S3*B*), the concentration ratio between the trap center and the edge reached a fixed value by reducing the monomer concentration at the trap edge. Only at a later time point (D in Fig. 4 and Fig. S3*B*), also the absolute monomer concentration inside the trap reached its steady state. At this time, monomers are accumulated more than 1,000-fold inside the trap. The physical nonequilibrium of the thermal trap is still required after time-point D to maintain the length-enhanced chemical equilibrium of polymerization. In Fig. 4 *C* and *D*, the polymer concentration and length distribution at the respective time points A–D of the experiment are shown. The trapped polymerization results in the concentration of 11-mers being larger than the concentration of monomers. In the final state (D in Fig. 4 and Fig. S3*B*), polymers consisting of 100 monomers or a corresponding length of 12,000 bp are expected. Fig. 4*B* shows the FRET signal recorded during the accumulation experiment (solid line). It precisely matches the theoretical prediction of our polymerization theory (dashed line), which we had calibrated using the FRET signals obtained by titration in a heated, non-convecting, nonaccumulating trap (open squares).

Assumptions, such as the omission of cyclization reactions and the diffusion-controlled limit for the experimental system, are supported by the agreement of Eq. **2** to the titration values. Furthermore, the agreement between the dynamic and static experiments (Fig. 4*B*) shows that at every time point polymerization is faster than the thermal trap as assumed in theory. This corresponds to a small perturbation of the chemical equilibrium of polymerization by the continuing physical nonequilibrium of the thermal trap until the final length distribution is reached. This gives us the confidence to extrapolate the findings toward a prebiotic scenario, implemented solely by using the experimentally verified theory of accumulation-enhanced polymerization, but with RNA parameters and a gravitationally driven trap instead of a laser-driven one.

Discussion

Our detailed theory to describe accumulation and polymerization in a thermal gradient is based on realistic assumptions and uses experimentally measured parameters. It connects physical and chemical nonequilibrium systems that are plausible in a primordial setting. The polymerization of RNA in thermal traps can be predicted because reliable measurements of the thermophoretic parameters of RNA for different lengths at various salt concentrations are available. In various scenarios, a critical length of the trap is found for which the accumulation reaches the dissociation constant of polymerization. Beyond this critical trap length, the trapped concentration diverges hyperexponentially and the RNA length distribution reaches lengths beyond 100 bases (Fig. 2*C*). Because the thermophoretic coefficients depend only moderately on concentration, significant reductions of the ionic contributions to thermophoresis are expected only well beyond millimolar concentrations (18) and are unlikely to vanish due to hydrophobic contributions.

The kinetics of the trap can require weeks and years in the simple linear geometry discussed here. As the outside molecules have to access the trap by diffusion, the equilibration timescale of the trap increases linearly with the concentration ratios. Reaching the point (2) in Fig. 2 *A*–*C* by pure linear diffusion demands 100 y. However, alternative geometries with, e.g., a larger trap aperture for increased diffusive influx or with a continuous overflow of ocean water perpendicular to the hydrothermal convection allow reaching the steady state much faster.

The proposed mechanism of trapped polymerization is well suited for low salt concentrations used, for example, in RNA polymerization from cyclic nucleotides (5). The polymerization requires cGMP in millimolar concentrations, which could be enriched from catalytically active rock surfaces (31). In general, surface catalysis on rock particles of the micrometer scale such as clay (7) is highly compatible, because larger particles show only minor accumulation due to their slow diffusional response time. For example, 1-μm beads cycle under conditions at which DNA

strongly accumulates (Movie S1), forcing molecules to reversibly attach and detach at the particle surface.

The thermal gradient and convection not only support accumulation and polymerization but also are capable of triggering and preserving the propagation of information, a vital requirement of the RNA world. When following a convection path, oligonucleotides are exposed to temperature oscillations that can trigger exponential replication reactions (15, 16). Compared with the isothermal case, replication is not faster for shorter oligomers and thus does not lead to the degeneration of information by shortening of the replicates as demonstrated by Spiegelmann's pioneering experiments (32). Thermally triggered replication (PCR) is compatible with thermal trapping: In previous work, DNA was replicated with a polymerase every 30 s in a laser-driven thermal molecule trap (16). Also the protein-free replication of codon information can be approached by using truncated tRNA molecules in a thermal oscillation (17). Other physical nonequilibrium mechanisms to drive replication have also been explored, such as a mechanical disequilibrium-induced pattern of replication in larger DNA complexes (33). Isothermal RNA ligation could be used for a mutual ligation chain reaction (34). Techniques from DNA machines could be used to form oligomers (35) and trigger sequence-determined polymer synthesis (36). Interestingly, important steps in peptide synthesis can be catalyzed by simple RNA molecules under physiological conditions (37). In addition, it was recently shown theoretically by modeling RNA ligation in a thermophoretic trap that sequence information transmission can be initiated by differential degradation in a thermal oscillation (38). More generally, the framework of nonequilibrium statistical thermodynamics can be used as a unifying theoretical framework to describe the generation of sequence information, using chemical and physical nonequilibrium processes (39). An exciting experimental prospect is the implementation of autonomous molecular evolution in a thermal trap—a molecular Darwinian process with replication driven by thermal cycling and selection driven by the length-sensitive trapping.

Materials and Methods

The trapping geometry and laser heating were described previously (16). Trap length was increased to 3.5 mm on each side (aspect ratio of the trap 70 from each side) at a lower temperature difference by plan correcting the scanning optics (specifications provided in *SI Text B*). A capillary with a rectangular cross section of 100 × 50 μm was thermally coupled to a Peltier element with sapphire and silicon. Double-stranded DNA with a length of 95 bp and with sticky ends 25 bases in length was allowed to reversibly polymerize by hybridization. Physiological salt concentrations (1× PBS: 137 mM NaCl, 2.7 mM KCl, 10 mM $Na_2HPO_4 \cdot H_2O$, 2 mM KH_2PO_4, pH 7.4) were used throughout the experiment. Heating and thermoviscous flow were provided by a 1,940-nm IR laser (20 W; IPG Photonics) and calibrated with the temperature-dependent fluorescence of the FRET signal and silica beads, respectively. DNA binding was recorded with fluorescence energy transfer (Table S1 and S2) (40) in an alternative dual excitation and permanent dual emission (Optosplit II; Cairn Research) microscopy setup (Axiotech Vario; Zeiss) with a 40×, 0.9 NA objective (Zeiss). Multiple images at modulated LED currents were used to enhance the dynamic range of the 12-bit CCD camera (PCO imaging). The thermophoretic properties (diffusion and Soret coefficient) of the 95-bp DNA were measured as described previously (20). To extrapolate the experiments into an RNA-world scenario, short single-stranded RNAs with lengths of 5–50 bases were measured over various salt concentrations and temperatures (*SI Text C*). Soret coefficients vs. RNA over length were fitted with power laws for use in theory and finite-element simulations.

ACKNOWLEDGMENTS. We thank Mario Herzog for measuring the thermophoretic properties of short nucleotides. Michael Nash, David Smith, Moritz Kreysing, and Ernesto di Mauro gave valuable comments on the manuscript at various stages. We thank Ingo Stein and Philip Tinnefeld in the analysis of FRET efficiencies. Financial support from the NanoSystems Initiative Munich, the Ludwig-Maximilians-Universität Munich Initiative Functional Nanosystems, the International Doctorate Program NanoBioTechnology, and the European Research Council Starting Grant is acknowledged.

1. Crick F (1970) Central dogma of molecular biology. *Nature* 227(5258):561–563.
2. Gilbert W (1986) Origin of life: The RNA world. *Nature* 319:618.
3. Wochner A, Attwater J, Coulson A, Holliger P (2011) Ribozyme-catalyzed transcription of an active ribozyme. *Science* 332(6026):209–212.
4. Zhang N, Zhang S, Szostak JW (2012) Activated ribonucleotides undergo a sugar pucker switch upon binding to a single-stranded RNA template. *J Am Chem Soc* 134(8):3691–3694.
5. Costanzo G, Pino S, Ciciriello F, Di Mauro E (2009) Generation of long RNA chains in water. *J Biol Chem* 284(48):33206–33216.
6. Costanzo G, et al. (2012) Generation of RNA molecules by a base-catalysed click-like reaction. *ChemBioChem* 13(7):999–1008.
7. Ferris JP, Hill AR, Jr., Liu R, Orgel LE (1996) Synthesis of long prebiotic oligomers on mineral surfaces. *Nature* 381(6577):59–61.
8. Baaske P, et al. (2007) Extreme accumulation of nucleotides in simulated hydrothermal pore systems. *Proc Natl Acad Sci USA* 104(22):9346–9351.
9. Mielke RE, et al. (2011) Iron-sulfide-bearing chimneys as potential catalytic energy traps at life's emergence. *Astrobiology* 11(10):933–950.
10. Martin W, Baross J, Kelley D, Russell MJ (2008) Hydrothermal vents and the origin of life. *Nat Rev Microbiol* 6(11):805–814.
11. Morgan L, et al. (2003) Exploration and discovery in Yellowstone Lake: Results from high-resolution sonar imaging, seismic reflection profiling, and submersible studies. *J Volcanol Geotherm Res* 122:221–242.
12. Weinert FM, Braun D (2009) An optical conveyor for molecules. *Nano Lett* 9(12): 4264–4267.
13. Braun D, Libchaber A (2002) Trapping of DNA by thermophoretic depletion and convection. *Phys Rev Lett* 89(18):188103.
14. Budin I, Bruckner RJ, Szostak JW (2009) Formation of protocell-like vesicles in a thermal diffusion column. *J Am Chem Soc* 131(28):9628–9629.
15. Braun D, Goddard NL, Libchaber A (2003) Exponential DNA replication by laminar convection. *Phys Rev Lett* 91(15):158103.
16. Mast CB, Braun D (2010) Thermal trap for DNA replication. *Phys Rev Lett* 104(18):188102.
17. Krammer H, Möller FM, Braun D (2012) Thermal, autonomous replicator made from transfer RNA. *Phys Rev Lett* 108(23):238104.
18. Duhr S, Braun D (2006) Why molecules move along a temperature gradient. *Proc Natl Acad Sci USA* 103(52):19678–19682.
19. Dhont JKG, Wiegand S, Duhr S, Braun D (2007) Thermodiffusion of charged colloids: Single-particle diffusion. *Langmuir* 23(4):1674–1683.
20. Reineck P, Wienken CJ, Braun D (2010) Thermophoresis of single stranded DNA. *Electrophoresis* 31(2):279–286.
21. Ludwig C (1856) Diffusion zwischen ungleich erwärmten Orten gleich zusammengesetzter Lösungen [Diffusion of homogeneous fluids between regions of different temperature]. *Sitzungsbericht Kaiser Akad Wiss*, ed Braunmüller W (Mathem-Naturwiss Cl, Vienna), Vol 65, p 539. German.
22. Clusius K, Dickel G (1938) Neues verfahren zur gasentmischung und isotopentrennung [A new method for the separation of different gases and isotopes]. *Naturwissenschaften* 26:546. German.
23. Debye P (1939) Zur theorie des clusiusschen trennungsverfahrens [Theory about the Clusius separation process]. *Ann Phys* 428:284–294. German.
24. Krapivsky PL, Redner S, Ben-Naim E (2010) *A Kinetic View of Statistical Physics* (Cambridge Univ Press, Cambridge, UK).
25. van Kampen NG (1992) *Stochastic Processes in Physics and Chemistry* (North-Holland Personal Library, Amsterdam).
26. Wang Z, Kriegs H, Wiegand S (2012) Thermal diffusion of nucleotides. *J Phys Chem B* 116(25):7463–7469.
27. Weinert FM, Braun D (2008) Optically driven fluid flow along arbitrary microscale patterns using thermoviscous expansion. *J Appl Phys* 104:104701-1–104701-10.
28. Duhr S, Braun D (2006) Optothermal molecule trapping by opposing fluid flow with thermophoretic drift. *Phys Rev Lett* 97(3):038103.
29. Seidel SAI, et al. (2012) Label-free microscale thermophoresis discriminates sites and affinity of protein-ligand binding. *Angew Chem Int Ed Engl* 51(42):10656–10659.
30. Wang X, et al. (2011) Peptide surfactants for cell-free production of functional G protein-coupled receptors. *Proc Natl Acad Sci USA* 108(22):9049–9054.
31. Saladino R, Botta G, Pino S, Costanzo G, Di Mauro E (2012) Genetics first or metabolism first? The formamide clue. *Chem Soc Rev* 41(16):5526–5565.
32. Spiegelman S, Haruna I, Holland IB, Beaudreau G, Mills D (1965) The synthesis of a self-propagating and infectious nucleic acid with a purified enzyme. *Proc Natl Acad Sci USA* 54(3):919–927.
33. Schulman R, Yurke B, Winfree E (2012) Robust self-replication of combinatorial information via crystal growth and scission. *Proc Natl Acad Sci USA* 109(17):6405–6410.
34. Lincoln TA, Joyce GF (2009) Self-sustained replication of an RNA enzyme. *Science* 323 (5918):1229–1232.
35. Lubrich D, Green SJ, Turberfield AJ (2009) Kinetically controlled self-assembly of DNA oligomers. *J Am Chem Soc* 131(7):2422–2423.
36. McKee ML, et al. (2010) Multistep DNA-templated reactions for the synthesis of functional sequence controlled oligomers. *Angew Chem Int Ed Engl* 49(43):7948–7951.
37. Turk RM, Chumachenko NV, Yarus M (2010) Multiple translational products from a five-nucleotide ribozyme. *Proc Natl Acad Sci USA* 107(10):4585–4589.
38. Obermayer B, Krammer H, Braun D, Gerland U (2011) Emergence of information transmission in a prebiotic RNA reactor. *Phys Rev Lett* 107(1):018101.
39. Andrieux D, Gaspard P (2008) Nonequilibrium generation of information in copolymerization processes. *Proc Natl Acad Sci USA* 105(28):9516–9521.
40. Förster T (1948) Zwischenmolekulare Energiewanderung und Fluoreszenz [Intermolecular energy transfer and fluorescence]. *Ann Phys* 437:55–75. German.

Supporting Information

Mast et al. 10.1073/pnas.1303222110

SI Text A. Theory

Equilibrium Solution of the Polymer Length Distribution. In this section, we describe the derivation and limitations of the solution of the aggregation–fragmentation model outlined in the main text. The aggregation–fragmentation type Eq. **2** rewritten more compactly as

$$\frac{dc_n}{dt}=\frac{1}{2}\sum_{i,j}\left[k_{ij}^{\mathrm{on}}c_ic_j-k_{ij}^{\mathrm{off}}c_{i+j}\right]\left[\delta_{i+j,n}-\delta_{i,n}-\delta_{j,n}\right] \qquad \textbf{[S1]}$$

(using the Kronecker-Delta, $\delta_{i,j}=0$ for $i\neq j$ whereas $\delta_{i,i}=1$) has a very simple stationary solution if there is a set of concentration values c_i that makes the first bracket in the sum vanish for every i, j. This condition is equivalent to the condition of detailed balance, i.e., the balance of all fluxes with their respective counterfluxes, $k_{ij}^{on}c_ic_j=k_{ij}^{off}c_{i+j}\ \ \forall i,j$. Such a set of concentration values c_i does not always exist, i.e., not for any set of rates k_{ij}^{on} and k_{ij}^{off}, but only if these rate constants satisfy certain constraints (one way to formulate and check these constraints is the Kolmogorov criterion, which demands that for every loop in state space, the product of all forward rates must be equal to the product of all backward rates). A physical system whose dynamics are described by a set of rate constants with this property is said to obey detailed balance. Detailed balance is guaranteed for a closed system that has reached full equilibrium, but not for nonequilibrium systems such as the thermal trap. However, for our description of the experiment in the main text, we assume an adiabatic accumulation limit where the thermal disequilibrium generated by the external temperature gradient does not destroy detailed balance in the chemical reactions. In this limit, the nonequilibrium steady state of the (reversible) polymerization process in the thermal trap corresponds to the equilibrium state of the same chemical process at an elevated total monomer concentration. This assumption is physically plausible and justified a posteriori by our finding that it yields an accurate description of the experiment.

To determine a set of rate constants k_{ij}^{on} and k_{ij}^{off} that is consistent with our independent measurements (diffusion constants and monomer–monomer binding equilibrium) and also obeys detailed balance, we posit that each bond breaks with equal probability and thus all dissociation rates are equal, $k_{ij}^{off}=\mathrm{const}$. Because we are ultimately interested only in the steady-state concentrations, c_n, the numerical value of this constant does not affect the final result (it cancels out) and need not be specified. The measured monomer–monomer dissociation constant, $K_D=k_{11}^{off}/k_{11}^{on}=1.14\times10^{-6}$ M, then fixes the monomer–monomer association rate. Assuming that the association is diffusion limited, our experimentally determined scaling of the diffusion coefficient with oligomer length, $D(n)=643n^{-0.46}\ \mu\mathrm{m}^2/\mathrm{s}$, can be used to extrapolate the monomer–monomer association rate to reactions with longer molecules. Specifically, we use this scaling to estimate the rates for monomer binding to a multimer according to $k_{1n}^{on}\propto[D(1)+D(n)]$, because the diffusion coefficient of the relative coordinate is the sum of the diffusion coefficients of the two molecules in a binary reaction. All remaining rates are then fixed by the detailed balance condition, because every multimerization state can be reached by consecutively adding monomers, and detailed balance requires that the product of equilibrium constants be the same along all pathways to a given multimerization state. The concentration of n-mers is then simply related to the free monomer concentration c_1 by $c_n=c_1^n\prod k_{1j}^{on}/k_{1j}^{off}$.

For our extrapolation of the prebiotic scenario for RNA polymerization, we use the same framework, but assume activation-controlled bond formation, with an association rate that is independent of the molecule lengths, $k_{nm}^{on}=\mathrm{const}$. Taking the dissociation rate to be constant as well (as before), the distribution of polymer lengths becomes exponential, $c_n=c_1^n(k^{on}/k^{off})^{n-1}$. This choice of rates automatically fulfills detailed balance. As detailed below, we chose K_D to be averaged over temperature and temperature independent, because it deviates less than one order of magnitude within the considered temperatures perpendicular to the trap (Eq. **S13**) and the temperature does not vary along the trap.

Estimating the Concentration of Long Polynucleotides in Equilibrium. Although the detailed chemical pathway under which polynucleotides could have been formed from individual building blocks is still under debate, one can point out the regime in which long polynucleotides are expected. Although covalent bonds formed between nucleotides are relatively stable, the possibility for cleavage due to hydrolysis increases with each newly added nucleotide. The competition between formation and cleavage leads to an equilibrium distribution of finite polynucleotide lengths. Assuming random association and dissociation, we use the aggregation–fragmentation Eq. **2**. For an activation-controlled reaction, see the discussion following Eq. **2**, where the concentration of polynucleotides decays exponentially with length $c_n=c_1(c_1/K_D)^{n-1}$. The total concentration of nucleotides $c_0=\sum nc_n$ can be expressed in terms of monomer concentration c_1 and dissociation constant K_D. The functional dependence can be inverted analytically to

$$c_1(c_0,K_D)=1+\frac{K_D}{2c_0}-\frac{\sqrt{(K_D(K_D+4c_0))}}{2c_0}. \qquad \textbf{[S2]}$$

The concentration distribution c_n as a function of the polymerization strength c_0/K_D is shown in Fig. S1. For concentrations lower than the dissociation constant, almost only monomers exist in equilibrium. Long polynucleotides are virtually nonexistent in this regime. For instance, 200-mers are expected to appear as little as $\sim c_0\times10^{-600}$. Long polynucleotides appear abruptly as soon as the concentration exceeds the dissociation constant by orders of magnitude.

Derivation of Accumulation Formulas. *a) Gravitationally driven trap.* Debye's approach for the thermophoretic trap was used to derive an analytic result for the accumulation distribution inside the trap. This derivation is now laid out in detail for both laser and gravitationally induced pumping. As explained in the main text, the pore is modeled by an elongated 2D compartment orientated in a vertical y direction. A temperature gradient is applied in a horizontal x direction, by keeping the two walls facing each other at a constant temperature, one being warm and the other one cold. The 2D approximation of the simulation and theory was shown to successfully describe the 3D experiment and theoretical treatments in previous work (1, 2). This is reasonable because flow velocities in the z direction are much smaller than the convection flow along the y axis induced by gravitation or, in the experiment, by a moving laser spot. For thermophoresis, only the component along the thermal gradient (here, along the x axis) to the convection flow will contribute to the strong accumulation of the thermal trap. Minor thermal gradients, created by the glass surfaces of the capillary, give a much smaller thermophoretic movement along the z and y axes, both contributions that can be neglected. Likewise, diffusion was

shown to average well over existing parabolic flow profiles in three dimensions. As discussed and treated in ref. 1, a variety of chambers with different z dimensions showed equal accumulation strengths. Thus, to describe the experiment, it is sufficient to consider the measured experimental data (temperature, fluid flow profile) only in two dimensions. Please note that all measurements are averaged along the z axis by the epifluorescent measurement. The drift-diffusion equation

$$\frac{\partial c}{\partial t} = D\left(\frac{\partial^2 c}{\partial x^2} + \frac{\partial^2 c}{\partial y^2}\right) + S_T D \frac{dT}{dx}\frac{\partial c}{\partial x} + v(x)\frac{\partial c}{\partial y} \qquad \textbf{[S3]}$$

is steered by three contributions: diffusion, thermodiffusion, and convection. Sedimentation of DNA or RNA is not considered here, because even for large T4-DNA with a length of 169 kbp and a sedimentation coefficient $s \sim 100$ S, the sedimentation speed $v_{sed} = g \cdot s = 0.1$ nm/s at gravitational acceleration g is >10,000-fold slower than convection and can be neglected (3, 4). The following two effects are directly evoked by a linear temperature gradient $dT/dx = \Delta T/w$ over the width w of the compartment. On the one hand the gradient yields a thermodiffusive flux in the x direction with D and S_T being the diffusion and Soret coefficient of the dissolved molecule. On the other hand, particles are transported via convection. The driving effect for convection in a horizontally erected, elongated pore is the expansivity β of the solvent. Difference in density yields differences in gravitational force per volume. Debye derived from the equilibrium of forces for a volume element a dependence of the velocity in the y direction on the x position:

$$\frac{\partial^3 v}{\partial x^3} = \frac{-\beta g \rho \Delta T}{\eta w}. \qquad \textbf{[S4]}$$

This factor depends on the natural constants solvent density ρ, viscosity η, and thermal expansivity β, as well as width w and temperature difference ΔT, and holds as long as temperature-induced changes in expansivity can be neglected. Far from the ends of the trap, the flow is solely directed in the y direction, thus meaning that the velocity profile in the x direction is independent of y. In this case, the velocity profile can be solved via integration. With no slip boundaries at both walls, $v(0) = 0$, $v(w) = 0$. As a side condition, because no drift through the pore is assumed, the total flow up and down must cancel for the system to conserve mass. This yields the velocity profile (Fig. S2*D*)

$$v(x) = \frac{-\beta g \rho \Delta T w}{6\eta}\left(\frac{1}{2}\frac{x}{w} - \frac{3}{2}\frac{x^2}{w^2} + \frac{x^3}{w^3}\right) = -v_0\left(\frac{1}{2}\frac{x}{w} - \frac{3}{2}\frac{x^2}{w^2} + \frac{x^3}{w^3}\right), \qquad \textbf{[S5a]}$$

as used in the main text.

To simplify analyzing the accumulation behavior, Eq. **S3** is nondimensionalized. Introducing the dimensionless constants $\tau = Dt/w^2$, $q = v_0 w/D$, $p = S_T \Delta T$, $\eta = y/w$, $\xi = x/w$, Eq. **S3** is transformed to

$$\frac{\partial c}{\partial \tau} = \left(\frac{\partial^2 c}{\partial \xi^2} + \frac{\partial^2 c}{\partial \eta^2}\right) + p\frac{\partial c}{\partial \xi} + qf(\xi)\frac{\partial c}{\partial \eta} \qquad \textbf{[S6]}$$

with $f(\xi)$ being $f(\xi) = (1/2\xi - 3/2\xi^2 + \xi^3)$.

For the purpose presented in the main text, the steady-state distribution of concentration is of interest; i.e., $\partial c/\partial \tau = 0$. The key to solving Eq. **S6** in the steady state is a separation of variables. We choose $c(\xi, \eta) = U(\xi)V(\eta)$ with an exponential dependence in the long η axis $V(\eta) = \exp(\alpha\eta)$, where the factor α is to be determined. Plugging the ansatz into Eq. **S6** yields a differential equation for $U(\xi)$:

$$U'' + pU' + \left(\alpha^2 + \alpha q f(\xi)\right)U = 0. \qquad \textbf{[S7]}$$

The natural boundary conditions enforce that no flux of particles is crossing the walls of the compartment; hence diffusive and thermodiffusive currents have to cancel at the boundary. In terms of $U(\xi)$ this means $U' + pU = 0$ at $\xi = 0, 1$. Eq. **S7** can only simultaneously obey both boundary conditions for a distinct α, hence defining the exponential accumulation. Solving Eq. **S7** can be done numerically by standard computational techniques.

In contrast, one can compute an analytic solution in the limit $p << 1$, which is presented in the following. We expand U and α to second order in p and get $U = 1 + pU_1 + p^2U_2 + ...$, and $\alpha = p\alpha_1 + p^2\alpha_2 + ...$ To get a uniform distribution for $p = 0$, we choose the zeroth order of U arbitrarily to be unity and that of α to be zero. Inserting the expansions into Eq. **S7** and collecting orders of p gives

$$p^1 : \; U_1'' + \alpha_1 q f(\xi) = 0 \qquad \textbf{[S8a]}$$

$$p^2 : \; U_2'' + U_1' + \alpha_1^2 + \alpha_2 q f(\xi) + \alpha_1 q f(\xi) U_1 = 0. \qquad \textbf{[S8b]}$$

The second-order differential Eq. **S8a** can be solved by direct integration, while enforcing the boundary conditions of first order in p, $U_1' + 1 = 0$ at $\xi = 0, 1$. Subsequently, the result is inserted into Eq. **S8b**, which can once again be solved by direct integration. Enforcing the boundary conditions of second order in p, $U_2' + U_2 = 0$ at $\xi = 0, 1$, fixes the exponent $\alpha \approx p\alpha_1$. For gravitational pumping the exponent is $\alpha \approx 84pq/(10,080 + q^2)$ and the distribution inside the trap (Fig. S2*E*) is

$$c(\xi, \eta) = \left(1 + p\left(-\xi + \frac{84pq}{10,080 + q^2}\left(\frac{1}{20}\xi^5 - \frac{1}{8}\xi^4 + \frac{1}{12}\xi^3\right)\right)\right) \times \exp\left(\frac{84pq}{10,080 + q^2}\eta\right). \qquad \textbf{[S9a]}$$

The exponential accumulation is maximal for an optimal $q_{opt} = \sqrt{(10,080)} \approx 100$, where the exponent has its maximum, $\alpha_{max} \approx 0.42p$. Because velocity is coupled to the width of the trap, optimal $q_{\mathrm{opt}} = v_0 w/D$ means optimal width.

The choice of width and thus convection speed is crucial for the accumulation behavior. Diffusion decreases with RNA/DNA length, and thus the optimal width decreases as well. If the width is chosen such that monomers are accumulated optimally, then the buildup of longer polymers will decrease the accumulation efficiency. If, on the other hand, the width is chosen to optimally accumulate long polymers, then polymerization escalates inside the trap.

b) Laser-driven trap. A laser can be used to evoke a thermal molecule trap (Fig. 3) analogously to the gravitational thermal molecule trap discussed above. The advantage is that several parameters of the system, such as convection velocity, temperature gradient, and width of the trap, can be modified independently. Also a symmetrical trap can be generated to not depend on the geometry of a hard-to-define trap ending. Solvent flux and temperature gradient are directly evoked by an IR laser moving along the center line of a glass capillary. Due to the expansivity of water, the solvent flows in the opposite direction of the laser movement. At the edges of the linear IR laser pathway the solvent naturally reverses and flows back along the outside edge of the capillary, creating two symmetric convection rolls along the long axis. This setup would accumulate molecules at one corner, where they could easily escape via diffusion. To prevent this from happening the capillary could be either closed physically, like the gravitationally driven thermal molecule

trap, or closed using mirror-inverted pumping along the short axis of the trap. This induces four symmetric convection rolls, each of them trapping analogous to the gravitationally driven trap (Fig. S2*A–C*). In the following we calculate the accumulation for one these four identical traps. The a velocity pattern is symmetric to the center line of the trap, having the global velocity maximum in the center and velocity maxima of opposite sign close to the edges of the trap. The profile is modeled analogous to Eq. **S5a**, by assuming that the third spatial derivative of the velocity is constant, $\partial^3 v/\partial x^3 = \text{const}$. The result was qualitatively verified using bead tracking. Furthermore, slip-flow boundaries are enforced; i.e., $v(0) = 0$, $v(w) = v_0$. The choice of coordinates is such that the origin of x is at one cold wall and $x = w$ in the center of the trap. As side conditions we demand the profile to be continuous, i.e., $\partial v/\partial x = 0$ at $x = w$, and a drift-free trap. This yields the velocity profile (Fig. S2*D*)

$$v(x) = v_0\left(6\frac{x}{w} - 15\frac{x^2}{w^2} + 8\frac{x^3}{w^3}\right) \qquad \textbf{[S5b]}$$

To simplify the analysis of the accumulation behavior, Eq. **S3** is nondimensionalized. Identically to gravitational pumping, the dimensionless constants $\tau = Dt/w^2$, $q = v_0 w/D$, $p = S_T\Delta T$, $\eta = y/w$, $\xi = x/a$ are introduced. The pumping velocity v_0 can be adjusted by laser movement. The velocity profile $f(\xi) = (6\xi - 15\xi^2 + 8\xi^3)$ leads to an accumulation exponent $\alpha \approx 189pq/1,260 + 38q^2$ and the distribution in the side trap (Fig. S2*E*)

$$c(\xi,\eta) = \left(1 + p\left(-\xi + \frac{189pq}{1,260+38q^2}\left(\frac{2}{5}\xi^5 - \frac{3}{4}\xi^4 + \frac{1}{2}\xi^3\right)\right)\right) \times \exp\left(\frac{189pq}{1,260+38q^2}\eta\right). \qquad \textbf{[S9b]}$$

Here, the exponent has its maximum $\alpha_{max} \approx 0.43p$ at an optimal $q_{opt} = \sqrt{630/19} \approx 5.8$. A 2D finite-element simulation was used to describe the experimental laser trap, where a laminar fluid drift through the capillary allowed for reasonable experimental timescales. The assumption that a 2D simulation may describe the 3D experiment is valid in this regard because the prominent driving force of convection and thermophoresis, the varying temperature profile, is y symmetric and has only small deviations along the z axis. The 2D/3D difference of the convection flow is small for the fast thermoviscous pumping used in the experiment as shown in ref. 2. Therefore, the match of the simulation and the 2D projection of the experiment obtained by fluorescence microscopy is reasonable (Figs. 3 and 4).

Quasi-1D Calculation of the Accumulation. In the following, an approximate solution of the accumulation inside the trap for fast chemical reactions is derived. In this limit, the polymerization reaction equilibrates adiabatically to the steady-state solution $c_n = c_1^n \prod k_{1x}^{on}/k_{1x}^{off}$ during the accumulation of the thermal trap. For this reason we define effective constants of the system, such as the diffusion coefficient

$$\overline{D} = \frac{\sum c_n n D(n)}{\sum c_n n}$$

and Soret coefficients

$$\overline{S}_T = \frac{\sum c_n n S_T(n)}{\sum c_n n},$$

which account for the combined effects of the individual polymers. The diffusion and Soret coefficients for double-stranded (ds)DNA used in the main text and for dsDNA in the experimental conditions in Figs. 3 and 4 are $D(n) = 65n^{-0.75}$ μm^2/s and $S_T(n) = 0.1n^{0.5}$ K^{-1}. In the warm and salty scenario for RNA shown in Fig. 2, the experimental scaling laws $D(n) = 643n^{-0.46}$ μm^2/s and $S_T(n) = (5.3 + 5.7n^{0.73}) \times 10^{-3}$ K^{-1} were used (5). The largest change in diffusion and Soret coefficients is the exponential accumulation along the long axis of the trap, because this alters the length distribution c_n toward longer molecules. Furthermore the influence of concentration variation along the short axis and the concentration distribution change due to the temperature-dependent dissociation constant are two minor, temperature-dependent contributions. Assuming that the temperature difference ΔT is small, one can neglect both latter contributions. Although assuming a small concentration variation along the short axis is almost always justified, here variations are only of order $p = S_T\Delta T$, and the second assumption may cause inaccuracies due to the exponential impact of temperature differences on the dissociation constant for too large ΔT. Following the simplification, the dependence of diffusion and Soret coefficients, D and S_T, becomes effectively one-dimensional, along the y axis. Thus, the system can be sliced along y into infinitesimal disks of constant D and S_T and solved in an integrative manner:

$$c(x,y) = U(x, c(x,y))\exp\left(\int_0^y d\tilde{y}\alpha\left(c\left(x,\tilde{y}\right)\right)\right). \qquad \textbf{[S10]}$$

As a top boundary condition we use the solution of Eq. **S3** and use c_{Out} as concentration. U and α can be obtained either numerically or analytically, as described above.

SI Text B. Experiment

Materials and Methods. We use a custom-made borosilicate capillary (VitroCom) with a rectangular cross section of 100 × 50 μm. The capillary is embedded into immersion oil to improve the optical quality of the system and sandwiched between an IR-transparent silicon wafer and a sapphire coverslip to enhance thermal gradients. The silicon wafer is cooled with Peltier elements (9502/065/018M; Ferrotec) at 10 °C to ensure constant temperature for long time measurements. The temperatures inside the capillary are set to $T_{min} = 53$ °C and $T_{max} = 60$ °C over a range of 50 μm by IR laser absorption.

The filled capillary is connected to a high-precision syringe pump (neMESYS; Cetoni) on one side for automatic refilling. Imaging is done with a fluorescence microscope (Axiotech Vario; Zeiss), using a set of high-power light-emitting diodes (LEDs) for alternating color excitation (590 nm and 470 nm; Thorlabs) and a 40× objective (Plan-Neufluar 40× 0.9 NA; Zeiss). A CCD camera (Sensicam; PCO) records color-separated fluorescence resonance energy transfer (FRET) images provided by a dual-view unit (Optosplit II; Cairn Research). Because the molecule trap creates DNA concentration differences of several orders of magnitude, each excitation channel (blue, amber) was recorded with three different LED settings (10 mA, 20 mA, and 80 mA) to improve the signal's dynamic range. With dual excitation and dual emission, six CCD frames and 12 images were recorded at each time frame. FRET probability was calibrated as described below.

Heating and thermoviscous flow are provided by an IR laser (TLR-20-1940; IPG Photonics) from the bottom. It is focused inside the capillary with a custom-built scanner lens system providing a constant heat-spot width of 30 μm along the whole-scan range of 2 × 3.5 mm. The scanner lens system consists of three lenses (L_A, Linos, G063095000, f = 15 mm; $L_B = L_C$, Thorlabs, LA1422-C, f = 40 mm) with lens separations of $\Delta x_{L_A,L_B} = 57$ mm, $\Delta x_{L_B,L_C} = 45$ mm, and $\Delta x_{L_C,scanner} = 10$ mm. Angular deflection is realized by scanning mirrors (6200-XY; Cambridge Technology). A heat bath (F12; Julabo) cools the microscopy stage and the scanning mirrors. The thermoviscous fluid flow is created by a di-

rected/asymmetric movement of the IR laser along the capillary: Each time the laser spot passes by, a small amount of water is transported opposite to the direction of the laser spot movement (6).

To realize a reversible and observable polymerization reaction, we designed pieces of double-stranded DNA (95 bp) that define a monomer (Fig. 3*A*) with two complementary sticky ends of 25 bases (IBA Lifesciences). The sequences of the monomer are

DNA_A: 3′ TGTGAGACCCCCGGGTCACTGATGAGGAGGAGCTGCGGACTCCCGTGAACCAGAACTCTCGGGGAATCCATCAACTTGGCCGGTAAGGGGTCCCGCAATAACGTG(ROX)ACGTACATCGGGACT 5′

DNA_B: 5′ GTTATTGCAC(FAM)TGCATGTAGCCCTGAACACTCTGGGGGCCCAGTGACTACTCCTCCTCGACGCCTGAGGGCACTTGGTCTTGAGAGCCCCTTAGGTAGTTGAACCGGCCATTCCCCAGGGC 3′.

DNA arrived as an aqueous solution with a concentration of 100 μM and was portioned into aliquots of 50 μL and frozen immediately. The final concentrations of the working stock are 10 μM of DNA_A and DNA_B, respectively, inside a 1× PBS buffer (137 mM NaCl, 2.7 mM KCl, 10 mM $Na_2HPO_4 \cdot H_2O$, 2 mM KH_2PO_4). The stock solution was annealed into a defined state before further dilution, using a temperature ramp from 95 °C to 10 °C with a cooling rate of 1 °C/10 s.

Each sticky end was modified with the fluorescent dye carboxy-X-rhodamin (ROX) or its respective FRET counterpart fluorescein amidite (FAM). The polymerization of two monomers at their complementary sticky ends brings both dyes in close proximity and is recorded by fluorescence resonance energy transfer.

Because we used FRET in a bulk solution at various temperatures, prior calibration had to be done. We recorded the temperature dependence of the spatially averaged FRET signal obtained by

$$FRET(T) \equiv \frac{DA(T) - dd(T) * DD(t) - aa(T) * AA(T)}{AA(T)}, \quad \textbf{[S11]}$$

where the channels are defined according to Tables S1 and S2.

The temperature-dependent crosstalk corrections $dd(T)$ and $aa(T)$ were recorded over a temperature range of 10–95 °C, using the same monomers with nonsticky ends to prevent binding artifacts in the fluorescence signal. For measurements of $dd(T)$ ($aa(T)$), the monomers were labeled with 6-FAM (6-ROX) only. After obtaining coefficients $\alpha \equiv min(FRET(T))$ and $\beta \equiv \max(FRET(T)) - \alpha$ by Eq. **S11**, the normalized, crosstalk-corrected, and time-dependent FRET ratio for each pixel (x,y) and frame t is defined as

$$FRET(t,x,y) \equiv \left(\frac{DA(t,x,y) - dd(T(x,y)) * DD(t,x,y) - aa(T(x,y)) * AA(t,x,y)}{AA(t,x,y)} - \alpha \right) \Big/ \beta, \quad \textbf{[S12]}$$

where $T(x,y)$ is the previously measured temperature profile inside the trap. This procedure was repeated for each illumination setting.

To determine the 2D temperature profile $T(x,y)$ inside the filled capillary, we switched off the thermoviscous fluid flow but left the temperature profile of the molecule trap unchanged before each trapping measurement: Superposition of the initial movement with a reversed movement of the IR laser spot results in a vanishing net flow inside the capillary while IR absorption is kept constant. We compared the steady-state FRET signal under these conditions with the temperature-dependent FRET calibration measurement done before using thermoelectric elements. Fluid flow velocity was recorded by tracking homogeneously distributed 1-μm green fluorescent silica particles (PSI-G1.0NH2; Kisker), using the same experimental settings as in the polymerization trap. The mean fluid speed was determined to be 28 ± 2 μm/s. The silica beads used in this measurement exhibit a considerably lower diffusion coefficient compared with DNA (5). Accordingly the beads are not trapped but continuously cycled between the hot and the cold sides of the compartment. Clay (7) with similar slow diffusion could therefore act as a catalyst for nucleotide-based reactions on the cold side, while their surface is being reset for another cycle at the hot side.

The only fitting parameter of the polymer theory, the dissociation constant $K_{D,polymer}$ of the monomer's hybridization bond, was checked independently with thermal melting-curve analysis (Fig. S3*A*) and calculated with $K_{D,melting} = FRET(T) / \left(2 \cdot c_0 (1 - FRET(T))^2\right)$ for a solution of 2 μM monomers buffered in 1× PBS (8). The dissociation constants revealed by both methods match within the error margin. The chosen temperature of $T = 56$ °C is the temperature at the point of measurement in the polymerization experiment (Fig. S3*A*). The measured, temperature-dependent dissociation constant was also taken into account for the finite-element simulation and mapped over the temperature profile. The free energy of the hybridization bond is estimated with a linear fit of the dissociation constant over the inverse absolute temperature with $\Delta G^0/R \cdot 1/T + \text{const.} = \ln(K_D)$. The obtained value of 45 kcal/mol matches the modeled value of 48 kcal/mol for the bond energy (determined using IDT OligoAnalyzer). An approximation for the relative change of K_D over temperature is

$$\frac{dK_D/dT}{K_D} = \frac{\Delta G^0}{R \cdot T^2}. \quad \textbf{[S13]}$$

Whereas the temperature-dependent and measured K_D was used in the finite-element simulation, K_D was assumed to be temperature averaged in the theoretical considerations. Eq. **S13** justifies this assumption for theoretical calculations concerning the experimental model system, because K_D varies less than one order of magnitude within the given temperature range. In the case of RNA polymerization, the theoretical results represent a lower bound for the escalated polymerization, because the affinity of polymerization is higher in colder regions of the trap, especially in the trapping center at the bottom edge.

The complexity of the experimental system does not allow a full analytical description, but is accessible with a combination of an analytical polymerization solution and a finite-element simulation of the thermal trap. Therefore, we combined the semianalytical polymerization theory with a 2D hydrodynamic finite-element simulation. Because the characteristic timescale of polymerization is much shorter compared with trapping dynamics, we may correlate all DNA length-dependent parameters (thermodiffusion/diffusion coefficients) of the system to the total concentration of monomers at a specific time and place, using $\overline{D}(c_0)$ and $\overline{S}_T(c_0)$ (main text). Convective and drift flow velocity, temperature-dependent K_D, and temperature profile were set to experimental values (Fig. 3*C*). The simulated capillary geometry includes a passive area without heating or thermoviscous pumping at the outer boundaries of the trap to fully model the experimental setup. The positions used for extracting experimental and

simulation data are the trapping center itself (center) and a relative distance of 4.9 mm from the trapping center (edge). Fig. S3*B* clarifies the two steady states of the accumulation ratio $\sum kc_{k,center} / \sum kc_{k,edge}$ and the absolute monomer concentration $\sum kc_{k,center}$ by showing the time evolution of the total amount of monomers integrated over the simulated trapping area.

SI Text C. Primordial Scenario

The model presented in the main text can in principle be extrapolated to any arbitrary primordial scenario, concerning temperature, salt concentration, or geological geometries. Here we discuss two additional plausible scenarios, a cold and saline scenario (e.g., an arctic ocean) and a salt-deprived scenario (e.g., a primordial freshwater pond). For this purpose we measured the parameters of the system, i.e., diffusion D and Soret coefficient S_T for different salt concentrations, DNA or RNA lengths, and temperatures as shown in Fig. S3 *C* and *D* for the two settings.

Whereas the former scenario is comparable to modern biological environments, the latter has been proposed by Szostak and colleagues as these conditions could facilitate development of protocells out of simple fatty acids (9) and could therefore be a link from early molecular evolution to the first compartmentalization of life on earth. The cold and salty ocean was modeled assuming 25 °C (which is cold compared with the typical 60 °C of primordial oceans) and a salt concentration of 150 mM NaCl ($\lambda_{Debye} = 0.8$ nm). The lower concentration slightly decreases the effect of thermophoresis, but can easily be compensated by a slightly longer trap length.

In freshwater, in contrast, the low salt concentrations enhance the effect of thermophoresis significantly and the hyperexponential escalation sets in at even shorter trap heights, as shown in Fig. S4, *II*. Here the temperature is assumed to be at 55 °C and salt concentration at 3 mM NaCl ($\lambda_{Debye} = 5.6$ nm). We restricted ourselves to investigating only geological boundary conditions, but not the chemical means of polymerization because our fully reversible polymerization model represents the most inefficient polymerization reaction and therefore gives a lower bound for polymer lengths. Stable covalent bonds, for example, are often modeled using irreversible polymerization, which would quickly lead to incorporation of all building blocks into very long polymers.

1. Baaske P, et al. (2007) Extreme accumulation of nucleotides in simulated hydrothermal pore systems. *Proc Natl Acad Sci USA* 104(22):9346–9351.
2. Mast CB, Braun D (2010) Thermal trap for DNA replication. *Phys Rev Lett* 104(18): 188102.
3. Miller ES, et al. (2003) Bacteriophage T4 genome. *Microbiol Mol Biol Rev* 67(1):86–156.
4. Rosenbloom J, Cox EC (1966) Sedimentation coefficient of T-even bacteriophage DNA. *Biopolymers* 4(7):747–757.
5. Duhr S, Braun D (2006) Why molecules move along a temperature gradient. *Proc Natl Acad Sci USA* 103(52):19678–19682.
6. Weinert FM, Braun D (2008) Optically driven fluid flow along arbitrary microscale patterns using thermoviscous expansion. *J Appl Phys* 104:104701-1–104701-10.
7. Ferris JP, Hill AR, Jr., Liu R, Orgel LE (1996) Synthesis of long prebiotic oligomers on mineral surfaces. *Nature* 381(6577):59–61.
8. Mergny J-L, Lacroix L (2003) Analysis of thermal melting curves. *Oligonucleotides* 13(6): 515–537.
9. Ricardo A, Szostak JW (2009) Origin of life on earth. *Sci Am* 301(3):54–61.

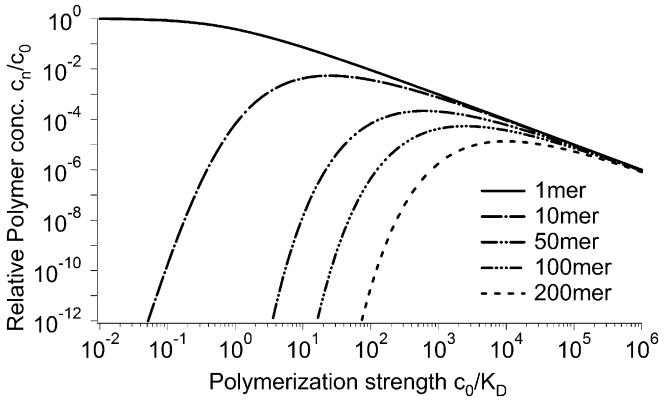

Fig. S1. Equilibrium distribution of polynucleotide lengths. Hydrolysis constantly cleaves polynucleotides, leading to finite lengths of polynucleotides in equilibrium. For total monomer concentrations $c_0 = \sum nc_n$ lower than the dissociation constant, virtually only monomers are present. For concentrations larger than the dissociation constant, a large share of polynucleotides is built up. 200-mers abruptly appear for $c_0/K_D > 10^2$.

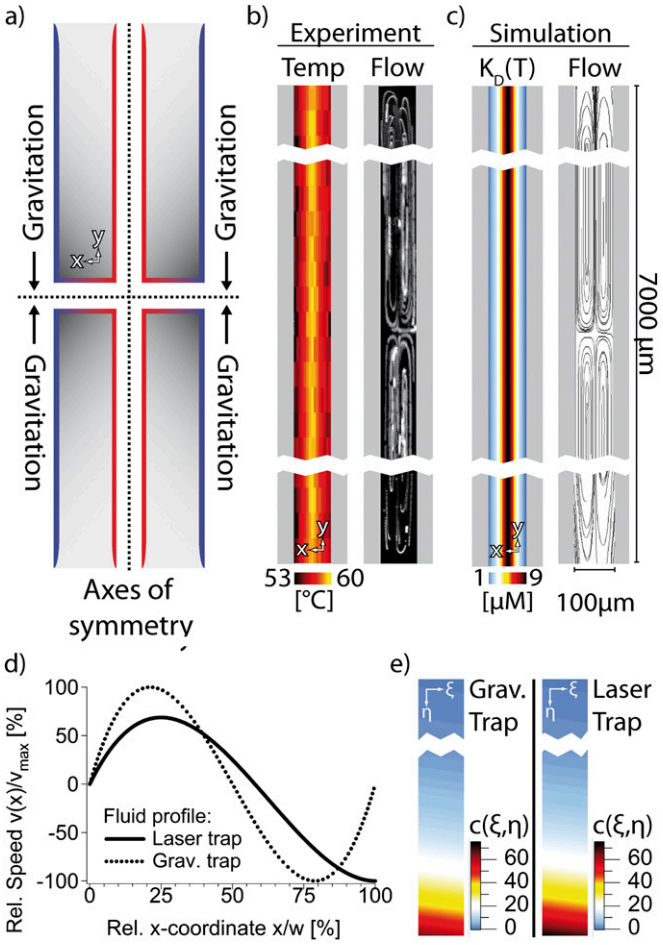

Fig. S2. Connection of theory, simulation, and experiment. (*A*) A gravitational trap is driven by a thermal gradient and the buoyancy of water. Therefore, it has a fixed relation between the diffusion coefficient of the species to be accumulated and the optimal width of the trap. In a laser-driven trap, the convection speed can be set independently of the temperature gradient, which allows having an optimal convection speed for any species of biomolecules in a given trap width. The geometry of the laser-driven trap can be thought of as four gravitational traps glued together at their hot and bottom sides with symmetric boundary conditions. (*B*) The 2D temperature and profile were measured using the temperature-dependent dye 2′,7′–bis–(2–carboxyethyl)–5–(and–6)–carboxyfluorescein and tracking fluorescent beads. (*C*) A 2D finite-element simulation simulates the experiment. We used the theoretical concentration-dependent diffusion coefficient $D(c)$ and Soret coefficient $S_T(c)$ to take into account the timescale-separated polymerization reaction. The temperature-dependent dissociation constant $K_D(T)$ was measured separately (Fig. S3) and was mapped to the temperature profile inside the trap. Therefore, all relevant experimental parameters [$K_D(T)$, temperature, convection flow, degree of polymerization, and monomer concentration] could be successfully modeled (Fig. 4). (*D*) Convection flow $v(x)$ according to Eq. **S5a** (gravitation trap: dashed line) and Eq. **S5b** (laser trap: solid line). The difference comes from the missing nonslip boundary in the center of the capillary; however, it has no significant effect on the trapping efficiency. (*E*) Concentration distribution $c(\xi,\eta)$ according to Eq. **S9a** (gravitation trap) and Eq. **S9b** (laser trap) for RNA nucleotides with $S_T = 0.01 \cdot 1/K$, $\Delta T = 10\ K$, $p = S_T \cdot \Delta T = 0.1$, $q_{grav,opt} = 100$ for the gravitation trap, $q_{laser,opt} = 5.8$ (*SI Text A and B*) for the laser trap, and an exemplary trap aspect ratio of 1:100.

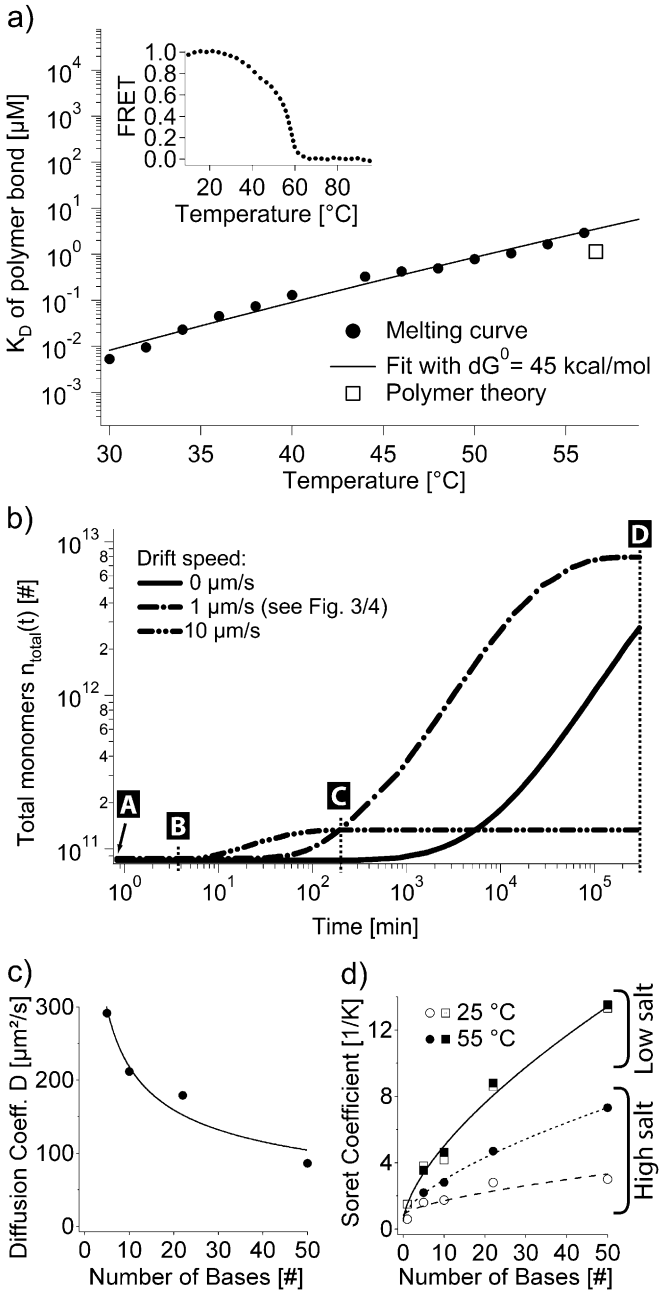

Fig. S3. (*A*) Dissociation constant for the polymer bond $K_{D,melting}$ is measured independently from the polymerization experiment via melting-curve analysis. It matches the dissociation constant $K_{D,polymer} = 1.14$ µM obtained by fitting of experimental data in Fig. 4*A* with the polymerization theory. Therefore, no fitting parameters are needed to theoretically describe the polymerization experiments. (*B*) Integration of the total monomer concentration over the complete simulated thermal trap $n_{total}(t) = \sum_k k \int_{V(\mathrm{Trap})} c_k dV$ for different drift speeds through the capillary. In the experimental section (Figs. 3 and 4) a drift speed of 1 µm/s was used: The trap needs 6 h to deplete its edge area by two orders of magnitude and therefore reach its steady state of the separation ratio $\sum k c_{k,center} / \sum k c_{k,edge} (t = 0..10^2$ min, timepoints A–C). Subsequently, a strong concentration gradient is built up at the edges of the trapping area, which leads to an diffusive influx of new monomers from the outside into the trap ($t = 10^2..10^5$ min, timepoints C and D) until the edge and bulk concentration of monomers match ($t > 10^5$ min). Higher drift speeds (10 µm/s) yield faster equilibration times of trapped polymerization but at a lower total accumulation of monomers. Without drift (0 µm/s), the trapped polymerization would have equilibrated only within several years. (*C* and *D*) Measurement of Soret and diffusion coefficients by microscale thermophoresis. Whereas the Soret coefficient is inferred by the local thermophoretic depletion of DNA or RNA, $c/c_0 = \exp(-S_T \cdot \Delta T)$ in a temperature difference ΔT, diffusion is obtained via fluorescence recovery after switching of the heat source. (*C*) Length-dependent diffusion coefficient D of DNA or RNA scales with $D(n) = 643 n^{-0.46}$ µm^2/s. (*D*) Length dependence of the Soret coefficient S_T for 25 °C and 55 °C under physiological, high-salt ($\lambda_{Debye} = 0.8$ nm, [NaCl] = 150 mM) and low-salt ($\lambda_{Debye} = 5.6$ nm, [NaCl] = 3 mM) conditions. For high salt at 55 °C S_T is fitted to $S_T(n) = (5.3 + 5.7 n^{0.73}) \times 10^{-3}$ K^{-1}.

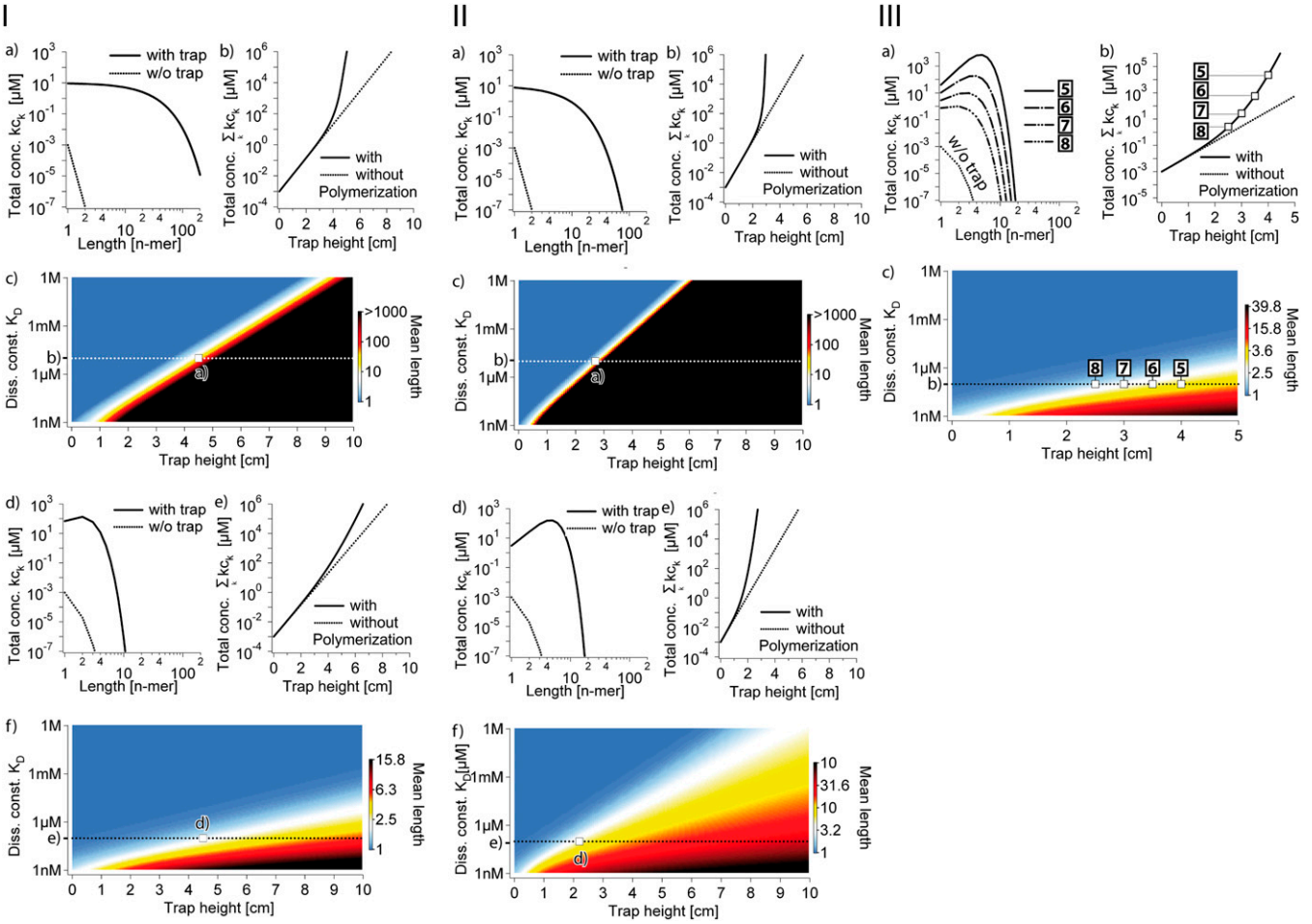

Fig. S4. (*I*) "Cold Earth": Accumulation inside a primordial geothermal pore surrounded by cold and salty water (25 °C, 150 mM KCl, $\lambda_{Debye} = 0.8$ nm), colder, but otherwise identical to Fig. 2 in the main text. (*A*) Length distribution of a fast-reacting polymer inside a 4.5-cm-long trap, with temperature difference 10 K and RNA dissociation constant $K_D = 10$ μM. The steady state is reached after 100 y and oligomers of the size of active ribozymes are predicted in the trap. (*B*) Escalation of trap efficiency for varying pore heights as soon as the concentration reaches K_D. (*C*) Mean polymer lengths for varying pore heights and dissociation constants. For every plausible K_D, there exists a trap height at which polymerization escalates. *D*–*F* extrapolate to the slow reaction limit, using the identical trap and $K_D = 0.1$ μM. The phenomenon persists, showing its robustness. (*II*) "Fresh Water": Accumulation inside a primordial geothermal pore surrounded by fresh water (55 °C, 3 mM KCl, $\lambda_{Debye} = 5.6$ nm) and with less salty conditions but otherwise identical to Fig. 2 in the main text. The temperature dependence is small (Fig. S3 *C* and *D*). (*A*) Length distribution of a fast-reacting polymer inside a 2.7-cm-long trap, with temperature difference 10 K and RNA dissociation constant $K_D = 10$ μM. The steady state is reached after 100 y and oligomers of the size of active ribozymes are predicted in the trap. (*B*) Escalation of trap efficiency for varying pore heights as soon as the concentration reaches K_D. (*C*) Mean polymer lengths for varying pore heights and dissociation constants. For every plausible K_D, there exists a trap height at which polymerization escalates. *D*–*F* extrapolate to the slow reaction limit, using the identical trap and $K_D = 0.1$ μM. The phenomenon persists, showing its robustness. (*III*) Very slow, reversible RNA polymerization: Accumulation and polymerization of RNA in a primordial geothermal fissure. (*A*) Length distribution of a slow-reacting polymer ($\tau > 30$ min) inside a 2.5- to 4-cm-long trap (boxes 5–8) with a temperature difference of 10 K with an average trap temperature of 55 °C, a dissociation constant of $K_D = 0.1$ μM for polymerization, and an initial monomer concentration of 1 nM in physiological salt concentration (150 mM NaCl, $\lambda_{Debye} = 0.8$ nm). (*B*) Escalation of trapping as the accumulated RNA concentration reaches the K_D of polymerization. (*C*) Mean polymer length for varying pore heights and dissociation constant K_D. Even for low affinities a plausible trap height is found at which polymerization escalates and the polymer length diverges hyperexponentially.

Table S1. Description of all used channels and polymerization conditions by a pattern NM_x

Channel	Excitation	Emission	Monomer labeling	Monomer allows polymerization
DA	FAM 482 nm	ROX 630 nm	ROX/FAM	Yes
DD	FAM 482 nm	FAM 536 nm	ROX/FAM	Yes
AA	ROX 586 nm	ROX 630 nm	ROX/FAM	Yes
AA_A	ROX 586 nm	ROX 630 nm	ROX	No
DD_D	FAM 482 nm	FAM 536 nm	FAM	No
DA_D	FAM 482 nm	ROX 630 nm	FAM	No
DA_A	FAM 482 nm	ROX 630 nm	ROX	No

The letters N(M) denote the excitation (emission) wavelength (D, donor; A, acceptor). Index x denotes which dyes were used for monomer labeling (no index: monomers labeled with both dyes).

Table S2. Definition of FRET crosstalk ratios

Correction	Description
$dd(T)$	Temperature-dependent crosstalk ratio by donor $DA_D(T)/DD_D(T)$
$aa(T)$	Temperature-dependent crosstalk ratio by acceptor $DA_A(T)/AA_A(T)$

Temperature-dependent donor ($dd(T)$) and acceptor ($aa(T)$) crosstalk ratios were measured to correct for non-FRET–associated signals in the DA channel.

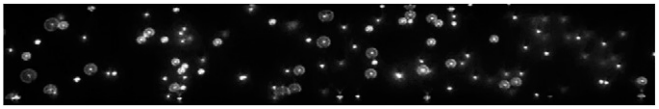

Movie S1. Fluid flow velocity was recorded by tracking homogeneously distributed 1-μm green fluorescent silica particles (PSI-G1.0NH2; Kisker), using the same experimental settings as in the polymerization trap. The mean fluid speed was determined to be 28 ± 2 μm/s. The silica beads used in this measurement exhibit a considerably lower diffusion coefficient compared with DNA. Accordingly the beads are not trapped but continuously cycled between the hot and the cold side of the compartment. Clay particles with similar slow diffusion could therefore act as a catalyst for nucleotide-based reactions on the cold side, while their surface is being reset for another cycle at the hot side.

Movie S1

Thermal Trap for DNA Replication

Christof B. Mast and Dieter Braun*

Systems Biophysics, Physics Department, Center for Nanoscience, Ludwig Maximilians Universität München, Amalienstrasse 54, 80799 München, Germany

(Received 1 August 2009; published 7 May 2010)

The hallmark of living matter is the replication of genetic molecules and their active storage against diffusion. We implement both in the simple nonequilibrium environment of a temperature gradient. Convective flow both drives the DNA replicating polymerase chain reaction while concurrent thermophoresis accumulates the replicated 143 base pair DNA in bulk solution. The time constant for accumulation is 92 s while DNA is doubled every 50 s. The experiments explore conditions in pores of hydrothermal rock which can serve as a model environment for the origin of life.

DOI: 10.1103/PhysRevLett.104.188102 PACS numbers: 87.14.gk, 87.15.R−

Introduction.—Central to life is the buildup of structure. This requires the reduction of local entropy. As result, living systems have to be driven by nonequilibrium boundary conditions to agree with the second law of thermodynamics [1,2]. Modern cells use a complex metabolism and transport nutrients directionally across the cell membrane. But how could prebiotic molecules be accumulated with a nonequilibrium setting from a probably highly diluted ocean [3,4]?

A second central aspect is the replication of information-bearing molecules such as DNA or RNA. How could these molecules replicate and at the same time be hindered to diffuse out into the ocean? Ideally, evolution would be hosted by physical boundary conditions which drive a replication reaction and at the same time accumulate the replicated molecules against diffusion.

We experimentally show here a simple thermally driven system which replicates DNA by using a polymerase protein and simultaneously accumulates the replicated molecules in an efficient thermophoretic trap. The nonequilibrium driving is solely provided by a thermal gradient, possibly between warm volcanic rock and colder ocean water, a ubiquitous setting on the early earth [5,6].

This work brings together two lines of research. On the one hand, thermal convection [7] and thermophoresis [8] was initially shown to trap long DNA molecules under low salt conditions. Subsequently, it was pointed out theoretically that even single nucleotides should accumulate in centimeter-long cracks of hydrothermal rock [5] [Fig. 1(a)]. This approach was recently shown to accumulate lipids to form vesicles [9] and to trap 5 base pair DNA [10]. On the other hand, the exponential replication of DNA is provided in our experiments by the polymerase chain reaction (PCR) where DNA is periodically molten by a temperature oscillation and as a result, replicated with a primer-directed polymerase protein. Microthermal convection in various shapes was previously shown to provide the necessary temperature cycling for PCR [11–16] with exponential yield [12]. Under convection, DNA denatures into two strands in the warm region [Fig. 1(b)] before it is shuffled by convection to colder regions where it can be replicated. Target inhibition [17,18] is circumvented by the periodic binding or unbinding protocols. This is essential for exponential replication, which itself is highly preferred in Darwinian evolution [19].

However, the convection geometries were not optimized for concurrent accumulation. Here, we show that both accumulation and replication of 143 base pair DNA can be implemented in an elongated single chamber. We used a glass capillary where the convection flow was driven by light driven microfluidics to achieve controllable experimental conditions [20,21]. The setting bodes well to select replicated molecules under continuous PCR using a superposed fluid flow.

Materials and methods.—We use a borosilicate capillary (VitroCom) with a rectangular cross section of 100 μm × 50 μm, embedded into immersion oil and sandwiched between an IR-transparent silicon wafer and a sapphire cover slip to enhance thermal gradients. The silicon wafer

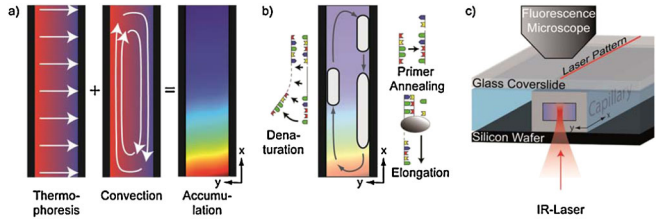

FIG. 1 (color online). Trapping and replicating DNA by thermal convection. (a) As molecules are directed to the right by thermophoresis, they are transported downward by the convection and accumulate at the bottom of the chamber. (b) Convection provides a temperature oscillation to periodically denature DNA with subsequent binding of short primers and replication by a polymerase protein. As a result, DNA is duplicated in each convection cycle. (c) A borosilicate capillary with rectangular cross section is heated symmetrically with an infrared laser. Directed scanning provides a convectionlike flow pattern due to light-driven microfluidics [20,21].

is cooled with Peltier elements (9502/065/018 M, Ferrotec) to 24 °C. The filled capillary is sealed on both ends by a reservoir of paraffin oil to prevent fluid drift. Imaging is realized with a fluorescence microscope (Axiotech Vario, Zeiss) using a high power cyan LED for illumination (Luxeon V Star, Lumiled lighting) and a CCD camera (Luca SDL-658M, Andor) using an air objective ($20x$, UPlanSApo $NA = 0.75$, Olympus).

Heating and thermoviscous flow is provided by an IR laser (1940 nm, 10 W, TLR-10-1940, IPG, Burbach) from the bottom. It is focused inside the capillary with a lens (C240TM, Thorlabs) after being deflected with scanning mirrors (6200-XY, Cambridge Technology). A heat bath (F20, Julabo) cools the microscope stage. Temperature imaging is provided with 50 μM of the dye BCECF [2′,7′-bis-(2-carboxyethyl)-5-(and-6)-carboxyfluorescein, Invitrogen] in 10 mM TRIS-HCl buffer, 150 ms after switching on the laser and normalized against a previously taken cold picture [22,23]. The fluorescence decrease was calibrated by temperature dependent fluorescence measured in a fluorometer (Fluoromax-3, Horiba).

Fluid flow velocity was tracked with homogeneously distributed 1 μm fluorescent beads (F8888, Invitrogen) in the initial 5 seconds after the laser was switched on. Maximal recorded flow speed of $v_{\max} = 70$ μm/s indicated a chamber averaged velocity of $v = 2/3 v_{\max} \approx 45$ μm/s. Finite element simulations were performed with FEMLAB (COMSOL), slightly modifying previous simulations [5]: the measured temperature profile replaced the previously linear temperature profile, and the flow pattern was approximated by gravitational flow (See Ref. [24]).

The PCR solution consists of 20 μl FastPCR master mix (Qiagen), 2 μl of 143 mer single stranded oligonucleotide template with random internal sequence at various concentrations, 2 × 2 μl primer (sequences 5′-cccagctctgagcctcaagacgat-3′, 5′-ggcttaaaagcagaagtccaaccca-3′) with a final concentration of 500 nM, 2 μl 10 x SYBR Green I (Invitrogen), 2 μl 60 mg/ml BSA (biotin free, Roth), and 12 μl H_2O. PCR with 30 reaction cycles of denaturation at 96 °C (30 s), annealing at 53 °C (30 s), and elongation at 68 °C (30 s) were applied after 5 min of initial hot start at 95 °C. Reference PCR products were amplified in a RapidCycler (Idaho Technology) with 50 pM template DNA. DNA length and concentration were calibrated against standards with a 1.5% agarose gel.

Accumulation.—Short 143 base pair dsDNA accumulates by convection and thermophoresis. The convection flow is created optically with thermoviscous pumping [20,21] in an elongated pore geometry of size 100 μm × 1800 μm allowing for two mirror-symmetric convection rolls of width $a = 50$ μm and mimicking gravitationally driven convection. Thermophoretic drift $j_T = -D_T c \nabla T$ is characterized by the thermodiffusion coefficient D_T, driving the DNA along the horizontal thermal gradient ∇T [Fig. 2(c)]. This concentration bias towards the cold sides is accumulated to the chamber center by the fluid flow [Fig. 2(d)].

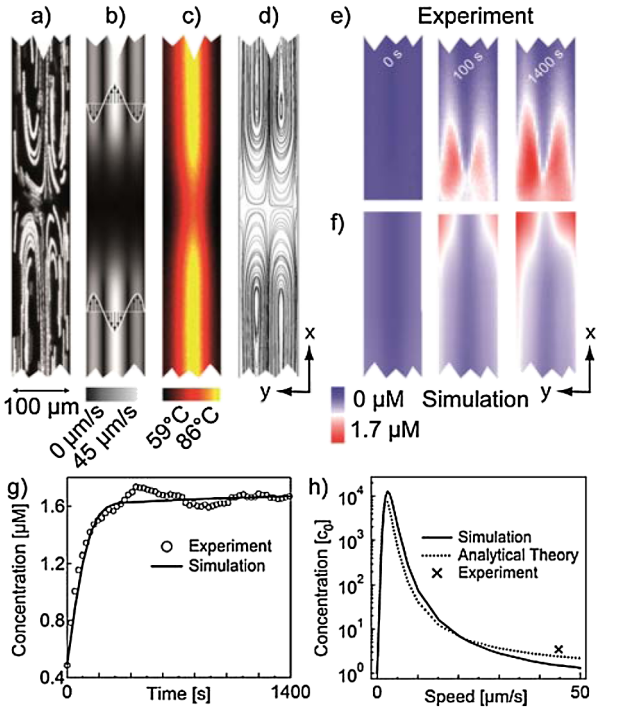

FIG. 2 (color online). Accumulation of DNA. (a) In the chamber center, the convection flow was tracked with 1 μm particles. The chamber averaged flow speed is 45 μm/s. (b) The corresponding flow profile for the finite element simulation. (c) The temperature profile was measured using a temperature dependent dye [8]. (d) Molecular trajectories by the superposition of fluid flow and thermophoresis. (e) Fluorescence images show the DNA accumulation over time. (f) The concentration pattern over time is reasonably described theoretically. (g) The kinetics of central accumulation is well described theoretically. (h) Optimal convection speed for accumulation is around 2.5 μm/s. The experimental conditions favor faster PCR replication under reduced accumulation.

Above concentration mechanism is counterbalanced by diffusion, resulting in a concentration plateau after 300 s as measured by the intercalating DNA dye SYBR Green I [Fig. 2(e)]. Concentration increases to 1.7 μM of DNA, up from the initial 0.49 μM concentration. The experimental result is described reasonably well by a time dependent simulation using the measured temperature and flow profile [Fig. 2(f)].

The accumulation kinetics in the center is shown in Fig. 2(g). A hydrodynamic time constant $\tau_{\text{Trap}} = 2l/v = 80$ s for accumulation can be estimated from the convection flow and the chamber length l and agrees well with the experimentally found accumulation time of 92 s. Further accumulation is kinetically limited by diffusive refilling at the outer boundaries of the flow [10]. The steady state accumulation of a thermogravitational column can be described by [25]

$$\frac{c_{\text{Trap}}}{c_0} = \exp\left(\frac{q/120}{1 + q^2/10\,080} S_T \Delta T r\right), \qquad (1)$$

with q defined as

$$q = \frac{\Delta T \alpha g \rho_0 a^3}{6\eta D}, \tag{2}$$

where c_{Trap}/c_0 denotes the ratio of the DNA concentration at the accumulation center to the outer boundaries, $S_T = D_T/D$ the Soret coefficient, D the ordinary diffusion coefficient, $r = l/a$ the aspect ratio of the convection, η the viscosity of the solvent, ρ_0 the density of the solvent, α the volume expansion of the solvent, and g the local acceleration due to gravity. The maximum convection flow velocity in a 2D chamber is given by [25]

$$v = \frac{\Delta T \alpha g \rho_0}{6\eta} a^2 \frac{3}{64}. \tag{3}$$

By eliminating g, we obtain the accumulation ratio depending on the convection flow v

$$\frac{c_{\mathrm{Trap}}}{c_0}(v) = \exp\left(\frac{504 v a S_T \Delta T r D}{2835 D^2 + 128 v^2 a^2}\right). \tag{4}$$

It matches well with the finite element simulation [Fig. 2(h)]. Although flow and temperature gradient were created by an infrared laser, the conditions do not differ significantly from gravitational driving.

Accumulation and PCR.—In the same setting, the DNA molecules follow the fluid flow and are cycled through a temperature difference of 27 K with an average cycling time based on the convection flow of $\tau_{\mathrm{cycle}} = 2l/v = 80$ s. This is an upper bound since the inclusion of thermophoretic drift tends to shorten the cycle time. Based on the size and charge of DNA [5,8], we expect the preferential accumulation of DNA. However, even if all the components of the PCR mix accumulate, they would still thermally cycle, albeit on shorter molecular trajectories.

The PCR reaction is driven by the melting of the 143 mer at 86 °C and primer binding and replication at 59 °C. The generated DNA is accumulated by the trap dynamics. With template DNA, we find an increased fluorescence in the trap, but only background fluorescence is detected without template [Fig. 3(a)]. For the concentration of replicated but not yet trapped DNA, we expect a raise in fluorescence given by a sigmoidal curve with doubling time τ_{doubling} and amplification delay $t_{1/2}$ [26]

$$c_{\mathrm{PCR}}(t) = \frac{c_{\max}}{1 + \exp[\ln(2)(t_{1/2} - t)/\tau_{\mathrm{doubling}}]}. \tag{5}$$

The initial single-stranded DNA is immediately elongated to double-stranded DNA by the polymerase in the first round. The reaction therefore effectively starts with double-stranded DNA. No significant contribution to the fluorescence signal is expected as its concentration is 500-fold and 85.000-fold lower than the final replicated and accumulated product [Fig. 3(c)]. The DNA which replicated homogeneously at time $t - \tau$ is accumulated by the trap with time delay τ. So the concentration of trapped PCR product will follow

$$c_{\mathrm{TrappedPCR}}(t) = \int_0^t c_{\mathrm{Trap}}(\tau) \dot{c}_{\mathrm{PCR}}(t - \tau) d\tau. \tag{6}$$

The shape of the concentration increase leads for template containing probes to $\tau_{\mathrm{doubling}} = 74$ s. A reduced template DNA concentration delays the replication of PCR. We find $t^A_{1/2} = -8$ s for $c_A = 3500pM$ of initial DNA and $t^B_{1/2} = 380$ s for $c_B = 20pM$. From this, we infer a doubling time of $\tau_{\mathrm{doubling}} = \ln 2(t^B_{1/2} - t^A_{1/2})/\ln(c_A/c_B) \approx 50$ s which fits the data equally well [Fig. 3(c), solid line]. As discussed [26], this evaluation using $t_{1/2}$ should be more reliable than the fitting of τ_{doubling} from the sigmoidal shape. The fact that τ_{doubling} is slightly smaller than τ_{cycle} might indicate a shortening of the DNA trajectories or a possible cotrapping of the PCR mix.

Controls.—The thermophoretic characteristics of amplified DNA were compared against DNA amplified in a standard cycler. Standard methods are not available to verify the length of the replicated DNA due to the low product volumes in the capillary. Lengths of the expected 143 mer, shorter 86 mer, and longer 1530 mer were created by standard PCR and confirmed using gel electrophoresis [Fig. 4(a)].

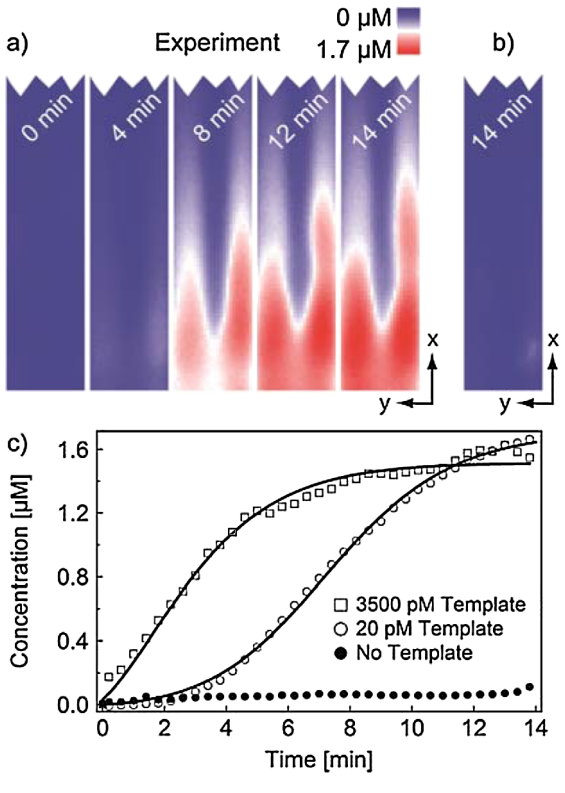

FIG. 3 (color online). Replication Trap. (a) Accumulation of PCR product by convection and thermophoresis, visualized by SYBR Green fluorescence. (b) No DNA is found without template DNA. (c) Center concentration over time and fits with Eq. (6). Delays of replication due to different template concentrations allow us to infer the replication doubling time with $\tau_{\mathrm{doubling}} = 50$ s.

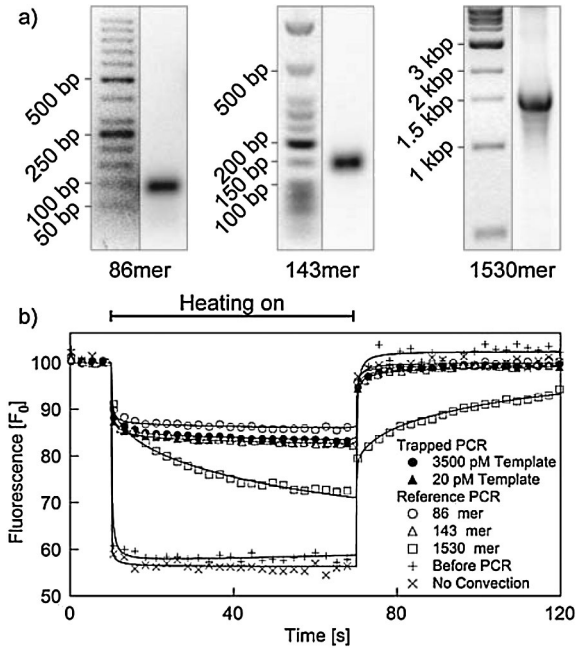

FIG. 4. Verification of the product. (a) Gel electrophoresis of product from a standard PCR cycler. Different primers yield product lengths of 86, 143, and 1530 base pairs. (b) In the capillary, the product is identified using thermophoresis [27,28]. Upon local heating with a laser spot, DNA is locally depleted. The amplified product matches the 143 base pair product and is well bracketed by 86 mer and 1530 mer product.

A low power IR laser spot was temporarily generated with a Gaussian temperature profile with $T_{\max} = 9$ K and width $\sigma = 100$ μm in the capillary in the accumulated spot after the PCR has finished. Thermophoretic depletion and backdiffusion was recorded by fluorescence [Fig. 4(b)]. From the time trace, we infer the diffusion coefficient D and the thermodiffusion coefficient D_T [8,27,28]. The product of the replication trap agrees with the 143 mer in both $D = 23$ μm^2/s and $D_T = 0.26$ μm^2/s K (solid line) and is bracketed by the shorter and longer DNA signal. Longer DNA with 1530 base pairs is clearly distinguishable and yields $D = 1.7$ μm^2/s and $D_T = 0.24$ μm^2/s K whereas the 86 mer yields $D = 25$ μm^2/s and $D_T = 0.15$ μm^2/s K. No product shows a large temperature dependence with a fast diffusion kinetics indicating unbound SYBR Green. We find these characteristics before PCR or for a symmetric scanning pattern that heats without fluid flow [Fig. 4(b)].

Discussion and outlook.—We showed that temperature gradients across elongated pores can drive both replication and accumulation of short DNA. Our experiment mimics conditions in pores of hydrothermal vents [5], but also has biotechnological relevance for HPLC or capillary electrophoresis. It bodes well for continuous feeding of PCR by a slow capillary flow while trapping the replicated DNA at a fixed position. The setting yields 1700 DNA replications within 24h, considerably faster than for example *E. coli* with 70 replications per day.

We thank Hubert Krammer for reading the manuscript. Financial support from the NanoSystems Initiative Munich, the International Doctorate Program NanoBioTechnology, and the LMU Initiative Functional Nanosystems is gratefully acknowledged.

*dieter.braun@lmu.de

[1] J. S. Wicken, J. Theor. Biol. **72**, 191 (1978).
[2] D. Braun and A. Libchaber, Phys. Biol. **1**, P1 (2004).
[3] K. Dose, BioSystems **6**, 224 (1975).
[4] S. J. Mojzsis, T. M. Harrison, and R. T. Pidgeon, Nature (London) **409**, 178 (2001).
[5] P. Baaske *et al.*, Proc. Natl. Acad. Sci. U.S.A. **104**, 9346 (2007).
[6] W. Martin and M. J. Russell, Phil. Trans. R. Soc. B **358**, 59 (2003).
[7] D. Braun and A. Libchaber, Phys. Rev. Lett. **89**, 188103 (2002).
[8] S. Duhr and D. Braun, Proc. Natl. Acad. Sci. U.S.A. **103**, 19678 (2006).
[9] I. Budin, R. J. Bruckner, and J. W. Szostak, J. Am. Chem. Soc. **131**, 9628 (2009).
[10] F. M. Weinert and D. Braun, Nano Lett. **9**, 4264 (2009).
[11] M. Krishnan, V. M. Ugaz, and M. A. Burns, Science **298**, 793 (2002).
[12] D. Braun, N. L. Goddard, and A. Libchaber, Phys. Rev. Lett. **91**, 158103 (2003).
[13] E. K. Wheeler *et al.*, Anal. Chem. **76**, 4011 (2004).
[14] D. Braun, Mod. Phys. Lett. B **18**, 775 (2004).
[15] M. Hennig and D. Braun, Appl. Phys. Lett. **87**, 183901 (2005).
[16] N. Agrawal, Y. A. Hassan, and V. M. Ugaz, Angew. Chem., Int. Ed. **46**, 4316 (2007).
[17] G. von Kiedrowski, Angew. Chem., Int. Ed. **98**, 932 (1986).
[18] A. Luther, G. Brandsch, and G. von Kiedrowsky, Nature (London) **396**, 245 (1998).
[19] E. Szathmáry and I. Gladkih, J. Theor. Biol. **138**, 55 (1989).
[20] F. M. Weinert, J. A. Kraus, T. Franosch, and D. Braun, Phys. Rev. Lett. **100**, 164501 (2008).
[21] F. M. Weinert and D. Braun, J. Appl. Phys. **104**, 104701 (2008).
[22] P. Baaske, S. Duhr, and D. Braun, Appl. Phys. Lett. **91**, 133901 (2007).
[23] M. L. Cordero, E. Verneuil, F. Gallaire, and C. N. Baroud, Phys. Rev. E **79**, 011201 (2009).
[24] See supplementary material at http://link.aps.org/supplemental/10.1103/PhysRevLett.104.188102 for the FEMLab 3.1 file of the numerical simulation.
[25] P. Debye, Ann. Phys. (Leipzig) **428**, 284 (1939).
[26] S. Swillens, B. Dessars, and H. E. Housni, Anal. Biochem. **373**, 370 (2008).
[27] S. Duhr, S. Arduini, and D. Braun, Eur. Phys. J. E **15**, 277 (2004).
[28] P. Reineck, C. J. Wienken, and D. Braun, Electrophoresis **31**, 279 (2010).

Reviews

International Journal of Modern Physics B
Vol. 26, No. 32 (2012) 1230017 (13 pages)

DOI: 10.1142/S0217979212300174

World Scientific
www.worldscientific.com

THERMAL SOLUTIONS FOR MOLECULAR EVOLUTION

CHRISTOF B. MAST, NATAN OSTERMAN and DIETER BRAUN

Systems Biophysics, Physics Department,
Center for Nanoscience Ludwig Maximilians Universtät München,
Amalienstrasse 54, 80799 München, Germany

Received 15 October 2012
Accepted 1 November 2012
Published 28 November 2012

The key requirement to solve the origin of life puzzle are disequilibrium conditions. Early molecular evolution cannot be explained by initial high concentrations of energetic chemicals since they would just react towards their chemical equilibrium allowing no further development. We argue here that persistent disequilibria are needed to increase complexity during molecular evolution. We propose thermal gradients as the disequilibrium setting which drove Darwinian molecular evolution. On the one hand the thermal gradient gives rise to laminar thermal convection flow with highly regular temperature oscillations that allow melting and replication of DNA. On the other hand molecules move along the thermal gradient, a mechanism termed Soret effect or thermophoresis. Inside a long chamber a combination of the convection flow and thermophoresis leads to a very efficient accumulation of molecules. Short DNA is concentrated thousand-fold, whereas longer DNA is exponentially better accumulated. We demonstrated both scenarios in the same micrometer-sized setting. Forthcoming experiments will reveal how replication and accumulation of DNA in a system, driven only by a thermal gradient, could create a Darwinian process of replication and selection.

Keywords: Molecular evolution; nonequilibrium; replication; Darwin process; thermophoresis; convection; microfluidics; origin of life.

1. Introduction

The origin of life problem is commonly explained by a top-down (or shall we rather say present–past) approach which includes simplified versions of complex molecular machinery as it is known today. However, the boundary conditions which drove and sustained such a nonequilibrium system are not clarified. The approach therefore might miss important restrictions based on metabolism or thermodynamic boundary conditions. An alternative bottom-up approach taken here, experimentally based on biochemistry, physics and geology of systems far away from thermodynamic equilibrium can reveal unexpected complementary information.

Typically, experiments which explore molecular evolution start with a disequilibrium system which then dies by equilibrating into its chemical steady state

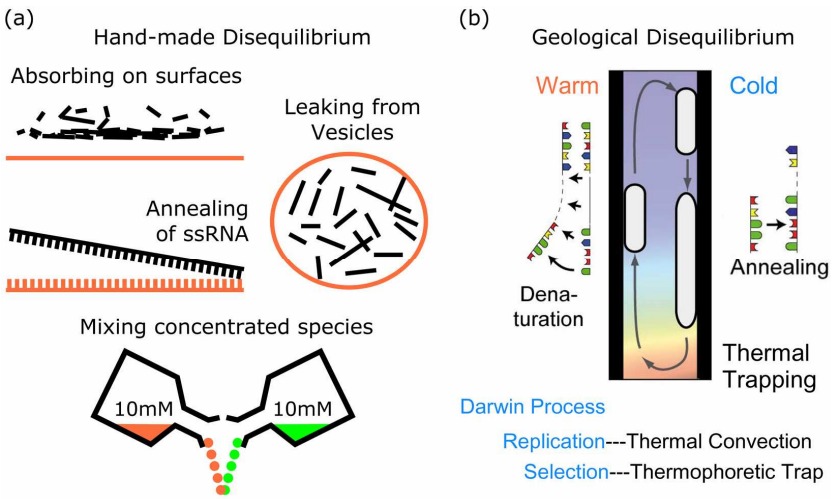

Fig. 1. Hand-made versus geological disequilibrium condition. (a) In most experimental scenarios of molecular evolution an invisible hand prepares an initial disequilibrium condition which then decays into equilibrium. As a result, a dying system is observed. (b) A continuous disequilibrium is required to host a system that can evolve into ever more complexity. We pursue the example of a thermal gradient. On the one hand thermal convection provides thermal oscillation that opens and closes RNA structures, which possibly leads to cycles of RNA replication. On the other hand, the pore implements a thermal trap by superposition of convection and thermophoresis. This provides monomers in sufficient concentration and in parallel retains the longer replicated molecules in a strongly length dependent way. We hypothesize that thus a thermal gradient can host a Darwin process of replication (by convection) and selection (by length dependent thermophoretic trapping). As reviewed here, we could experimentally show major steps of this hypothesis.

[Fig. 1(a)]. While this concept is typical and instructive for irreversible chemical synthesis such a concept will not be enough to explore the driving forces behind early molecular evolution. The invisible hand which creates the initial disequilibrium is often hidden in the materials and methods section. For example, surfaces for catalysis are prepared fresh and clean initially, nucleotides are provided in their energy-rich single stranded form to prevent template inhibition or generally, highly concentrated, pure chemicals are added to drive the reaction. However, these approaches will not explore persistent molecular evolution in a geochemical setting. Natural disequilibrium settings have to be in place to drive evolution and to harvest their results. However, only few experimental explorations based on persistent, at best geochemical disequilibrium have been pursued. We think there are many ways to implement the disequilibrium systems of early geology.

We have focused on thermal gradients as a persistent disequilibrium system. They show the interesting dynamics of continuous laminar flow perpendicular to the temperature difference [Fig. 1(b)]. Two processes in such a chamber can give rise to a Darwin process of replication and selection. Nucleotides can overcome template inhibition in the thermal cycling of convection, allowing for various schemes of physical replication. In our case we used a polymerase chain reaction (PCR) as

proxy for an exponential replication, where a polymerase protein fixes the result of replication. Second part of the Darwin process is selection, provided by the strongly length selective thermal trapping process. As result, monomeric molecules are actively accumulated, giving raise to replicating polymerization reactions. The longest replication products are retained in the system by the length selective thermal trap. Both processes are simply driven by a thermal gradient.

Corliss, Russell, Hall, Cairns-Smith, Matsuno, Martin and others proposed hydrothermal systems on the deep-sea floor as a suitable environment for the origin of life which provides thermal gradients inside water-filled pores.[1–8]

Hydrothermal vents create large flows of hot water (50°C–370°C) which is contrasted by 2°C cold ocean water on the outside. In between are porous mineral precipitates and rocks with a multitude of porous spaces that provide the requirements for a complex network of convection chambers. One can imagine also other sources of thermal gradients, for example the large space of subsurface clefts which might be more probable on the early earth. A network of such diverse sized chambers could effectively dictate different tasks, like the separate trapping of polymers of different lengths in distinct compartments.

The research of thermal gradients is interesting also from applicative point of view. For example, the movement of proteins in a temperature gradient is a sensitive and versatile way to probe protein interactions,[9,10] including the important class of membrane receptors binding to its target molecule.[11] The binding was detected all-optically in various biological fluids. We screened for drug-protein interactions without labeling the protein and were able to successfully commercialize the method.

Another novel use of thermal gradients is thermoviscous pumping.[12,13] Selected parts of a fluid film are pumped along the path of a moving warm spot which is generated by the repetitive motion of an infrared laser focus. With this technique, we could remotely drive arbitrary two-dimensional fluid flow patterns with a resolution of 20 μm. The mechanism is based on the dynamic thermal expansion in a gradient of viscosity. As the viscosity in the spot is reduced by its enhanced temperature, the symmetry is broken and as a result the fluid flows opposite to the spot movement. This demonstration of optical remote control of fluid flow expands the microfluidic paradigm into previously inaccessible regimes of tiny volumes, closed flow paths, fast switching between flow patterns and remote fluid control under extreme fluidic conditions. Recent extensions of the approach move molecules in ice, in this case driven by the phase transition between frozen and liquid water.[14]

2. Thermal Convection on a Micro-Scale Level

A temperature gradient applied across a liquid filled chamber gives rise to thermal convective flow as a result of density changes. In the hot regions of the chamber the liquid thermally expands and rises whereas in the colder regions it contracts and moves downwards.

One of the important measures to characterize a fluid flow is the Reynolds number ($\mathrm{Re} = \rho v L/\mu$) which is a ratio of inertial forces to viscous forces. The flow is laminar and characterized by smooth fluid motion below $\mathrm{Re} = 1000$, while above it the flow is turbulent, full of chaotic eddies, vortices and other instabilities. In the case of water (density $\rho = 1000$ kg, dynamic viscosity $\mu = 10^{-3}$ Pa s) and temperature gradients of some 10 K the laminar convection flow occurs in chambers with a characteristic dimension L smaller than a few centimeters and larger than 100 nm, a limit imposed by molecular diffusion.

A two-dimensional finite element simulation (Femlab, Comsol) of a convective flow of water in an elongated chamber is presented in Fig. 2. The flow is driven solely by a horizontal temperature gradient. As expected in the low Reynolds number regime, the flow is laminar without any instability. A slowly-diffusing particle like DNA located on a certain trajectory remains on the same trajectory, travels around the chamber and finally returns to the same initial position.

As shown in Fig. 3, the maximum fluid velocity is linearly proportional to the applied thermal gradient across the pore. The velocity is on the order of 1000 μm/s for chambers with dimensions of a few millimeters and a temperature difference of 40 K between the left and the right wall. The simulation reveals that the maximum fluid velocity strongly depends on the aspect ratio (height/width) of the pore at a given temperature gradient.

In Fig. 4 we highlight two example trajectories and present the course of temperature experienced by particles "sitting" on them. Diffusion bridges between different trajectories at much longer times than the temperature oscillation of convection. A single chamber can thus simultaneously host a number of thermal cycling conditions which interact at time scales longer than the convective return times. This principle has been successfully used for convective polymerase chain reactors.

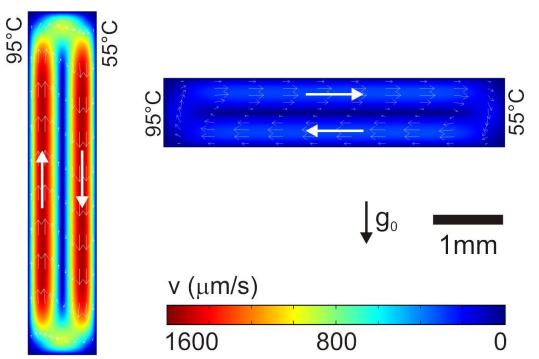

Fig. 2. Simulated thermal convection in vertically and horizontally oriented elongated chambers. The applied temperature difference of 40 K in the horizontal direction results in laminar flow with velocities up to 1600 μm/s. The liquid rises in the hot region of the chamber and sinks in the cold region.

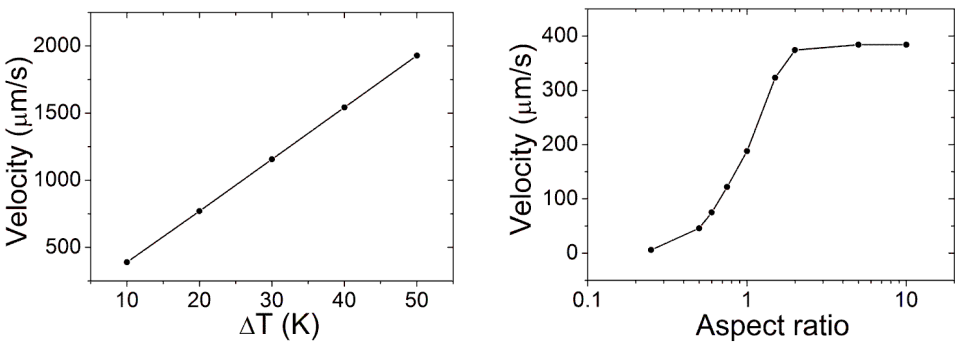

Fig. 3. (a) Fluid velocity in linearly proportional to the applied temperature difference across the chamber. The chart shows maximum fluid velocity for a vertically oriented 1 mm × 5 mm chamber of Fig. 2. (b) Dependence of the maximum fluid velocity on the aspect ratio (height/width of the chamber) for a 1 mm wide chamber with the applied temperature difference of 10 K.

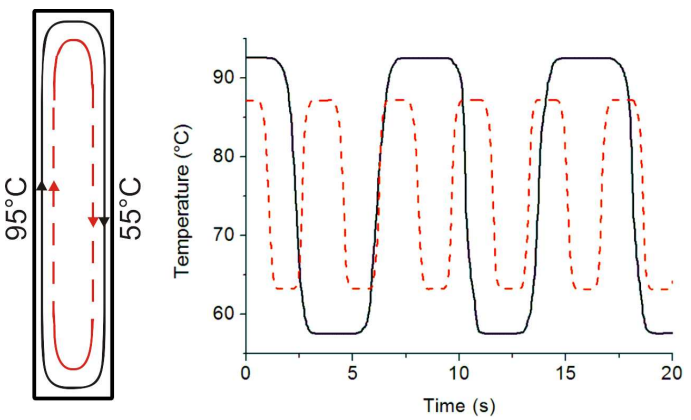

Fig. 4. (Color online) The temperature versus time along two convective flow trajectories in a millimeter-wide vertical pore with the temperature difference of 40 K. A molecule in the outer trajectory (denoted by the black solid line) experiences slow temperature cycling between 58°C and 92°C with the period of 7.5 s. Molecules in the inner trajectory (denoted by the red dashed line) cycle between temperatures 63°C and 87°C with the period of 3 s.

3. Exponential Replication in Convection Chambers

Replication is fundamental for the existence of life. Information is passed on to daughter cells by replication of genetic information. The exponentiality of the growth is central to ensure a fast spread of innovations throughout the population to the point that competing species become extinct. We will show in the following section that the continuous thermal oscillation of thermal convection can drive exponential replication.

In addition to the common exponential growth of the contemporary populations, one has to consider also nonconventional types of growth when discussing

the prebiotic evolution. The simplest general description of the population growth with a kinetic equation $dx/dt = kx^p$. The type of growth dynamics depends solely on the exponent p. The most known reproduction is exponential or Malthusian growth ($p = 1$) where a parent object splits into multiple child objects.[15] A slightly more complicated growth type is when more than one parent is necessary to produce an offspring. Such hyperbolic growth ($p > 1$) was discussed by Eigen in the context of hypercycles.[16] Parabolic growth ($0 < p < 1$) occurs when the replication is self-limiting, for example due to the inhibition of the template in the prebiotic evolution. It was first experimentally demonstrated by von Kiedrowski[17] who showed that oligonucleotide analogues follow a square root growth law. The reason for such sub-exponential growth is the template "poisoning" — a copy of the template remains associated with the template and therefore prevents further replication.

A typical example of the exponential growth is the PCR, which replicates a single or a few copies of a piece of DNA across several orders of magnitude, generating thousands to millions of copies of a particular DNA sequence. PCR proceeds in three steps which are periodically repeated: (i) *melting*: heating a DNA double helix at 95°C to dissociate the double helix into two single strands; (ii) *annealing*: decreasing the temperature to 55–65°C in the presence of a large excess of two short DNA fragments also called primers. The primers are complementary to the terminal target sequence and form short double helices at the ends; (iii) *replication*: raising the temperature to 72°C in the presence of a thermostable polymerization enzyme called polymerase which elongates each of the two short double helices to generate twice the amount of the target DNA. The temperature cycling can be simplified in many cases to only two temperature levels with a typical cycling period and thus doubling time between 5 s and 5 min.

The process of PCR is performed in dedicated thermocyclers, which cycle the reaction solution through three (or two) predefined temperatures. As shown in the previous chapter, the liquid in the convection chamber also undergoes temperature cycling. By choosing a suitable chamber geometry and appropriate thermal gradient, the induced convection flow shuttles the reaction liquid between regions with temperatures of about 65°C and 95°C, i.e., between a temperature profile capable of driving PCR. The geometry should also ensure that the cycling periods along laminar trajectories are compatible with the times needed for a PCR reaction.

Convective PCR has been demonstrated among various geometries. Wheeler *et al.*[18] designed a closed microfluidic tubing in the shape of a "0" that heats the liquid on one side and cools it on the other side. The advantage of such a design is the circulation of all the volume through both temperature zones. Krishnan *et al.*[19] designed a restricted Rayleigh–Bénard cell where the bottom of a cylindrical chamber was heated and the top cooled. Braun *et al.* devised a toroidal convection PCR where a mm-sized chamber is heated in the center by a focused infrared beam[20] or micro immersion heater[21] which leads to a hot center and colder periphery. The toroidal convection geometry creates only short heat pulses as the liquid passes the

central spot with high speed so the temperature profile is more compatible with the timing of a standard, nonconvective PCR.

As already pointed out it is central to ensure the exponentiality of the replication. To confirm it experimentally the chain reaction has to be monitored during the initial phase before restricting boundary conditions are reached. In PCR replication the product DNA concentration can be indirectly monitored by observing the fluorescence signal of an intercalating dye added to the reaction mixture. Starting from low fluorescence, the product of the chain reaction increases and reaches a saturation level after some cycles. To get the growth coefficient and confirm exponential replication one should not just fit the fluorescence measurement (because it is highly inaccurate) but rather opt for multiple reactions with varying initial template concentrations. For instance in Ref. 20, the initial DNA template concentration was varied over five orders of magnitude. As depicted in Fig. 5 the product appeared earlier with increasing template concentration, whereas the time to reach 10% of the final product concentration was shown to be a logarithmic function of the initial template concentration, a solid proof of the replication exponentiality.

4. Thermophoresis

Thermophoresis (also known as thermodiffusion or the Soret effect)[22,23] is the movement of particles in the direction of a thermal gradient, typically from hot to cold. The phenomenological foundation of the thermophoretic drift is the Onsager theory of linear nonequilibrium thermodynamics.[24] For low molecule concentrations the drift velocity is proportional to temperature gradient $v = -S_T D \nabla T$ with the diffusion coefficient D and the Soret coefficient S_T.

Thermophoretic experiments are theoretically described by two competing approaches. One disputes that thermophoresis is low Peclet number movement and

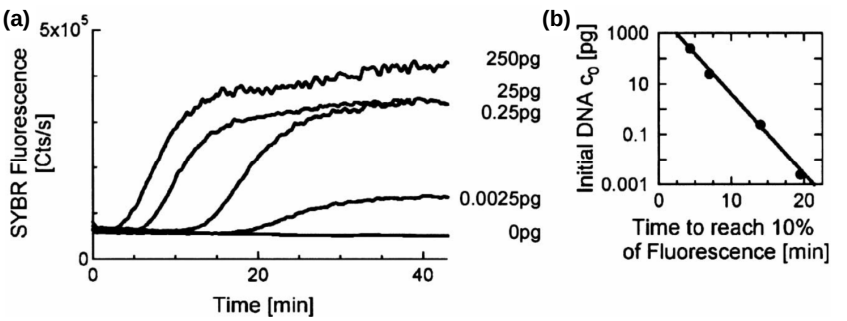

Fig. 5. Exponential amplification of an 86 base pair DNA molecule in thermal convection chamber. (a) The initial template concentration is varied over five orders of magnitude. The fluorescence of SYBR Green I intercalating dye is monitored at the periphery of the chamber with a counting photomultiplier to follow the product concentration during the cycling. The concentration rises during exponential growth phase and then saturates on a final plateau. No amplification is found without a template. (b) The time to reach 10% of the plateau amplification is a logarithmic function of initial DNA concentration. (Reprinted with permission from Ref. 20.)

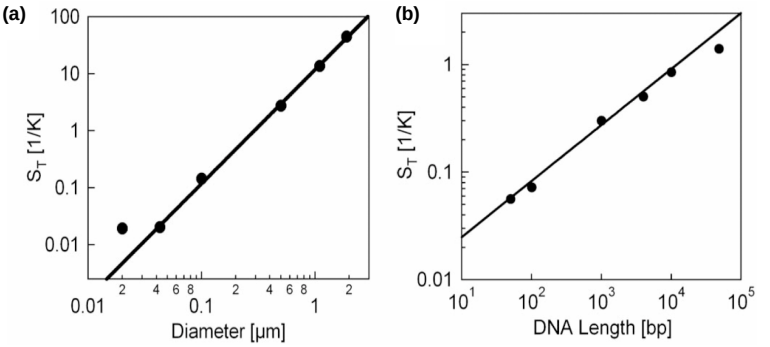

Fig. 6. Size dependence of Soret coefficients S_T. (a) For polystyrene beads, S_T scales with the particle surface over four orders of magnitude. (b) The S_T of DNA scales according to $S_T\sqrt{L}$. (Reprinted with permission from Ref. 25).

is rather a biased diffusion motion than a directed motion. The Soret coefficient is given by the negative solvation entropy, divided by kT when a local thermodynamic equilibrium of the solvent molecules around the molecule is assumed. This is fulfilled for moderate temperature gradients below a fluctuation criterion. Thermophoretic motion changes direction at lower temperatures for both DNA and polystyrene beads. This thermophilicity is attributed to the increase of positive entropy of hydration, whereas the generally dominating thermophobicity is explained by the negative entropy of ionic shielding. This approach is supported by a multitude of experiments,[25,26] where size and salt dependence of the measured thermophoresis are described without fit parameters for both polystyrene beads and long DNA as shown in Fig. 6. Contrary size dependencies have been measured in different experimental geometries, particles and methods[27] however without recording the salt dependence.

In the case of Peclet numbers larger than unity which corresponds to high thermal gradients and therefore ballistic particle movements, Maragoni-like fluid patterns emerge and particles show hydrodynamic attraction.[28]

The thermophoretic velocity in temperature gradient of less than 0.1 K/μm is usually well below 1 μm/s. Nevertheless, the inherent size selectivity of the effect (Fig. 6) and its unique sensitivity to interfacial properties of the molecule-water interface under complex buffer conditions make it a very sensitive tool to detect changes on a molecular level. All-optical fluorescence detection and infrared heating technique made thermophoresis a successful technique for the analysis of biomolecule affinity and activity. The approach, termed Microscale Thermophoresis[10] has been commercialized by NanoTemper Technologies (Munich, Germany). They developed a robust analytical platform suitable for a wide variety of biological settings. Experiments range from the quantification of the affinity of low molecular weight binders using fluorescently labeled proteins, to interactions between macromolecules and multi-component complexes like receptor containing liposomes.

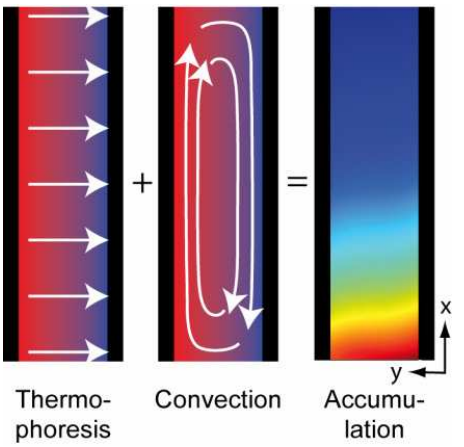

Fig. 7. Thermophoresis forces molecules to the cold side where they are transported downward by convection and as result accumulate at the bottom of the chamber. (Reprinted with permission from Ref. 32.)

Thermal Molecular Trap

The separation of molecules with different thermophoretic properties using a thermo-gravitational column was first proposed by Clusius and Dickel more than 70 years ago.[29] The thermo-gravitational column for industrial purification[30] is also a plausible model for the physical boundary conditions inside hydrothermal pores[31] on the deep-sea floor.

These pores are elongated, water-filled chambers that are sandwiched between the hot vent interior and the cool water of the ocean. The resulting temperature gradient across the pore drives two entangled processes as shown in Fig. 7: (i) molecules are shuttled up and down the cleft by laminar thermal convection and (ii) thermophoresis drives the molecules along the temperature gradient, i.e., perpendicular to the convection flow. The superposition of both processes leads to a massive separation of biomolecules e.g., DNA along the pore, according to

$$\frac{c_{\text{bottom}}}{c_{\text{top}}}(v) = \exp\left(\frac{504 \cdot v \cdot a \cdot D_T \cdot \Delta T \cdot r}{2835 \cdot D^2 + 128 \cdot v^2 \cdot a^2}\right), \tag{1}$$

where $c_{\text{bottom}}/c_{\text{top}}$ is the ratio of concentrations of a species with the thermal diffusion coefficient D_T and the ordinary diffusion coefficient D. Temperature difference ΔT is applied along the width of the pore, $r = l/a$ is the aspect ratio of the chamber that hosts a convection with a maximum flow velocity v. If we assume $c_{\text{top}} = c_r$ by attaching a infinite reservoir with a constant species concentration c_r, the separation inside the column is equivalent to a massive accumulation relative to the reservoir.

The Szostak group achieved the accumulation of fatty acids in a 30 mm $\times$ 0.2 mm thermal diffusion column[33] using $\Delta T = 30$ K and a gravitational driven convection. By reaching a high accumulation ratio $c_{\text{bottom}}/c_{\text{top}} = 80$, it was possible to exceed

the critical aggregate concentration at the pore bottom such that vesicles consisting of bilayer membranes could be generated.[34] Such membranes composed of single-chain amphiphiles are proposed to play a potential role as early cell membranes.

Braun *et al.* accumulated DNA by gravitational convection in a simple sheet of water. The thermal gradient was realized by the absorption of a focused IR Laser beam inside the water.[35] They achieved an accumulation ratio of up to $c_{\mathrm{bottom}}/c_{\mathrm{top}} = 2500$ for 5 kbp DNA in accordance with Eq. (1) and numerical finite element calculations. Due to the exponential size dependence of the Soret coefficient $S_T = D_T/D$ as shown in Fig. 6(b)[25,26] thermal diffusion columns also exhibit a strong size selectivity which could serve as a selection pressure in a Darwinian process.

5. Darwinian Process in a Convection Chamber

Thermal diffusion columns not only accumulate selectively larger bio-molecules, but also implement an inherent temperature cycling. Convective flow shuttles biomolecules among regions with different temperatures. In such boundary conditions, simple replication of genetic information could have taken place by molecular self-assembly with the subsequent prevention of template poisoning by periodic heating.[36] These properties could lead to a Darwinian process which includes selection and replication of information. Using PCR as proxy reaction, we could demonstrate the replication and simultaneous accumulation of 143mer dsDNA in a micro thermal diffusion column (Fig. 8).[32]

The convective fluid flow was provided by thermoviscous pumping.[12,13] The same pattern of the focused IR laser beam also created the thermal gradient. The time constant for accumulation was 92 s while DNA was doubled every 50 s. How-

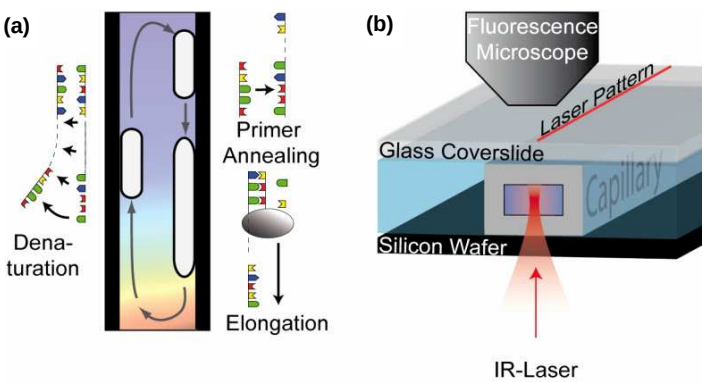

Fig. 8. Realization of a replication trap. (a) Convection provides a temperature oscillation to periodically denature DNA with subsequent binding of short primers and replication by a polymerase protein. As a result, DNA is duplicated in each convection cycle. (b) A borosilicate capillary with rectangular cross-section is heated symmetrically with an infrared laser. Directed laser scanning provides a convection-like flow pattern due to light-driven microfluidics. (Reprinted with permission from Ref. 32.)

ever, these numbers strongly depend on the geometry. Convection can for example reach 0.1 s return times in smaller chamber geometries (Fig. 4). The latter might also allow the fast cooling experiments run by Matsuno[4] in a single convection chamber. The convection certainly enables the implementation of adsorption/desorption cycles on clay particles for RNA polymerization as the particles are too large to be efficiently accumulated. The particles periodically add and remove large polymers on their surfaces and allow for efficient catalytic activities, as shown in the inherent periodic experiments of James Ferris.[37,38]

6. Conclusion and Outlook

Although thermal gradients might appear simple the combination of convection and thermophoresis provides very plausible boundary conditions for prebiotic evolution. A possible environment for this process might be elongated pores of rock with a width of 100–200 μm and a length scale of millimeters to centimeters that are spontaneously formed in great variety between the warm water flow of hydrothermal vents and the surrounding cold water on the deep-sea floor. In such pores biomolecules naturally accumulate to high concentrations.

At the same time thermal convection inherently gives rise to thermal oscillations which prevent template "poisoning", a crucial problem of RNA or DNA replication. Replication is otherwise always hindered by product inhibition, leading to slowly decelerating parabolic growth or no growth at all. As demonstrated, simple convection chambers provide environment for exponential replication, overcoming the limitation of product inhibition which is typically neglected in other scenarios of prebiotic evolution.

Since the same thermal gradient simultaneously drives both accumulation and replication[32] it is a natural step to contemplate upon the complete Darwinian process which, should in addition include evolutionary selection pressure. This can be achieved by a slow creep flow typical for hydrothermal vents. The larger (complex) molecules are predominantly accumulated after the replication while new monomeric molecules that are used as the source material for replication flow through the chamber and do not accumulate. Any waste products which are too small to be accumulated also leave the chamber. Thus replication and accumulation can, in principle run indefinitely. Moreover, connections to neighboring pores yield a very flexible and open playfield for lateral gene transfer between the replicating nucleotides. Once the genes were ready for competition on more than a molecule-against-molecule scale, lipids that co-accumulated provided vesicles around the genetic entities[33,34] to allow genome-level competition.

The ideas on the origin of life are converging, both on the experimental and theoretical level. We will see a number of more complex studies of molecular evolution along the line of thermal gradient induced disequilibrium settings. The main foci will be on achieving replication in thermal oscillations without complex proteins or chemistry and accomplishing the complete molecular evolution (including

mutations and competition of replicators) in the setting of a thermal gradient. We expect that the experiments will bring many new interesting results that could clarify the origin of life problem.

Acknowledgments

Financial support from the NanoSystems Initiative Munich, the International Doctorate Program NanoBioTechnology, the LMU Initiative Functional Nanosystems and the ERC Starting Grant is gratefully acknowledged.

References

1. J. B. Corliss, J. A. Baross and S. E. Hoffman, An hypothesis concerning the relationship between submarine hot springs and the origin of life on earth, *Proceedings 26th International Geological Congress, Geology of Oceans Symposium*, Paris, July 7-17, 1980, Oceanologica Acta (1981), pp 59–69.
2. M. J. Russell *et al.*, *Nature* **336**, 117 (1988).
3. M. J. Russell and A. J. Hall, *J. Geol. Soc. Lond.* **154**, 377 (1997).
4. E Imai *et al.*, *Science* **283**, 831 (1999).
5. E. G. A. J. Boyce, M. L. Coleman and M. J. Russell, *Nature* **306**, 545 (1983).
6. N. G. Holm (ed.), *Marine Hydrothermal Systems and the Origin of Life*, Vol. 22 (Kluwer Academic Publishers, Berlin, 1992), pp. 1–242.
7. W. Martin *et al.*, *Nat. Rev. Microbiol.* **6**, 806 (2008).
8. D. S. Kelley *et al.*, *Nature* **412**, 145 (2001).
9. P. Baaske *et al.*, *Angew. Chem.* **49**, 2238 (2010).
10. C. J. Wienken *et al.*, *Nat. Commun.* **1**, 100 (2010).
11. X. Wang *et al.*, *Proc. Natl. Acad. Sci. USA* **108**, 9049 (2011).
12. F. M. Weinert and D. Braun, *J. Appl. Phys.* **104**, 104701 (2008).
13. F. M. Weinert *et al.*, *Phys. Rev. Lett.* **100**, 164501 (2008).
14. F. M. Weinert, M. Wühr and D. Braun, *Appl. Phys. Lett.* **94**, 113901 (2009).
15. E. Szathmary and J. Maynard-Smith, *J. Theor. Biol.* **187**, 555 (1997).
16. M. Eigen, *Naturwissenschaften* **58**, 465 (1971).
17. G. von Kiedrowski, *Angew. Chem. Int. Ed. Engl.* **25**, 932 (1986).
18. E. K. Wheeler *et al.*, *Anal. Chem.* **76**, 4011 (2004).
19. M. Krishnan, V. M. Ugaz and M. A. Burns, *Science* **298**, 793 (2002).
20. D. Braun, N. L. Goddard and A. Libchaber, *Phys. Rev. Lett.* **91**, 158103 (2003).
21. M. Hennig and D. Braun, *Appl. Phys. Lett.* **87**, 183901 (2005).
22. C. Ludwig, *Sitzber. Akad. Wiss. Wien Math.- Naturw. Kl.* **20**, 539 (1856).
23. C. Soret, *Arch. Geneve* **3**, 48 (1879).
24. S. R. de Groot and P. Mazur, *Nonequilibrium Thermodynamics* (North-Holland, Amsterdam, 1969).
25. S. Duhr and D. Braun, *Proc. Natl. Acad. Sci. USA* **103**, 19678 (2006).
26. P. Reineck, C. J. Wienken and D. Braun, *Electrophoresis* **31**, 279 (2010).
27. M. Braibanti, D. Vigolo and R. Piazza, *Phys. Rev. Lett.* **100**, 108303 (2008).
28. F. M. Weinert and D. Braun, *Phys. Rev. Lett.* **101**, 168301 (2008).
29. K. Clusius and G. Dickel, *Naturwissenschaften* **26**, 546 (1938).
30. A. C. Jones and E. C. Milberger, *Ind. Eng. Chem.* **45**, 2689 (1953).
31. P. Baaske *et al.*, *Proc. Natl. Acad. Sci. USA* **104**, 9346 (2009).
32. C. B. Mast and D. Braun, *Phys. Rev. Lett.* **104**, 188102 (2010).

33. I. Budin, R. J. Bruckner and J. W. Szostak, *J. Am. Chem. Soc.* **131**, 9628 (2009).
34. M. M. Hanczyc, S. M. Fujikawa and J. W. Szostak, *Science* **302**, 618 (2003
35. F. M. Weinert and D. Braun, *Nano Lett.* **9**, 4264 (2009).
36. C. B. Mast, N. Osterman and D. Braun, *J. Cosmol.* **10**, 3305 (2010).
37. J. P. Ferris and G. Ertem, *Science* **257**, 1387 (1992).
38. K. Kawamura and J. P. Ferris, *J. Am. Chem. Soc.* **116**, 7564 (1994).

PCCP

View Online
Dynamic Article Links

Cite this: DOI: 10.1039/c0cp02359k

www.rsc.org/pccp

PERSPECTIVE

Optical fluid and biomolecule transport with thermal fields

Franz M. Weinert, Christof B. Mast and Dieter Braun*

Received 2nd November 2010, Accepted 8th December 2010
DOI: 10.1039/c0cp02359k

A long standing goal is the direct optical control of biomolecules and water for applications ranging from microfluidics over biomolecule detection to non-equilibrium biophysics. Thermal forces originating from optically applied, dynamic microscale temperature gradients have shown to possess great potential to reach this goal. It was demonstrated that laser heating by a few Kelvin can generate and guide water flow on the micrometre scale in bulk fluid, gel matrices or ice without requiring any lithographic structuring. Biomolecules on the other hand can be transported by thermal gradients, a mechanism termed thermophoresis, thermal diffusion or Soret effect. This molecule transport is the subject of current research, however it can be used to both characterize biomolecules and to record binding curves of important biological binding reactions, even in their native matrix of blood serum. Interestingly, thermophoresis can be easily combined with the optothermal fluid control. As a result, molecule traps can be created in a variety of geometries, enabling the trapping of small biomolecules, like for example very short DNA molecules. The combination with DNA replication from thermal convection allows us to approach molecular evolution with concurrent replication and selection processes inside a single chamber: replication is driven by thermal convection and selection by the concurrent accumulation of the DNA molecules. From the short but intense history of applying thermal fields to control fluid flow and biological molecules, we infer that many unexpected and highly synergistic effects and applications are likely to be explored in the future.

I. Introduction

Optical methods of manipulating and investigating matter have unique advantages[1] and are present all over the life sciences.[2] While high confinement of optical resolution can be used for photolithography to pattern materials without physical contact at an ever increasing level of miniaturization,[3] optical tweezers use the momentum transfer of light to remotely move microscale objects. Although the whole range of its applicability was not obvious in the beginning,[4] this technique was developed to a sensitive force sensor for single molecules, which had an enormous impact in molecular biology.[2,5]

Furthermore, handling of liquids on the microscale became an important topic in the past, especially in the life sciences, since it shortens the time of the experiment, enhances the signal to noise ratio of detection and reduces the overall consumption of chemicals and labor. Several ways to remotely switch valves in micromanufactured channels for the control of fluid flow in channels have been explored.[6–10] Optical methods have been investigated to move covered liquid droplets[11,12] or to drive liquid flow by holographically induced vortex flows near trapped particles.[13] Lithographic surface patterning is used to induce droplet movement by thermo-capillary actuation[14] or surface acoustic waves.[15] Here we review a set of recently developed methods which uses optically created temperature fields to generate arbitrary flow patterns of liquids, to move and trap solved biomolecules down to the size of a few nanometres and to manipulate and analyze biomolecules in free solution or in their natural environment, the living cell. The optical control of temperature enables arbitrary temperature jumps within hundreds of microseconds and spatial resolution in the micrometre range. The amplitude of the temperature jump depends on the laser power and the absorption coefficient of the used wavelength. It is not coupled to the raise time. In general it can be arbitrary, *i.e.* from the ambient temperature up to the boiling temperature of the used liquid. This allows for measuring DNA melting curves in milliseconds, setting up ideal conditions for enzymes or performing thermal cycling for PCR reactions. Since all techniques are driven by the same optical setup, they can be combined arbitrarily.

The thermal movement of molecules is an unexpected effect. We only slowly learn more about why molecules exactly move in a thermal gradient. While it can be argued that the magnitude of the effect is small, recent advances showed that it is especially useful in the characterization of biomolecular

Systems Biophysics, Center for Nanoscience, Physics Department, Ludwig Maximilians Universität München, Amalienstr. 54, 80799 München, Germany. E-mail: dieter.braun@lmu.de

binding in its native environment. To understand this, we have to compare the thermal movement—named thermophoresis, thermal diffusion or Soret effect—with the well known method of electrophoresis.

Electrophoresis is extensively used in biology, however it has significant and important drawbacks. Generally, electrophoresis gels have to be used to gain a size selective electrophoretic movement. Without them, typical biological molecules move in an electrical field with equal velocity. Thus, electrophoresis has to use a special matrix and special buffers, making it impossible to analyze biomolecules in their native environment.

Although the speed of thermophoresis is typically well below 1 μm s^{-1}, its unique surface sensitivity under complex buffer conditions and the possibility to miniaturize the approach using an all-optical fluorescence detection and infrared heating technique made thermophoresis a very useful technique in the detection of biomolecular binding.

II. Light driven microfluidics in water

In this section we describe a technique to generate and control an arbitrary flow pattern in any thin liquid layer by the repetitive movement of a focused infrared laser. The laser is used to generate temperature changes in micrometre thin water layers (Fig. 1a). Due to fast thermal coupling to the near glass windows, temperature spots can be generated with diameters of only a few micrometres and changed with rates faster than 10 kHz. As a result, the water in the wake of the spot cools down very fast when the heating laser spot is moved through the liquid layer. The result is a spatially symmetric moving warm spot. If the spot speed does not allow for full equilibration of the temperature, *i.e.* for velocity larger than the spot diameter divided by the thermal equilibration time, the temperature spot becomes elongated and is followed by an exponentially decaying temperature tail. Consider the spot is moving towards the left (Fig. 1b). The water in front of the spot heats up while the water in the wake of the spot cools down to ambient temperature again. The resulting density changes of the water lead to divergent flows due to mass conservation.[16] In front of the spot the water expands, while in the wake it contracts again. At constant viscosity the system is symmetric and the contraction exactly cancels out the previous expansion. However, the temperature dependence of the viscosity breaks the symmetry. A lower viscosity at higher temperatures for example increases the velocities in the warm spot between the expansion and contraction (see bottom of Fig 1b). The result is a net flow against the spot direction. When the spot passes over once, the net shift of the water after expansion and successive contraction is in the tens of nanometre scale. However, the laser movement can be repeated in the kHz regime due to the fast thermal coupling to the nearby glass windows. Therefore reasonable fast pumping velocities in the order of 100 μm s^{-1} can be achieved, generated and defined by the movement of the laser.

Using the nonlinear effect described here, we can, for example, move water along the letters "LASER PUMP" without lateral walls to guide the flow (Fig. 2). In the experiment, we sandwich a 10 μm thin sheet of water between glass slides and move a focused infrared laser along the letters. The water is locally heated by direct absorption of the laser irradiation. The spot movement along the letters is repeated in the kilohertz regime. As a result, the fluid flows in the reverse path of the warm spot movement.

To test the model of thermally induced asymmetric expansion, a finite element simulation of the three dimensional Navier–Stokes equation was performed (Fig. 3a). The system of interest allows to do a set of approximations. We can for example assume the flow to be laminar and therefore neglect the inertia terms. Furthermore dimensions parallel to the surface are much greater than the width of the water layer, which allows us to do a thin film approximation and describe the system as a two-dimensional flow (Fig. 3b). By further approximation, which can be tested by the finite element simulations (for details see ref. 16–18), it is possible to obtain

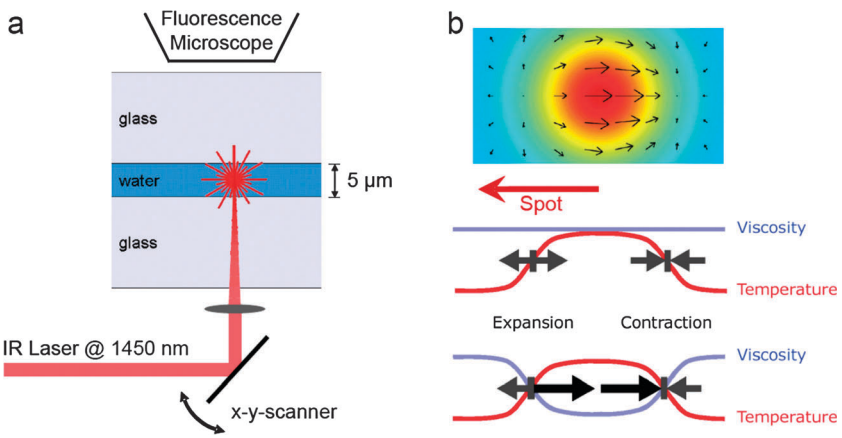

Fig. 1 (a) Schematic view of the experimental setup. An infrared laser is deflected by an Acousto-Optical Deflector and focused into a thin water layer between two glass windows. The water absorbs a part of the light. The result is a spot of raised temperature localized at the optical focus of the laser. (b) Moving the warm spot generates local fluid flows due to density changes of the water. The water expands in the front of the spot and contracts again in the wake. At constant viscosity both movements cancel out one another. However, the lower viscosity of the liquid at higher temperatures leads to increased velocities inside the warm spot. The result is a net flow against the spot direction. [Copyright *Journal of Applied Physics*].

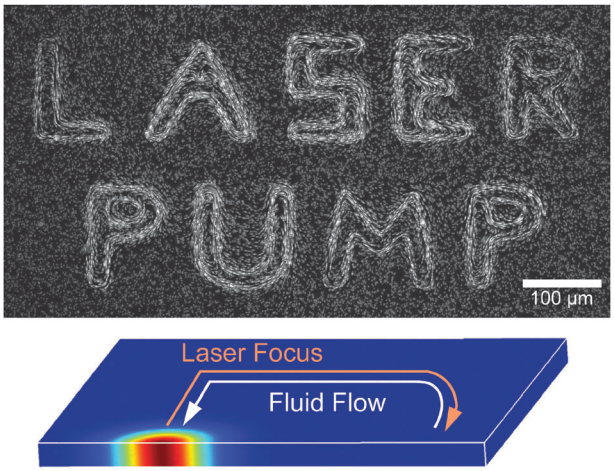

Fig. 2 Pumping water optically along arbitrary patterns. Fluid flow along the letters "LASER PUMP" is driven by dynamically heating a thin fluid film with a laser scanning microscope. As seen, complex flow patterns are easily accomplished. No channels restrict the fluid flow. Local pumping of the fluid film is the result of thermoviscous fluid movements for each passage of the laser focus. We visualize the water flow by fluorescent tracer particles. [Copyright *Journal of Applied Physics*].

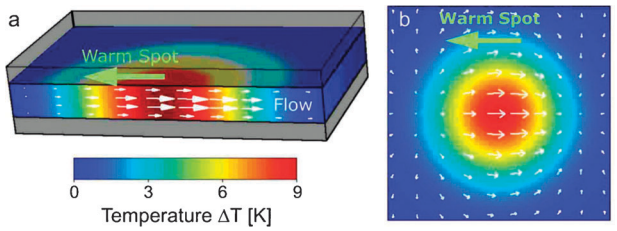

Fig. 3 Finite element simulation of the Navier–Stokes equation in the frame of reference of the moving spot. (a) Three dimensional calculation. (b) The model can be reduced to 2 dimensions by making a thin film approximation. [Copyright *Journal of Applied Physics*].

an analytical formula, which describes the pump velocity under a set of parameters:

$$v_{\mathrm{pump}} = -\frac{3\sqrt{\pi}}{4} f \alpha \beta b \Delta T^2, \qquad (1)$$

where f is the repetition frequency of the laser, α is the expansion coefficient, β is the temperature dependence of the viscosity, b is the spot width and ΔT is the amplitude of the temperature in the spot. The temperature can be obtained by imaging a temperature sensitive fluorescent dye added to the water. The shape of the moving warm spot is measured by stroboscopic illumination with a LED using a 10 µs long rectangular light pulse each time the laser spot passes by.

Since all parameters used in eqn (1) can be measured, the theoretical formula can be tested without fitting parameters. Every passage of the warm spot results in a liquid step Δx opposite to the spot movement direction. The pump speed is therefore expected to increase in a linear fashion with repetition frequency of the laser spot as given by eqn (1). This predicted behavior can be verified by measurements in the low frequency regime $f \ll 1$ kHz as shown in the inset of Fig. 4a. The repetition rate f in this experiment was adjusted by moving the laser spot with increased velocity along a fixed circular pump geometry. For slow frequencies, the spot temperature distribution remains in its Gaussian shape. However, a further increase in the spot velocity results in a considerable elongated temperature spot geometry which enhanced the pump speed beyond the linear estimate for constant spot width b (Fig. 4a). Examples of spot geometries as measured with stroboscopic temperature imaging are given as color coded insets. Interestingly, the enhanced pump velocity at high laser spot velocities could still be described when the elongated temperature spot geometry was taken into account with a spatial integral of eqn (1) for each repetition rate (Fig. 4a, solid line).

The analytical theory predicts a linear response of the pump velocity to both the thermal expansion $\alpha \Delta T_0$ and the change in

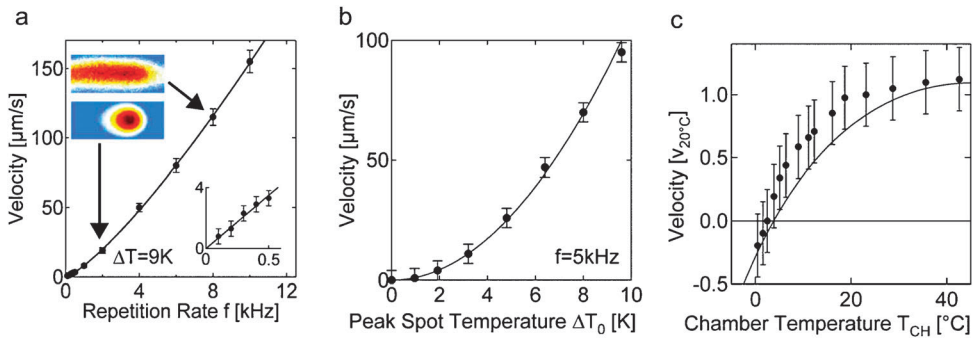

Fig. 4 Testing and comparing the analytical formula with measured pump velocities. (a) The pump velocity is a linear function of the repetition rate for $f = 1$ kHz when the spot geometry remains Gaussian. (inset: temperature image). At faster rates, the warm spot becomes elongated due to the finite thermal equilibration time of cooling. Accordingly, the pump velocity is enhanced beyond the linear prediction as the spot width b increases from 10 to 20 µm in the 5 µm thin fluid film. The solid line predicts the pump velocities based on extrapolated temperature profiles for each repetition rate f. (b) The pump velocity rises with the square of the spot temperature, confirming the linear dependence on both the thermal expansion and the temperature dependence of the viscosity. Pump velocities are predicted by eqn (1) without fitting parameters at a spot width $b = 25$ µm. (c) By changing the overall chamber temperature, we can probe the dependence on thermal expansion and temperature dependent viscosity. At 4 °C, the water contracts upon heating. As expected from eqn (1), pump velocity reverses its direction (solid line). In all plots, error bars show standard errors from particle tracking. [Copyright *Journal of Applied Physics*].

the temperature dependent viscosity $\beta\Delta T_0$ for a similar shape of the temperature spot. If the spot temperature is enhanced by higher laser power, the pump velocity increases proportionally to ΔT_0^2 as shown in Fig. 4b. The solid line results from eqn (1) without additional fitting parameters. The proportionality to the parameters α and β is tested by changing the ambient temperature T_{ch} of the chamber. In Fig. 4c we changed T_{ch} by cooling the microscope stage with an external heat bath. The experiments reveal a reversal of the pump direction at fluid temperatures below 4 °C. We attribute this reversal to the sign change of the volume expansion coefficient α. Again the theoretical expectation of eqn (1) fits the experimental pump velocities.

While the dynamic control of fluid flow on the micrometre scale is an interesting subject by itself, the capability to transport dissolved molecules is crucial for microfluidic applications. Traditional microfluidics use micromachined channels to hinder diffusion of molecules perpendicular to the pump direction. While our technique can also pump along such optically transparent channels, we aim at more flexible and previously impossible settings. For example, the method allows the usage of unstructured and disposable chambers.

To show that light driven pumping can be used in microfluidic applications, we demonstrate a purely light driven fluid mixer for small biomolecules. The initial condition is prepared by sandwiching two droplets containing initially warm low melting temperature agarose gel between glass slides. One droplet additionally contains a fluorescent labeled biomolecule. After covering the droplets by the glass slide, the droplets spread out and form an interface between one another (Fig. 5). The laser pump can be used to transport the fluorescent molecules into three pockets of different areas and mixed with the surrounding dark liquid with volume ratios of 4 : 1, 1 : 1 and 1 : 4.

III. Light driven microfluidics in ice

While the above approach works well for particles or long bio-molecules, small molecules can still diffuse through the gel and cannot be confined by the channels. In the following we will show that ice sheets can be used instead of gels to hinder diffusion. The infrared laser could be used to melt channels filled with liquid water into the ice. This system becomes even more interesting, when the channel freezes again behind the

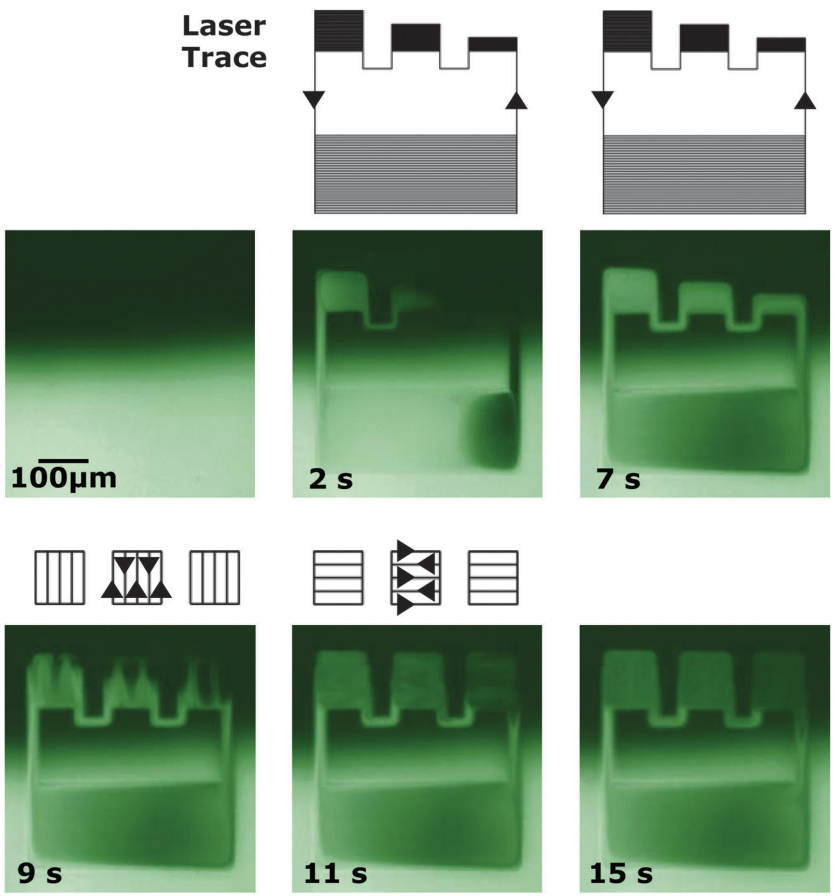

Fig. 5 Fast light driven creation of a dilution series. We have created an interface between two neighboring gels with no biomolecules on top and with biomolecules at the bottom. The stained biomolecules are first driven optically to three chambers to the top and mixed with different volumes of buffer. The result is a dilution series only created by optical fields. First, three volumes of 65, 40, and 20 pl are created with the laser pattern shown above the fluorescence images. Note that the laser direction is opposite to the pump direction. In a second step the fluid is mixed by repeatedly pumping rectangular ring flows with perpendicular orientation. The result is a dilution series with volume ratios of 4 : 1, 1 : 1, and 1 : 4 in equal volumes. [Copyright *Journal of Applied Physics*].

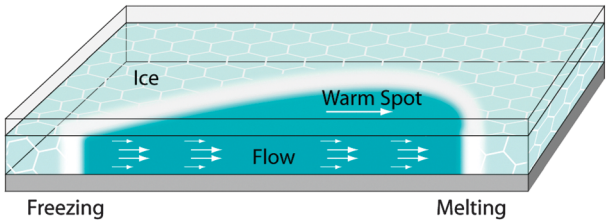

Fig. 6 An optically created temperature spot is moved to the right in a sheet of ice. The ice melts in front of the spot (right) and freezes behind it (left) and moves the fluid due to the difference in specific volume. [Copyright *Applied Physics Letters*].

heating laser spot, rather than remaining permanently thawed. By repeating the laser spot movement, the water undergoes a series of melting and freezing circles. At high repetition frequencies, considerably faster pump velocities can be achieved.[18]

The principle works as follows. Consider a spot of enhanced temperature, induced by the focused infrared laser, moving through a thin ice sheet (Fig. 6). The ice thaws at the front of the spot and freezes in its wake. The density change during the phase transition induces divergent flows due to mass conservation, with a sink (div $v > 0$) at the front and a source (div $v < 0$) at the back. The solid ice boundaries force the direction of the liquid movement towards the front of the molten compartment. We assume a parabolic flow profile perpendicular to the glass/silicon boundaries with $v_{avg} = 2/3 v_{water}$, where v_{water} is the peak velocity in the center of the fluid sheet. With the continuity equation ρ at the water–ice boundary, d_{spot} denoting the end to end distance of the molten area and if the spot movement is repeated with frequency f, we expect a pump velocity

$$v_{pump} = \Delta x f = \frac{3}{2}\frac{\rho_{water} - \rho_{ice}}{\rho_{water}} d_{spot} f. \qquad (2)$$

The length of the moving spot d_{spot} can be measured by stroboscopic white light imaging. A typical image of the drop-shaped molten area with $d_{spot} = 120$ μm is shown in Fig. 7c. For example for a repetition rate of $f = 650$ Hz with densities $\rho_{water} = 1000$ kg m^{-3} and $\rho_{ice} = 917$ kg m^{-3} we expect $v_{pump} = 9.5$ mm s^{-1}. Experimentally, we find 11 mm s^{-1} which is in agreement with the theoretical expectations.

The length of the molten spot depends on the temperature of the ice sheet (Fig. 7b). At low ice temperatures, only a short spot is molten. At higher ice temperatures, the molten spot can reach lengths beyond 500 μm with the pump velocity exceeding 50 mm s^{-1} (Fig. 7a). With this dependence, theory and experiment match quantitatively. For further increased chamber temperatures, the front of the thawed spot catches up with the back of the previous heating cycle which results in thermoviscous pumping in the reverse direction as described above. To conclude, we expect that the repetitive melting–freezing cycles are not very stressful to biomolecules since ice, if cooled as in our case on the millisecond time scale, remains amorphous and without grain boundaries.

IV. Thermophoresis: from fundamentals to binding assays

Thermophoresis is the movement of molecules in a static thermal gradient. So far, we have seen, how a dynamic thermal warming allows the fluid to move. In the following section, we will discuss how a static thermal gradient moves molecules. Already from this onset, it should be clear that we will be able to combine thermophoretic movement with fluid movement in an almost arbitrary manner as the dynamic and static thermal fields can be superposed with great flexibility.

The optical detection and induction of molecule movement in a thermal gradient is interesting from a fundamental point of view. Many more experiments have to be performed to completely understand the microscopic effects which drive the molecules in a thermal gradient. Equally interesting is the application of thermophoresis in biology, which was first demonstrated only a year ago by measuring binding curves between biologically relevant binding partners.[19,20]

We can only give a short and very rough overview over the fast growing field here. In the past many researchers have used optical density as detection for thermophoresis.[21–26] Since the signal is weak, rather high concentrations have to be employed and rather complex detection methods established to obtain enough signal. Examples are methods of beam deflection,[21,24] thermal lensing,[25] electrical heating[26] and holographic gratings with heterodyne detection approaches.[22,23]

In contrast, we have argued that the addition of a fluorescent marker to the molecule under consideration is a big advantage. Typically, the size of the marker does not change the thermophoretic properties significantly and moreover, for the study of fundamental aspects, the staining can be tuned to not affect the desired question at hand. For example, DNA can be end

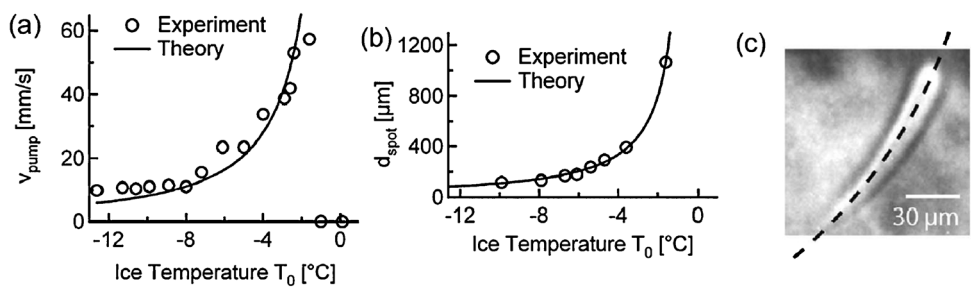

Fig. 7 (a) Pump velocities depend on the ice temperature T_0 (open circles). Eqn (2) predicts the pump velocity. (b) The length of the thawed spot becomes more elongated for higher T_0. (c) Stroboscopic image of the molten spot along a circular path, shown by the broken line. [Copyright *Applied Physics Letters*].

labeled, changing the overall charge and size of the molecule by less than 5%.

On the other side we gain two very important aspects. First, specificity: the marker enables us to measure the molecule in very complex mixtures and thus allows testing the fundamental aspects under a wide variety of buffer conditions. This becomes fundamental for the detection of molecule binding in for example blood serum.[19,20] Second, sensitivity: fluorescence allows us to detect the motion of attomolar concentrations for larger particles and typically reaches low nanomolar concentrations of biomolecules such as DNA or proteins with a single marker. Methods using refractive index as proxy do not reach such sensitivities. Fluorescence, one should mention, even allows tracking of individual particles in a thermal gradient.[27,29]

As fluorescence is an imaging technique with high sensitivity, we have direct control over fluid dynamics artifacts such as convection and can easily monitor binding of the molecules to surfaces or the formation of molecule clusters.

As it can be combined easily with optical temperature control, fluorescence imaging gives even more freedom in designing the experiments. For example, the DNA concentration can be imaged by fluorescence, while it is structured by optical temperature patterning along letters in a thin fluid film[27] (Fig. 8a) or imaged after the DNA has accumulated in microfluidic channels as thermophoresis and flow compete[28] (Fig. 8b). Thermophoretic flow around large particles[29] or the combined accumulation of DNA by convection and thermophoresis can be easily shown.[30,31] One nice case of how fluorescence allows the recording of complex phenomena is measurements where the competing depletion of a high concentration molecular crowding agent reverses the thermophoretic direction and inverts a depletion to an attraction.[32]

Due to space limitations we can't go into the details of possible explanations of thermophoresis. Basically, the experiments are tried to be described with two competing approaches. One argues that thermophoresis is a movement with low Peclet number and is more a biased diffusion motion than a directed motion. As a result, it is argued, the effect is dominated by a local thermodynamic equilibrium. Experiments support this view and demonstrate a description of thermophoresis in its size and salt dependence without fit parameters for both polystyrene beads and DNA.[27,33] Conversely competing size dependencies have been measured with different geometries, particles and methods,[27,34] without however recording the salt dependence. Whether the difference is an effect of electrical fields built up by the thermophoresis of ions,[35,36] or of the differing heating from surfaces or free fluid has to be investigated in the future. What appears clear is that when the thermal gradient grows to the extent that the Peclet number is larger than one and the movement is ballistic, Maragoni-like fluid patterns emerge and particles show hydrodynamic attraction.[29]

The speed of thermophoretic movement in typical temperature gradients of less than 0.1 K μm^{-1} is typically well below 1 $\mu m\ s^{-1}$, many order of magnitudes slower than electrophoresis. Nevertheless, the inherent size selectivity of the effect and its unique sensitivity to interfacial properties of the molecule–water interface makes it a very sensitive tool to detect changes of molecules where the diffusion coefficient or an electrophoretic movement does not record a change of the molecule. This means that thermophoresis will not be able to be used for the separation of a molecule mixture into bands of different size. However the most important biological questions do not require such separation capability. The binding of molecules, *i.e.* the analog of gel shift assays, can be handled with exquisite precision with the thermophoretic approach.

What came to the attention only recently is the use of thermophoresis for the analysis of biomolecule affinity and activity. The approach has been in the meanwhile commercialized by NanoTemper Technologies. By using capillaries, fluorescence labeling and infrared heating, a robust platform is obtained which is very flexible in a wide variety of biological settings. Here we only want to give one example which is particularly promising for the evaluation of pharmaceutical compounds (Fig. 9).[20]

Kinases are an important target for pharmaceuticals as they are the backbone of cellular signaling and play an important role in many diseases. The search of inhibitors is thus very important for the pharmaceutical industry. However the size difference between the protein (typically 40 kDa) and the inhibitor (typically 0.5 kDA) is big and makes the detection of binding with diffusion-based techniques such as FCS impossible. Also the dual labeling of the small compounds is in most cases prohibitive. However, although it was initially unexpected, thermophoresis can detect the binding by the thermophoretic depletion of the protein. It is only required to finetune the measurement conditions to allow a highly reproductive and precise measurement of thermophoresis.[20]

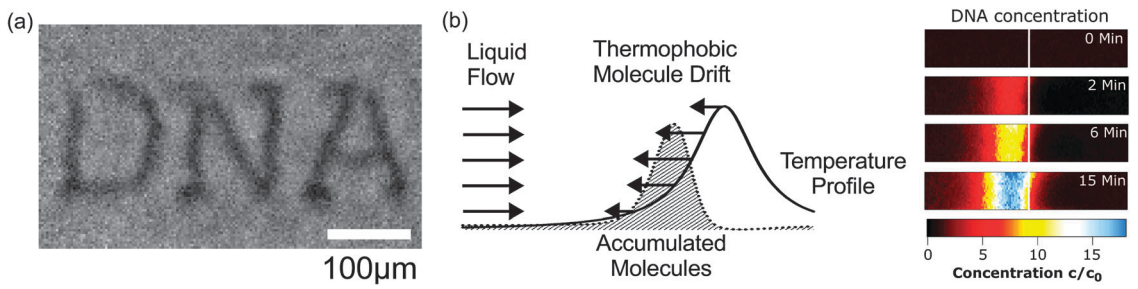

Fig. 8 (a) Thermophoresis. DNA moves form the warm to the cold region, visualized by the optical heating of the letters "DNA" and fluorescence imaging of the DNA concentration. [Copyright Proceedings of the National Academical Society, USA]. (b) Combination of thermophoresis with a flow in a microchannel leads to the accumulation of DNA at the upflow position of the heating spot. [Copyright *Physical Review Letters*].

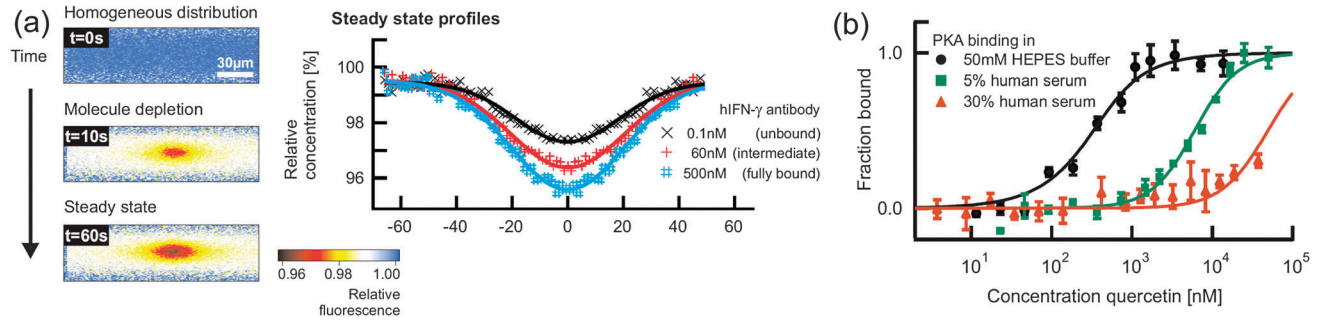

Fig. 9 (a) Microscale thermophoresis for quantification of binding. The thermophoretic depletion depends on the molecule size and linearly reports the binding probability in a binding titration series. The analysis of a concentration series quantifies the dissociation constant K_D. (b) The analysis is specially useful for detecting small molecules in complex biological liquids. An example is the kinase inhibitor quercetin binding to the kinase PKA. We find that the inhibitor significantly binds to the blood protein BSA in serum. [Copyright *Nature Communications*].

The binding shows a clear signal in the Soret coefficient as seen in Fig. 9a. The cAMP dependent kinase PKA was analyzed against the inhibitor quercetin. The kinase was fluorescently labeled and kept at a concentration of 300 nM. The inhibitor quercetin was titrated up to 50 μM in 50 mM HEPES buffer and 5% DMSO (dimethyl sulfoxide). We found an affinity of 130 ± 35 nM, in agreement with literature expectations. The thermophoretic concentration signal changed from 3.8% for the unbound state to 4.53% for the bound state, showing a 19% relative change upon binding of quercetin despite the fact that the bound complex differs by only 1%. We attribute the large signal to changes in the hydration shell originating from water molecules that are either displaced from the binding pocket or reorganized when the protein undergoes conformational changes.

Interestingly, when measured in diluted 5% and 30% blood serum, we found apparent dissociation constants K_D = 6 ± 0.4 μM and 50 ± 7 μM, respectively (Fig. 9b). Subsequent experiments showed that the drop in affinity was due to binding to human serum albumin. This shows that competing interactions, a typical but hard to assess problem in pharmaceutical development, are easily measured with fluorescence-based thermophoresis. In the short time since the development of the technique, a wide range of biological problems have been successfully tackled with the thermophoretic approach.[19,20]

V. An optical conveyor for molecules

The combination of thermophoresis with convection has a long history. Known as thermogravitational column, Clusius and Dickel developed an approach to accumulate molecules in gases in 1938.[37] With the above control of optical fluid flow and optical gradients, we can miniaturize this approach and thus significantly speed it up from several hours down to a mere second. The result is a very flexible optical conveyor for molecules. Its first application showed the concurrent accumulation and replication of DNA molecules in a replication trap. It approaches the replication and selection of genetic molecules in a single chamber, demonstrating two core processes of life in a simple and hydrothermally realistic boundary condition.

The first convection trap for DNA was demonstrated in 2002 using a combination of optically triggered convection and axial thermal gradients.[38] However, it required very low salt conditions and could only significantly trap relatively large DNA molecules with a length of 4000 base pairs. Common to all trap designs is that the thermophoretic depletion is amplified by combining the thermal field with a laser induced perpendicular liquid flow. This method allows us to trap even small DNA molecules in solution.[30,31]

The basic principle is based on a bidirectional flow of the fluid perpendicular to a thermal gradient.[30,31,37,39] As a result, the molecules are pushed by thermophoresis into one side of the flow and are transported preferentially in one direction. Applied to an axially symmetric geometry, freely diffusing molecules in a fluid film are expected to accumulate to a single spot (Fig. 10a). In effect, thermophoresis pushes the molecules to the top, where the water flow shuttles them to the center.

Interestingly, this intricate situation of counterflow and thermal gradient can be created solely by optical means. The thermal gradient is applied by focused infrared absorption in a Chromium-film below the water (Fig. 10b). The bidirectional flow is generated by the movement of the laser spot, based on the thermo-viscous fluid pump which uses thermal expansion in thermally created viscosity gradients, as shown above. We impose an outward flow near the bottom warm side by a radial laser pattern. The counterflow at the top is ensured by mass conservation.

This configuration allows the generation of a bidirectional flow in very thin fluid layers of only 2 μm. With a mean temperature difference of 15 K and a diameter of 200 μm such conveyor belt becomes very efficient even for small polymers with lengths down to 1.5 nm. Fig. 10c shows single stranded oligonucleotides with lengths of 5, 10 and 50 bases, trapped within 3 seconds. The longer DNA molecules are accumulated to higher concentrations and are more tightly confined in the center, with an $1/e$ decay at a radius of 14 μm. By inverting the flow, the conveyor transports the molecules equally efficiently in outward direction as shown for the 1000 base pair DNA in Fig. 10c, 4th image.

The physics of the conveyor belt can be simulated using finite elements. In an axial symmetric geometry we model a bidirectional flow with a maximal speed v_{max} = 200 μm s^{-1}

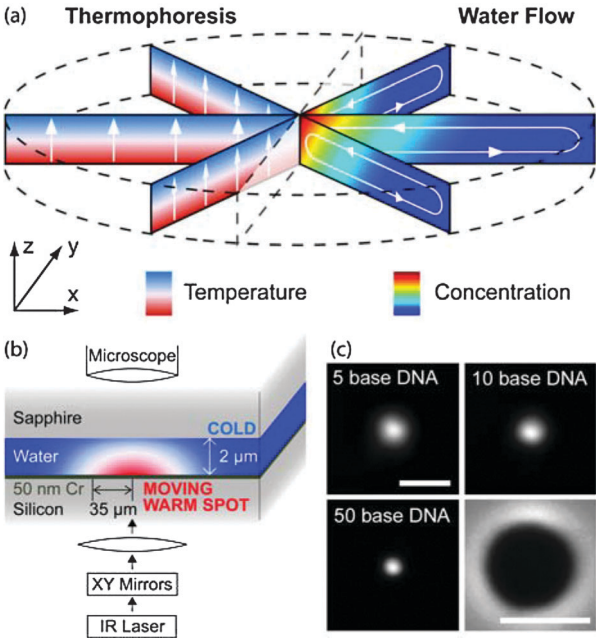

Fig. 10 Conveyor trap. (a) Bio-molecules are efficiently accumulated by a combination of a temperature gradient and perpendicular bidirectional flow. Since thermophoresis predominantly locates the molecules at the colder top, the conveyor-like water flow transports the molecules to the center. (b) Both the temperature gradient and the water flow are generated by a spot of enhanced temperature at the bottom, induced by the laser absorption in a thin metal layer. The water flow is the result of the co-axial thermo-viscous pumping in radial direction. (c) Short DNA is trapped from a diameter of 200 µm within 3 seconds. Longer DNA shows a stronger confinement. The single stranded DNA oligos with lengths of 5, 10 and 50 bases are labeled with the fluorescent dye 6-carboxy-2′,4,4′,5′,7,7′-hexachloro-fluorescein, succinimidyl ester (HEX) to visualize the concentration. By reversing the fluid flow, the molecules are transported off the conveyor, as shown by the 1000 base pair DNA stained with the intercalating dye TOTO-1. Scale bars are 100 µm. [Copyright *Nano Letters*].

within the trapping region $r < 100$ µm. We add the thermophoretic drift $v = S_T D \nabla T$ into the diffusion equation with a temperature gradient ∇T matching temperature imaging measurements using the temperature sensitive dye Cy5. The optical conveyor is simulated for various DNA lengths. Values for the diffusion coefficient D and the Soret coefficient S_T are phenomenologically interpolated. Fig. 11a shows the simulated concentration for the 50 base DNA (color scale). The simulation predicts a two million fold increase of the center concentration in the steady state.

The trapping mechanism transports the particles into the center within 3 seconds. After that period the relative concentration profile inside the trap is equilibrated. To further increase the absolute value of the center concentration, molecules have to diffuse into the region of the trap. To fill the trap up to its steady state concentration, all molecules within a radius of 10 mm would be needed to enter the trap. Fig. 11b shows the measured time trace of the center concentration, compared to the simulation prediction. The two different regimes can be clearly distinguished.

The effective potential depth of the trap can be calculated by assuming a Boltzmann distribution of the DNA molecules in steady state: $U(r) = -kT \ln(c/c_0)$. Fig. 11c shows the simulated shapes of the potentials for 50, 22, 10 and 5 base DNA. The 5 base DNA is expected to be trapped with a potential of 5 kT referring to a 200-fold accumulation. The linear shaped potential results in an exponential distribution of the concentration over the radius of the trap.

The radial fluorescence intensity of trapped DNA molecules is shown in Fig. 11d. The intensities are normalized to the center concentration to compare the accumulation efficiency by the confinement of the distribution for different polymer lengths. The concentration profile differs only in the center of the trap from the expected exponential shape. This is explained by the size of the thermal laser spot with a diameter of $d_{1/e} = 70$ µm which is used to drive the bidirectional fluid flow. In the center the laser spot overlaps and cancels out the flow. This lowers the efficiency of the trap in the center region.

The radial distribution of the measured intensity is fitted with an exponential function in the region beyond $r = 10$ µm. The trapping potential is obtained from the intensity ratio $U_{TRAP}/kT = -\ln(c/c_0) = -\ln[I_{EXP}(0)/I_{FIT}(100\ \mu m)]$, where $I_{EXP}(0)$ is the measured fluorescence intensity in the center. We take the extrapolated intensity at the edge of the trapping region $I_{FIT}(100\ \mu m)$ where the fluorescence measurement is limited by background and the dynamic range of the camera. Fig. 11e shows the measured potential depths of the molecule conveyor for single stranded DNA molecules of different lengths (open circles). The simulated data (solid line) describe the experimental results quantitatively.

Since the conveyor belt is driven entirely optically, its position can be changed easily. Instead of waiting for the molecules to diffuse into the trap, they can be collected while passing over it. Fig. 12a shows 40 nm fluorescent polystyrene beads. Comparable to a vacuum cleaner, the radial conveyor belt collects all particles on the trace. A similar protocol traps 50 base DNA molecules (Fig. 12b).

VI. The replication trap

A biologically interesting extension of the above trap is the combination of the trapping mechanism with a replication mechanism. The ultimate aim is to show that the two central pillars of the Darwinian process, namely replication and selection, are implemented simply by a thermal gradient. On the one hand, the thermal oscillation of the convection flow in a thermal trap gives rise to melting and hybridization cycles of DNA. An already replicated DNA or RNA opens up in the warm side of the chamber and is ready for another cycle of replication. This is the basic principle of the polymerase chain (PCR) reaction. On the other hand, the replicated molecules are selected out and saved from diffusion into the surrounding by the molecular trapping mechanism of combined convection and thermophoresis.

As a first step, we could show the replication and trapping in experiment. We used the replication of DNA using a polymerase protein as the proxy reaction for a replication.[31] In doing so, we implemented the two hallmarks of living matter in a single chamber, namely the replication of genetic

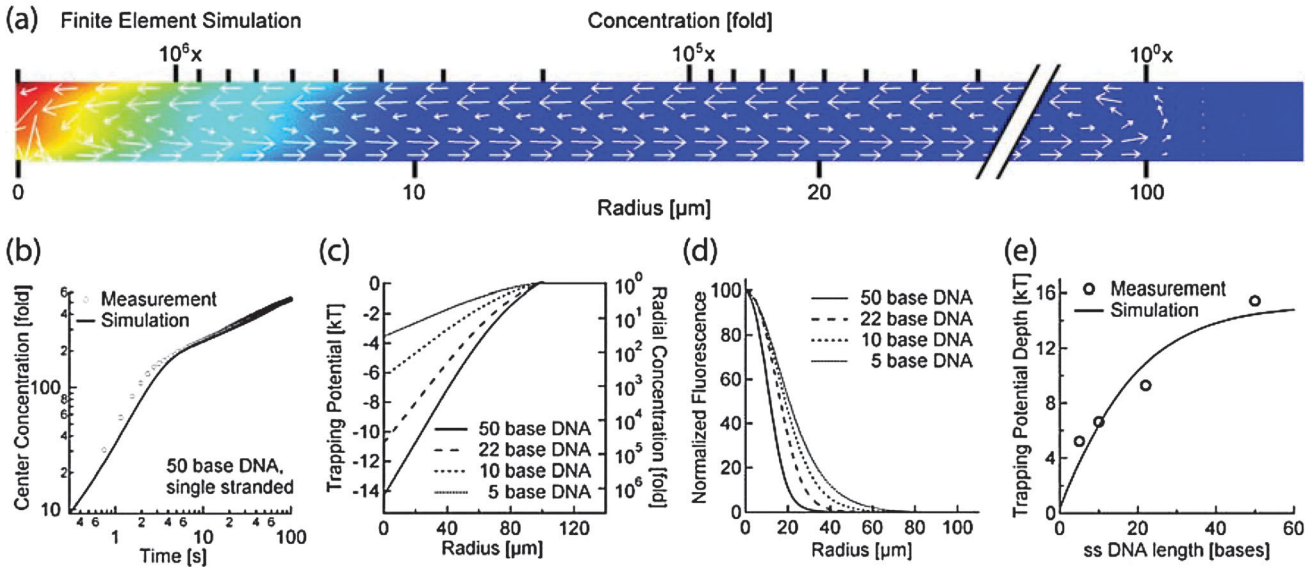

Fig. 11 Theory: (a) Finite element simulation in an axial symmetry confirms the experimental observations and predicts a steady state concentration of 2 million fold for the single stranded 50 base DNA. Arrows represent the fluid flow. (b) Molecules in the trap are shuffled to the center within 3 seconds as shown by the time trace of the center concentration. The successively slower concentration increase refers to diffusion into the region of the trap. The simulation (solid line) confirms the experimental behavior (open circles). (c) Radial distribution of the simulated trapping potential for 5, 10, 22 and 50 base DNA. (d) Measured concentration distribution of the conveyor belt. (e) Measured trapping potential depths for the DNA oligomers (open circles) match finite element simulations (solid line). [Copyright *Nano Letters*].

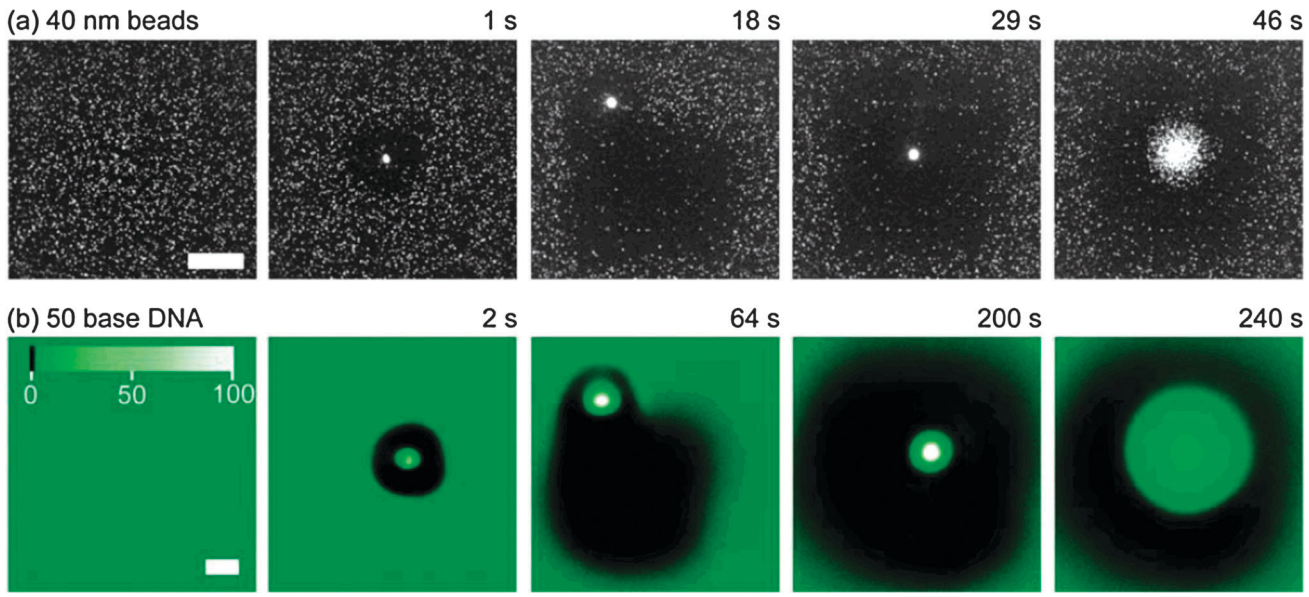

Fig. 12 Moving trap. (a) Since the conveyor belt is driven entirely optically, it can be moved arbitrarily through the solution to collect polystyrene beads with a diameter of 40 nm. After the trap has switched off, the particles diffuse freely. (b) The same processing works for the single stranded 50 base DNA. The color scale is highly nonlinear to visualize both the high concentration in the trapping center and the comparable low contrast between the outside concentration and the depleted area. The scale bars are 100 μm. [Copyright *Nano Letters*].

molecules and their active storage against diffusion. The simple nonequilibrium environment is a thermal gradient. Convective flow drives the DNA replicating polymerase chain reaction while concurrent thermophoresis accumulates the replicated 143 base pair DNA in bulk solution (Fig. 13a). The time constant for accumulation is 92 s while DNA is doubled every 50 s (Fig. 13b).

The experiments explore conditions in pores of a hydrothermal rock which can serve as a model environment for the origin of life. It is possible that such a scheme will be used in the future to select and breed useful DNA or RNA molecules. Interesting is that the setting yields 1700 DNA replications within 24 h, considerably faster than for example *E. coli* with 70 replications per day.

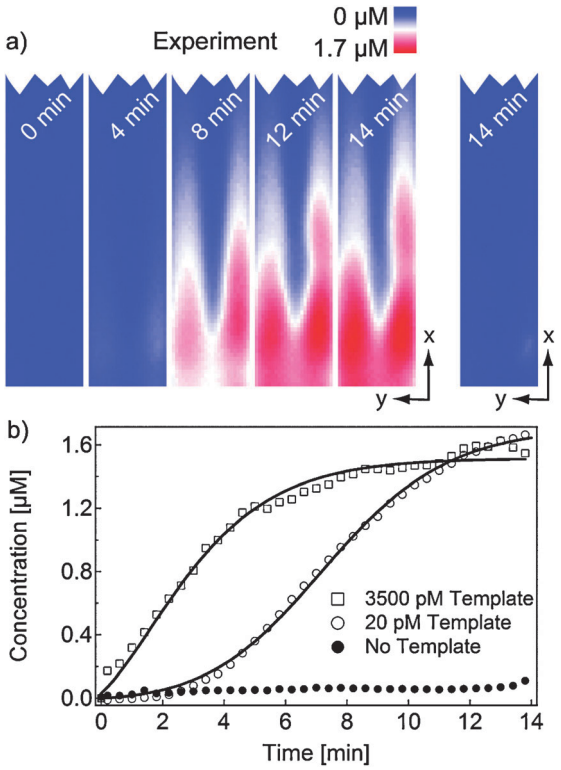

Fig. 13 Replication trap. (a) Fluorescence image of the DNA replicated and accumulated provided by the SYBR green DNA stain. A thermal gradient drives the DNA replication by the temperature oscillation in a thermal convection. The same thermal field selects the replicated DNA by accumulating it at the lower corner of the chamber. Without initial DNA, no replication result is found and fluorescence does not increase above background levels. Such a system mimics the conditions in a rock pore in the vicinity of hydrothermal vents. (b) We record the fluorescence level at the accumulation corner. The DNA replication is exponential and thus a function of its initial concentration. The results are fitted by a combination of the replication and the accumulation dynamics. [Copyright *Physical Review Letters*].

VII. Outlook

We have shown that the optical creation of thermal gradients allows us to control both molecules and water on the microscale. While the optical microflow control has applications in microfluidics, the optical thermophoresis allows the quantification of biomolecule interactions in highly sensitive assays. Both techniques can be combined to trap molecules and to reconstruct conditions for Darwinian evolution using static thermal gradients. As the developments have happened only in the last few years, we expect a number of interesting novel microscale applications using optothermal control in the near future.

Acknowledgements

We thank Natan Osterman for reading the manuscript. Financial support from the NanoSystems Initiative Munich, the International Doctorate Program NanoBioTechnology, and the LMU Initiative Functional Nanosystems is gratefully acknowledged.

References

1 A. Ashkin, Acceleration and trapping of particles by radiation pressure, *Phys. Rev. Lett.*, 1970, **24**, 156.
2 S. M. Block, L. S. B. Goldstein and B. J. Schnapp, Bead movement by single kinesin molecules studied with optical tweezers, *Nature*, 1990, **348**, 348.
3 P. S. Peercy, The drive to miniaturization, *Nature*, 2000, **406**, 1023.
4 A. Ashkin, J. M. Dziedzic, J. E. Bjorkholm and S. Chu, Observation of a single-beam gradient force optical trap for dielectric particles, *Opt. Lett.*, 1986, **11**, 288.
5 S. B. Smith, Y. J. Cui and C. Bustamante, Overstretching B-DNA: The elastic response of individual double-stranded and single-stranded DNA molecules, *Science*, 1996, **271**, 795.
6 R. B. M. Schasfoort, S. Schlautmann, J. Hendrikse and A. van den Berg, Field-effect flow control for microfabricated fluidic networks, *Science*, 1999, **286**, 942.
7 B. Zhao, J. S. Moore and D. J. Beebe, Surface-directed liquid flow inside microchannels, *Science*, 2001, **291**, 1023.
8 B. S. Gallardo, V. K. Gupta, F. D. Eagerton, L. I. Jong, V. S. Craig, R. R. Shah and N. L. Abbott, Electrochemical principles for active control of liquids on submillimeter scales, *Science*, 1999, **283**, 57.
9 M. G. Pollack, R. B. Fair and A. D. Shenderov, Electrowetting-based actuation of liquid droplets for microfluidic applications, *Appl. Phys. Lett.*, 2000, **77**, 1725.
10 D. Psaltis, S. R. Quake and C. Yang, Developing optofluidic technology through the fusion of microfluidics and optics, *Nature*, 2006, **442**, 381.
11 P. Y. Chiou, Z. H. Chang and M. C. Wu, Droplet manipulation with light on optoelectrowetting device, *J. Microelectromech. Syst.*, 2008, **17**, 133.
12 P. Y. Chiou, A. T. Ohta and M. C. Wu, Toward all optical lab-on-a-chip system: optical manipulation of both microfluid and microscopic particles, *Proc. SPIE–Int. Soc. Opt. Eng.*, 2004, **5514**, 73.
13 K. Ladavac and D. Grier, Microoptomechanical pumps assembled and driven by holographic optical vortex arrays, *Opt. Express*, 2004, **12**, 1144.
14 A. A. Darhuber, J. M. Davis, S. M. Troian and W. W. Reisner, Thermocapillary actuation of liquid flow on chemically patterned surfaces, *Phys. Fluids*, 2003, **15**, 1295.
15 A. Wixforth, C. Strobl, C. Gauer, A. Toegl, J. Scriba and Z. v. Guttenberg, Acoustic manipulation of small droplets, *Anal. Bioanal. Chem.*, 2004, **379**, 982.
16 F. M. Weinert, J. A. Kraus, T. Franosch and D. Braun, Microscale Fluid Flow Induced by Thermoviscous Expansion Along a Traveling Wave, *Phys. Rev. Lett.*, 2008, **100**, 164501.
17 F. M. Weinert and D. Braun, Optically driven fluid flow along arbitrary microscale patterns using thermoviscous expansion, *J. Appl. Phys.*, 2008, **104**, 104701.
18 F. M. Weinert, M. Wühr and D. Braun, Light driven microflow in ice, *Appl. Phys. Lett.*, 2009, **94**, 113901.
19 P. Baaske, C. J. Wienken, P. Reineck, S. Duhr and D. Braun, Optical Thermophoresis for Quantifying the Buffer Dependence of Aptamer Binding, *Angew. Chem., Int. Ed.*, 2010, **49**, 2238.
20 C. J. Wienken, P. Baaske, U. Rothbauer, D. Braun and S. Duhr, Protein Binding Assays in Biological Liquids using Microscale Thermophoresis, *Nat. Commun.*, 2010, **1**, 100.
21 M. Giglio and A. Vendramini, Soret-Type Motion of Macromolecules in Solution, *Phys. Rev. Lett.*, 1977, **38**, 26.
22 C. Debuschewitz and W. Köhler, Molecular Origin of Thermal Diffusion in Benzene + Cyclohexane Mixtures, *Phys. Rev. Lett.*, 2001, **87**, 055901.
23 J. Rauch and W. Köhler, Diffusion and Thermal Diffusion of Semidilute to Concentrated Solutions of Polystyrene in Toluene in the Vicinity of the Glass Transition, *Phys. Rev. Lett.*, 2002, **88**, 185901.
24 R. Piazza and A. Guarino, Soret Effect in Interacting Micellar Solutions, *Phys. Rev. Lett.*, 2002, **88**, 208302.
25 R. Rusconi, L. Isa and R. Piazza, Thermal-lensing measurement of particle thermophoresis in aqueous dispersions, *J. Opt. Soc. Am. B*, 2004, **21**, 605.
26 S. A. Putnam and D. G. Cahill, Transport of Nanoscale Latex Spheres in a Temperature Gradient, *Langmuir*, 2005, **21**, 5317–5323.

27 S. Duhr and D. Braun, Why molecules move along a temperature gradient, *Proc. Natl. Acad. Sci. U. S. A.*, 2006, **103**, 19678.
28 S. Duhr and D. Braun, Optothermal Molecule Trapping by Opposing Fluid Flow with Thermophoretic Drift, *Phys. Rev. Lett.*, 2006, **97**, 038103.
29 F. M. Weinert and D. Braun, Observation of Slip Flow in Thermophoresis, *Phys. Rev. Lett.*, 2008, **101**, 168301.
30 F. M. Weinert and D. Braun, An optical conveyor for molecules, *Nano Lett.*, 2009, **9**, 4264.
31 C. B. Mast and D. Braun, Thermal Trap for DNA Replication, *Phys. Rev. Lett.*, 2010, **104**, 188102.
32 H.-R. Jiang, H. Wada, N. Yoshinaga and M. Sano, Manipulation of Colloids by Nonequilibrium Depletion Force in a Temperature Gradient, *Phys. Rev. Lett.*, 2009, **102**, 208301.
33 P. Reineck, C. J. Wienken and D. Braun, Thermophoresis of single stranded DNA, *Electrophoresis*, 2010, **31**, 279–286.
34 M. Braibanti, D. Vigolo and R. Piazza, Does Thermophoretic Mobility Depend on Particle Size?, *Phys. Rev. Lett.*, 2008, **100**, 108303.
35 J. Morthomas and A. Würger, Thermoelectric effect on charged colloids in the Hückel limit, *Eur. Phys. J. E*, 2008, **27**, 425–434.
36 D. Vigolo, S. Buzzaccaro and R. Piazza, Thermophoresis and Thermoelectricity in Surfactant Solutions, *Langmuir*, 2010, **26**, 7792–7801.
37 K. Clusius and G. Dickel, Neues Verfahren zur Gasentmischung und Isotopentrennung, *Naturwissenschaften*, 1938, **26**, 546.
38 D. Braun and A. Libchaber, Trapping of DNA by thermophoretic depletion and convection, *Phys. Rev. Lett.*, 2002, **89**, 188103.
39 P. Baaske, F. M. Weinert, S. Duhr, K. H. Lemke, M. J. Russell and D. Braun, Extreme accumulation of nucleotides in simulated hydrothermal pore systems, *Proc. Natl. Acad. Sci. U. S. A.*, 2007, **104**, 9346.

Journal of Cosmology, 2010, Vol 10, 3305-3314.
JournalofCosmology.com, August, 2010

Disequilibrium First: The Origin of Life

Christof B. Mast, Natan Osterman, Ph.D., and Dieter Braun, Ph.D.,
Systems Biophysics, Center for Nanoscience, Ludwig Maximilians University Munich, Germany.

Abstract
We argue here that disequilibrium conditions are central for understanding the origin of life. Taking energetic chemicals at high concentrations to synthesize more complex molecules will not be enough to emulate and understand early pre-biotic evolution. Not the energetic, but the entropic picture is crucial. Life comes into existence only in disequilibrium situations. Experiments on studying the modes of entropy reduction in disequilibrium systems are the only way to understand the creation of complexity using biologically relevant molecules. Origin of life research will have to come out of the chemical and biochemistry labs and move onto interdisciplinary ground to make substantial progress in the future. Disequilibrium experiments will explore how those daring initial molecules had to evolve into complex information carrying biomachines. Disequilibrium experiments enable us to explore the possible routes that those daring initial molecules took to evolve into complex information carrying biomachines.

Keywords: Disequilibrium, non-equilibrium, evolution, origin of life, hydrothermal vents, primordial life,

1. Introduction

Many scholars argue that genetic replication alone will not make a realistic scenario for the first Darwinian process and the start of molecular evolution (e.g. Dyson 1986). So "genes first" should be complemented by some kind of metabolism to create the necessary living and replicating molecules; i.e. "metabolism first". But what does "metabolism first" really mean? We want to argue here that "metabolism", although generally not very well defined, is often used rather as a synonym for "good" boundary conditions to host life. However, based on an understanding of the entropic need for disequilibrium boundary conditions, we can arrive at a more precise definition of what is necessary to create information bearing molecules and to drive a Darwinian Process of replication, mutation and selection. The second law of thermodynamics requires disequilibrium settings to sustain life and this has been known for decades (Schrödinger 1946, Wicken 1978). We believe an understanding of "metabolism first"complements "genetic first" by providing the necessary boundary conditions.

Old ideas on the origin of life were dominated by the belief in 'spontaneous generation', i.e. the idea that life transforms itself all the time from non-living matter. Animals were supposed to appear out of all kinds of non-living materials and the idea that life may have arisen slowly, from an ancient earth after a long evolutionary period of development were utterly foreign. The basic idea, which has lived on into the 21st century, is that chemicals may be mixed together, and become energized thereby achieving life, and this belief has been rightly criticized as implausible (Joseph and Schild 2010). And yet, many in the scientific community are still preoccupied with a notion of mixing things together—that life can be created spontaneously if only we can divine the right recipe and discover and mix together the right concentrations of the correct and matching molecules.

These rather naive conceptions were long ago supplanted by more plausible scenarios, including the "RNA World" hypothesis which incorporates conceptions of entropy and energy. But is such a picture of life's origins accurate? Does it create enough structure to drive a process of Darwinian evolution? Our guess is: No. Loss of molecules by decay will prevent life from arising. Furthermore, simple diffusion is a very powerful driving force on the small micrometer scale. Both have to be compensated for by a disequilibrium condition to refresh the molecules. While such mechanisms and considerations are fundamental, they are rarely considered by those concerned with the origin of life.

2. Equilibrium Settings

Vesicles (Figure 1a) have been discussed at length as the be all and end all of the origin of life (Koch 1985, Szathmáry and Demeter, 1987, Szostak 2001). This idea could be called the "Vesicles First" hypothesis, i.e. that compartmentalization and encapsulation enable life to achieve life, once lipids were joined together to create membranes. Although very interesting properties of lipids have been reported (Walde et al. 1994, Oberholzer et al. 1995, Wick and Luisi 1996, Tsukahara et al. 2004), we find its initial importance doubtful. The main reason being the isolation of molecules into an equilibrium state (Figure 1a). No enhanced concentration of molecules is achieved by the presence of a membrane enclosure. If the concentration is not high at the outside it will not flow into the inside and the vesicles cannot be filled to high concentrations since a directional transport is lacking the necessary highly evolved protein machinery and the energy to fire transport. While the feeding of replication or translation from the outside has been demonstrated, these experiments first required a filling of the vesicles at high concentrations (Hanczyc et al. 2003). At these high concentrations, the experiments could have been performed without using a membrane enclosure and therefore mean nothing. With the membranes, molecular reactions are rather hindered, likewise, the replacement of degraded molecules with new ones is inhibited.

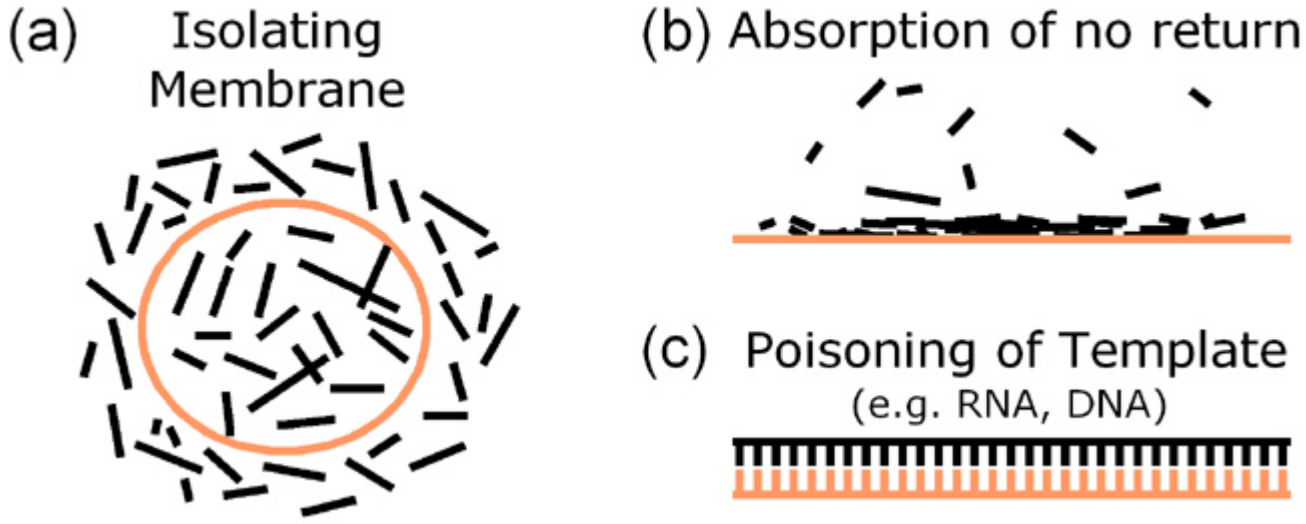

Figure 1. Disequilibrium First. Boundary conditions discussed for the origin of life often favor thermodynamic equilibrium. (a) A membrane encapsulates molecules at high concentration only if they are already concentrated on the outside. Without highly evolved directional transport from membrane proteins through pores, a membrane drives the system into equilibrium since it blocks molecular exchange. (b) Surface-induced catalysis only works for small molecules which can use thermal fluctuations for desorption. Larger molecules require desorption steps from disequilibrium settings or are fixed to the two-dimensional surface. (c) The RNA world scenario lacks a non-equilibrium setting to remove the replicated strand from the template. Template poisoning, i.e. the permanent attachment of the replicated strand - blocks the information from being replicated.

Many scientists reject the "Vesicles First" hypothesis and believe that vesicles were not necessary for the development of the first replicating molecules (e.g. Martin and Russell 2003), such that cellular

organization came later, not first. Manfred Eigen (1981) has argued that "organization into cells was surely postponed as long as possible. Anything that interposed spatial limits in a homogeneous system would have introduced difficult problems for prebiotic chemistry. Constructing boundaries, transposing things across them and modifying them when necessary are tasks accomplished today by the most refined cellular processes." Vesicles are considered too much “equilibrium” than “non-equilibrium” boundary conditions.

Similarly, the absorption on surfaces (Figure 1b) has been discussed as a mechanism to enhance the local concentration of the necessary chemicals and to trigger catalytic activity (Ferris and Ertem 1992, Kawamura and Ferris 1994). However experiments using longer, information bearing molecules typically require a washing step after surface catalysis to remove the molecules. Although a disequilibrium boundary condition which could implement such a desorption mechanism might provide the necessary impetus for life, this possibility is seldom taken into consideration. Therefore, according to the surface absorption hypothesis, the molecules have to sit on the surface until they are degraded into pieces short enough such that they can be removed by desorption using Brownian motion. However, in fact, the templated replication of longer nucleotides (Figure 1c) poisons the replicated template and they will only be removed by degradation.

The theory of spontaneous generation has never really died, although one might have expected the experiments of Louis Pasteur to have administered the coup de grâce with his work "On the organized corpuscles that exist in the atmosphere; examination of the doctrine of spontaneous generation" (Louis Pasteur 1861). Pasteur was able to show that spores and bacterial life forms exist on the microscale and induce only an apparent "spontaneous" generation of life. We see an analogy here with present day thinking. Just as people at that time took for granted that life creates itself everywhere from scratch, origin-of-life researchers tend to take it for granted that life should be able to grow from scratch, or at least from very limited food sources and in equilibrium settings. These views have been ridiculed as completely implausible (Joseph 2009; Joseph and Schild 2010).

Life can only survive when it has ways to import food into a reaction chamber against a considerable chemical potential created by high concentrations of molecules already inside the cell. This is made possible via directed membrane transport equipped with highly evolved protein machinery. How could a primitive membrane machinery create directed transport across a membrane without an ATP metabolism and in the absence of highly evolved membrane proteins? On the other hand, as we will see below, rather simple disequilibrium conditions such as a thermal gradient, can provide such a pump and import molecules into microscale pores in mineral precipitates (Baaske et al. 2007).

Table 1. Examples for disequilibrium conditions used in molecular evolution experiments.

Examples for Disequilibrium Settings	
Artificial Disequilibrium Conditions	**Persisting Geological Disequilibrium Settings**
High starting molecule concentration	Temperature oscillation by thermal microconvection
Unloaded catalytic surfaces	Nano/micro-particles moving in convection allowing catalytic adsorption and desorption
Vesicles filled with high concentrations of molecules	Accumulation by microconvection and thermophoresis (thermal diffusion)
Activated, fast decaying molecules	Size-dependent selection of molecules by thermophoretic trap.
Washing steps	Transport and accumulation by pH gradients
Purification and selection in columns for in vitro evolution	UV illumination under day-night cycles
Volume transport by pipetting	Periodic eutectic freeze out
External buffer or salt changes	Dry-wet cycles

3. Disequilibrium Settings

The examples of Table 1 illustrate the point we want to make here. Without doubt, most origin of life experiments do indeed use disequilibrium conditions in the lab. For example, they start with a high molecule concentration, fill molecules at high concentration into vesicles, put molecules on unloaded, fresh catalytic surfaces and begin after creating well prepared initial conditions. However, these conditions lack a persistent, geological disequilibrium implementation. The experiments run into thermodynamic equilibrium, or in other words, they die. They miss the opportunity to explore continuous evolution in a maintained disequilibrium steady state, and therefore, fail to create the conditions necessary for the establishment of life.

Persistent disequilibrium is for example obtained from a constant gradient of a thermodynamic property. This can be a temperature gradient (as discussed later) or the close contact of two different materials which induce salt, pH and redox potentials. The latter is discussed in the geometry of membranous boundaries of mineral precipitate enclosures are envisioned by Michael Russell (Russell and Hall, 1997, Martin and Russell 2003, Martin and Russell 2007). These chambers have built-in gradients across a semi-permeable membrane. Directed electrical transport with the possibility of catalytic synthesis along the pH gradient is the natural result of a geologically focused gradient. We envision that many other disequilibrium settings are likely to be found, discussed and explored in the future as the advantages of disequilibrium settings for the origin of life are recognized.

Another persistent disequilibrium can occur in a flow from a warm liquid to a cold one, a setting studied for example by Koichiro Matsuno, who demonstrated the polymerization of peptides in the fast cooling environment of hydrothermal outflows into the ocean (Imai et al. 1999). Other examples are dry-wet cycles or day-night cycles which induce oscillatory temperature or phase state changes on the hour time scale. We are not a particular fan of the latter setting as the volume which is used for wetting will lead to very strong dilutions that are not compensated for in the next drying cycle. As a result, the overall loss of molecules is probably too large to be compensated by the gain of concentration in the dry cycle. Also, like day and night cycles, the kinetics might be too slow to yield a fast evolving system.

Shown in Figure 2 is the example of a disequilibrium setting of a temperature gradient. It can suck a high concentration of molecules (Braun and Libchaber 2002, Baaske et al. 2007) into a millimeter-sized chamber and concurrently implement a thermal cycling in the same setting to foster DNA replication (Braun et al. 2003) (Figure 2a). As demonstrated, both can be combined (Mast and Braun, 2010) to replicate DNA by thermal cycles in an exponential manner and the accumulation of the replicates in a micrometer-sized spot (Figure 2b). As a result a simple disequilibrium setting comes close to implementing a Darwinian process with replication and selection in a simple chamber. Furthermore, the degradation of molecules does not lead to a dead end as molecules constantly re-accumulate. Interestingly, the trap implements a selective pressure to keep the longer of the replicated molecules in play.

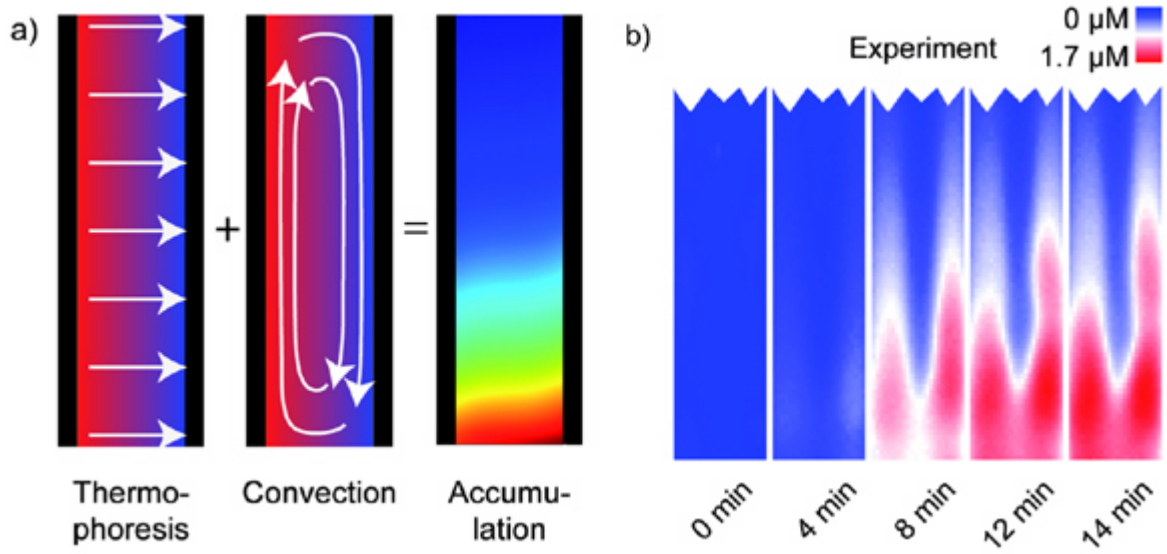

Figure 2. Replication Trap. A thermal disequilibrium combines thermal oscillation by convection and molecule accumulation by thermophoresis in a single chamber. This allows exponential replication as the nucleotides separate by temperature spikes – here implemented by a PCR replication protein due to a lack of a similar RNA world scenario. At the same time, the replicating molecules are accumulated. Such a setting comes close to host a Darwinian process of replication (by convection) and selection (by thermophoretic trapping) in a single chamber. Reprinted from (Mast and Braun 2010), Copyright by the American Physical Society.

In the experiment, the convection cycles the temperature in 60 seconds and the accumulation reaches a steady state within the chamber after 90 seconds. However, these numbers strongly depend on the geometries. Convection can for example reach 0.1s return times in smaller, circular chamber geometries. The latter might allow the fast cooling experiments run by Matsuno (Imai et al. 1999) in a single convection chamber. What the convection certainly allows is for the implementation of adsorption/ desorption cycles on clay particles which are too large to be efficiently accumulated. The particles periodically add and remove large polymers on their surfaces and allow for efficient catalytic activities, for example along the lines of James Ferris (Ferris and Ertem 1992, Kawamura and Ferris 1994).

It is interesting to note that even in one convection chamber, the laminar convection produces trajectories which are isolated from each other by the laminarity of the flow. Diffusion can bridge between them only at a much smaller time scale than the temperature oscillation of convection. A single chamber can thus host a number of thermal cycling conditions which interact at time scales slower than the convection itself. Therefore different species of molecules could replicate in parallel under different conditions and allow for coevolution and evolution of subpopulations.

The physical location for this temperature gradient and the pores that host convection follow the lines of Corliss, Russell, Hall, Cairns-Smith, Matsuno, Martin and others (Corliss et al. 1979, Russell et al.

1988, Imai et al. 1999, Russell and Hall 1997). They pinpointed hydrothermal systems on the deep-sea floor for the origin of life (Boyce et al. 1983, Holm 1992, Van Dover 2000, Kelley 2001). Hydrothermal venting systems create large flows of hot water (50°C to 370°C). This high temperature circulation is contrasted by 2°C cold ocean water on the outside. Between are porous mineral precipitates and rocks with a multitude of porous spaces allowing a complex network of convection chambers. This network of chambers can effectively dictate different tasks, one pore could accumulate shorter polymers while a neighboring pore give rise to large scale temperature oscillations and thereby longer polymers.

4. Disequilibrium First

In our view, most interesting are disequilibrium settings which keep the concentrations of molecules at a constantly high level or implement steady states of constant change. In modern time most life can create structures within the second law of thermodynamics by – directly or indirectly – converting high energy, low entropy solar radiation into low energy, high entropy waves. To study the origin of life, we have to search for a similar geological flux of entropy which allows the buildup of structure in a disequilibrium setting. From everyday observations it is clear that life which cannot keep itself in a state of disequilibrium(i.e. is without food and without gradients), cannot be sustained and dies.

We expect that a focus on disequilibrium conditions will foster more interdisciplinary research. In the past, the field was dominated by experiments where high concentrations of molecules were used as the entropic driving force to push the reaction into the desired (and preconceived) direction. It is a typical reflex for a chemist to grab the concentrated molecule and study its reactions in a mix and analyze the setting. Only slowly is the field realizing that it is missing many interesting and creative boundary conditions in such approaches.

Freeman Dyson (Dyson 1986) has stressed that metabolism and replication have to be combined to understand the origin of life. He saw a neglect of metabolism in a genetically focused origin of life research and made the distinction between the replication of genes and the reproduction of the cell. Making use of a metabolism, a “second beginning” occurred in which nucleotides were synthesized, genes entered in a way analogous to a parasitic disease, only later to develop the symbiotic advantage of replication and reproduction. Dyson argued that this active metabolism of the beginning already shaped the possibilities and constraints of genetic information.

We would like to point out that a disequilibrium setting must predate metabolism. A living metabolism can only be created by the structure, concentrations and specific molecules possible in an entropy flow. Otherwise it has to succumb to the cruelty of the second law of thermodynamics: equilibrium systems have to decay into a state of homogeneous high entropy. To build the metabolism that can host genes, we argue that the disequilibrium setting has to predate both. Not metabolism first or genes first is crucial to create life, but the disequilibrium is at least similarly important, if not the central ingredient to drive and originate life.

We see ideas on the origin of life converging, both on the experimental and theoretical level. For example, the Szostak group showed that the hydrothermal mechanism accumulate small molecules (Braun and Libchaber 2002, Baaske et al. 2007) and will form vesicles when applied to lipids (Budin et al. 2009). As a result, vesicles form and have the co-accumulated molecules already inside. This exactly counters our above criticism that vesicles have to be prepared at high content concentrations by using a disequilibrium setting. Similarly, joining Ferris' surface catalysis with desorption and adsorption by thermal convection is likely to generate more interesting and longer nucleotide strands. Moreover, those strands are not accessible to water without washing steps. Other converging moves have older roots. Already some time ago, Hans Kuhn was focusing on how to merge ideas from replication with those of translation (Kuhn and Waser 1982). The path we see before us is the path of integration of different approaches along the line of disequilibrium settings. We will see a number of disequilibrium, often microscale, experimental ideas from more disciplines. The experiments will shift

the focus from kinetic chemical equilibrium experiments (i.e. mix and analyze) towards true steady state disequilibrium conditions. We expect many new interesting results from them.

References

Baaske P, Weinert FM, Duhr S, Lemke KH, Russell MJ, and Braun D, ((2007), Extreme accumulation of nucleotides in simulated hydrothermal pore systems, Proc. Nat. Acad. Sci. 104, 9346–9351.

Bainbridge A, Crane K, van Andel TH, (1979), Submarine thermal springs on the Galapagos Rift, Science (203, 1073-1083.

Boyce EGAJ, Coleman ML and Russell MJ, (1983), Formation of fossil hydrothermal chimneys and mounds from Silvermines, Ireland, Nature 306, 545–50 Braun D and Libchaber A, (2002), Trapping of DNA by thermophoretic depletion and convection, Phys. Rev. Lett. 89, 188103.

Braun D, Goddard NL and Libchaber A, (2003), Exponential DNA replication by laminar convection, Phys. Rev. Lett. 91, 158103.

Budin I, Bruckner RJ and Szostak JW, (2009), Formation of protocell-like vesicles in a thermal diffusion column, J. Am. Chem. Soc. 131, 9628–9629.

Corliss JB, Dymond J, Gordon LI, Edmond JM, von Herzen RP, Ballard RD, Green K, Williams D, (1979), Submarine thermal springs on the Galapagos Rift, Science, (203, 1073-1083.

Dyson F., (1986), Origins of Life, Cambridge University Press.

Eigen M., Gardiner W., Schuster P. and Winkler-Oswatitsch, R., (1981), The origin of genetic information, Scientific American, 244, 88-118.

Eigen M., (1994), The origin of genetic information, Origins of Life and Evolution of Biospheres, 24, 241-262.

Ferris JP and Ertem G, (1992), Oligomerization of ribonucleotides on montmorillonite: reaction of the 5'-phosphorimidazolide of adenosine, Science, 257, 1387-1389.

Hanczyc MM, Fujikawa SM, Szostak JW, (2003), Experimental models of primitive cellular compartments: encapsulation, growth, and division, Science 302, 618 - 622.

Holm NG (ed.), (1992), Marine hydrothermal systems and the origin of life, Orig. Life Evol. Biosphere 22, 1–242.

Imai E, Honda H, Hatori K, Brack A and Matsuno K, (1999), Elongation of oligopeptides in a simulated submarine hydrothermal system, Science 283, 831–833.

Kawamura K and Ferris JP, (1994), Kinetic and mechanistic analysis of dinucleotide and oligonucleotide formation from the 5'-phosphorimidazolide of adenosine on Na+-montmorillonite, J. Am. Chem. Soc., 116, 7564–7572.

Kelley DS et al., (2001), An off-axis hydrothermal vent field near the Mid-Atlantic Ridge at 30 N, Nature 412, 145–149.

Koch A.L., (1985), Primeval cells: possible energy-generating and cell-division mechanisms, Journal of Molecular Evolution, 21, 270-277.

Kuhn H and Waser J, (1982), Evolution of early mechanisms of translation of genetic information into polypeptides, Nature 298, 585.

Martin W and Russell MJ, (2003), On the origins of cells: a hypothesis for the evolutionary transitions from abiotic geochemistry to chemoautotrophic prokaryotes, and from prokaryotes to nucleated cells, Phil. Trans. R. Soc. Lond. B, 358, 59-85.

Martin W and Russell MJ, (2007), On the origin of biochemistry at an alkaline hydrothermal vent, Phil. Trans. R. Soc. Lond. B, 362, 1887-1926.

Mast CB and Braun D, (2010), Thermal Trap for DNA Replication, Phys. Rev. Lett. 104, 188102.

Oberholzer T, Albrizio M and Luisi PL, (1995), Polymerase chain reaction in liposomes, Chemistry & Biology, 2, 677-682.

Pasteur L, (1861), Sur les corpuscules organisés qui existent dans l'atmosphere. Examen de la doctrine des generations spontanees. Ann. sci. naturelles (partie zoologique) (S6r. 4) 16, 5-98.

Russell MJ, Hall AJ, Cairns-Smith AG and Braterman PS, (1988), Submarine hot springs and the origin of life, Nature 336, 117.

Russell MJ and Hall AJ, (1997), The emergence of life from iron monosulphide bubbles at a submarine hydrothermal redox and pH front, J. Geol. Soc. London 154 377–402.

Schrödinger E., (1946), What is life? Macmillan Press.

Szathmáry E. and Demeter L., (1987), Group selection of early replicators and the origin of life, Journal of Theoretical Biology, 128, 463-486.

Szostak J., (2001), Synthesizing life, Nature 409, 387-390.

Tsukahara H, Imai E, Honda H, Hatori K and Matsuno K, (2004), Evolving lipid vesicles in prebiotic hydrothermal environments, Origins of Life and Evolution of Biospheres, 32, 13-21

Van Dover CL, (2000), The Ecology of Deep-Sea Hydrothermal Vents, Princeton University Press.

Walde P, Wick R, Fresta M, Mangone A, Luisi PL, (1994), Autopoietic self-reproduction of fatty acid vesicles, J. Am. Chem. Soc., 116, 11649–11654.

Wick R and Luisi PL, (1996), Enzyme-containing liposomes can endogenously produce membrane-constituting lipids, Chemistry & Biology, 3, 277-285.

Wicken J.S., (1978), Information transformations in molecular evolution, J. Theo. Biol. 72, 191-204.